Magnetic hysteresis up to 80 kelvin in a dysprosium metallocene single-molecule magnet

Article (Accepted Version)

Title: Magnetic hysteresis up to 80 K in a dysprosium metallocene single-molecule magnet

Authors: Fu-Sheng Guo,[1] Benjamin M. Day,[1,2] Yan-Cong Chen,[3] Ming-Liang Tong[3]*, Akseli Mansikkamäki[4]*, Richard A. Layfield[1]*.

Affiliations:

[1]Department of Chemistry, School of Life Sciences, University of Sussex, Falmer, BN1 9QJ, U.K.

[2]School of Chemistry, The University of Manchester, Oxford Road, Manchester, M13 9PL, U.K.

[3]Key Laboratory of Bioinorganic and Synthetic Chemistry of the Ministry of Education, School of Chemistry, Sun-Yat Sen University, Guangzhou 510275, P.R. China.

[4]Department of Chemistry, Nanoscience Centre, University of Jyväskylä, P. O. Box 35, FI-40014 Jyväskylä, Finland.

*Correspondence to: R.Layfield@sussex.ac.uk.

Abstract: Single-molecule magnets (SMMs) containing only one metal center may represent the lower size limit for molecule-based magnetic information storage materials. Their current drawback is that all SMMs require liquid-helium cooling to show magnetic memory effects. We now report a chemical strategy to access the dysprosium metallocene cation $[(Cp^{iPr5})Dy(Cp^*)]^+$ (Cp^{iPr5} = penta-iso-propylcyclopentadienyl, Cp* = pentamethylcyclopentadienyl), which displays magnetic hysteresis above liquid-nitrogen temperatures. An effective energy barrier to reversal of the magnetization of U_{eff} = 1,541 cm^{-1} is also measured. The magnetic blocking temperature of T_B = 80 K for this cation overcomes an essential barrier towards the development of nanomagnet devices that function at practical temperatures.

One Sentence Summary: Magnetic blocking above liquid-nitrogen temperatures is demonstrated in a dysprosium single-molecule magnet.

Main Text:

The observation of slow magnetic relaxation in coordination compounds that contain a single lanthanide ion stimulated considerable interest in monometallic single-molecule magnets (SMMs) (*1*). This family of materials shows magnetic hysteresis properties that arise from the electronic structure at the molecular level rather than interactions across comparatively large magnetic domains (*2-4*). In addition to the considerable fundamental interest in SMMs and related magnetic molecules, their magnetic memory properties have inspired proposals for applications as spin qubits (*5*) and in nanoscale spintronic devices (*6*). A key performance parameter of an SMM is the magnetic blocking temperature, T_B, one description of which refers the maximum temperature at which it is possible to observe hysteresis in the field-dependence of the magnetization, subject to the field sweep rate. The blocking temperature provides a means of comparing different SMMs and, to date, the vast majority that show any hysteresis at all require liquid-helium cooling to do so (*7,8*). A few notable examples have emerged from the extreme cold to set record blocking temperatures above the liquid-helium regime (*9-12*), including the dysprosium metallocene $[(Cp^{ttt})_2Dy][B(C_6F_5)_4]$ (Cp^{ttt} = 1,2,4-tri-*tert*-butylcyclopentadienyl), which showed magnetic hysteresis with coercivity up to 60 K (*13-15*); however, this threshold

still falls markedly short of the more practically accessible 77 K temperature at which nitrogen liquefies. We now show that by designing the ligand framework so that two key structural parameters – i.e. the Dy-Cp_{cent} distances (cent refers to the centroid of the Cp ligand) and the Cp-Dy-Cp bending angle – are rendered short and wide, respectively, we achieve an axial crystal field of sufficient strength to furnish an SMM that shows hysteresis above 77 K.

A dysprosium metallocene cation was targeted with cyclopentadienyl substituents of sufficient bulk to produce a wide Cp-Dy-Cp angle, but not too bulky to preclude close approach of the ligands. Thus, the borohydride precursor complex [(η^5- Cp^{iPr5})Dy(η^5-Cp^*)(BH_4)] (**2**) (Cp^{iPr5} = penta-iso-propylcyclopentadienyl, Cp^* = pentamethylcyclopentadienyl) was synthesized by treating [Dy(η^5-Cp^{iPr5})(BH_4)$_2$(THF)] (**1**) with KCp^* (Fig. 1). The molecular structures of **1** and **2** were determined by x-ray crystallography (tables S1-S3, figs S4, S5). The target compound [(η^5-Cp^*)Dy(η^5-Cp^{iPr5})][$B(C_6F_5)_4$] (**3**), hereafter abbreviated [Dy-5*][$B(C_6F_5)_4$], was then isolated in 60% yield by treating **2** with the super-electrophile [$(Et_3Si)_2(\mu$-H][$B(C_6F_5)_4$] (*16*). An x-ray crystallographic analysis of the molecular structure of **3** at 150 K (fig. 1, figs S6-S7, tables S1, S4) revealed that the Dy-5* cation features Dy-Cp^* and Dy-Cp^{iPr5} distances of 2.296(1) Å and 2.284(1) Å, respectively, which are, on average, 0.026 Å shorter than the analogous distances of 2.32380(8) Å and 2.30923(8) Å determined for [$(Cp^{ttt})_2$Dy]$^+$ (*13*). Furthermore, the Cp-Dy-Cp angle in Dy-5* is 162.507(1)°, and hence almost 9.7° wider than the angle of 152.845(2)° found in [$(Cp^{ttt})_2$Dy]$^+$. Based on these structural parameters, the crystal field in Dy-5* should be stronger and more axial than in [$(Cp^{ttt})_2$Dy]$^+$, and hence an improvement in the SMM properties can be expected.

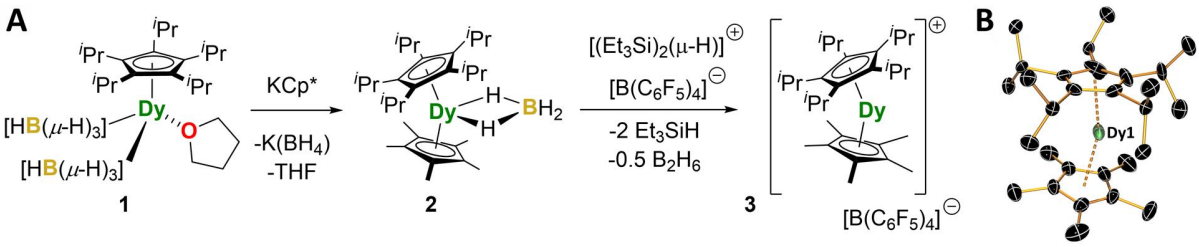

Fig. 1. Synthesis and molecular structures. (**A**) Reaction scheme for the synthesis of **3**. Cp^* = pentamethylcyclopentadienyl (**B**) Thermal ellipsoid representation (50% probability) of the molecular structure of the Dy-5* cation in **3**, as determined by x-ray crystallography (for clarity, the hydrogen atoms and $[B(C_6F_5)_4]^-$ counter anion are omitted).

The D.C. molar magnetic susceptibility (χ_M) was measured for compounds **1**-**3** in the temperature range 2 to 300 K using an applied field of 1000 Oe, and the field-dependence of the magnetization for **1** and **2** was measured at T = 2 and 5 K using fields up to 70 kOe (figs S8-S12). A description of the properties of **1** and **2** is provided in the Supplementary Materials. For **3**, the $\chi_M T$ value was measured to be 13.75 cm^3 K mol^{-1} at 300 K and then manifested a steady decrease down to 75 K. At lower temperatures a sharp drop in $\chi_M T$ was observed, indicating the onset of magnetic blocking, with a value of 0.94 cm^3 K mol^{-1} reached at 2 K. Overall, the D.C. magnetic properties of compounds **1**-**3** are typical for a monometallic complex of Dy^{3+} with a $^6H_{15/2}$ ground multiplet (*17*). The SMM properties of compounds **1**-**3** were then established through measurements of the in-phase (the real component, χ') and the out-of-phase (the imaginary component, χ'') A.C. susceptibilities as functions of the A.C. frequency (ν) and temperature, using an oscillating field of 5 Oe and zero applied D.C. field (figs S13-S28, tables

S5-S7). Focusing again on **3**, the $\chi''(\nu)$ isotherms show well-defined maxima up to 130 K (Fig. 2). The $\chi'(\nu)$ and $\chi''(\nu)$ data were then used to derive Cole-Cole plots of $\chi''(\chi')$ for relaxation in the temperature range 82 to 138 K in intervals of 2 K, with each plot adopting a parabolic shape (figs S26-S28,). Accurate fits of the A.C. susceptibility plots were obtained using equations describing χ' and χ'' in terms of frequency, the isothermal susceptibility (χ_T), adiabatic susceptibility (χ_S), the relaxation time (τ), and the fitting parameter α to represent the distribution of relaxation times (eq S1, S2) (*18*).

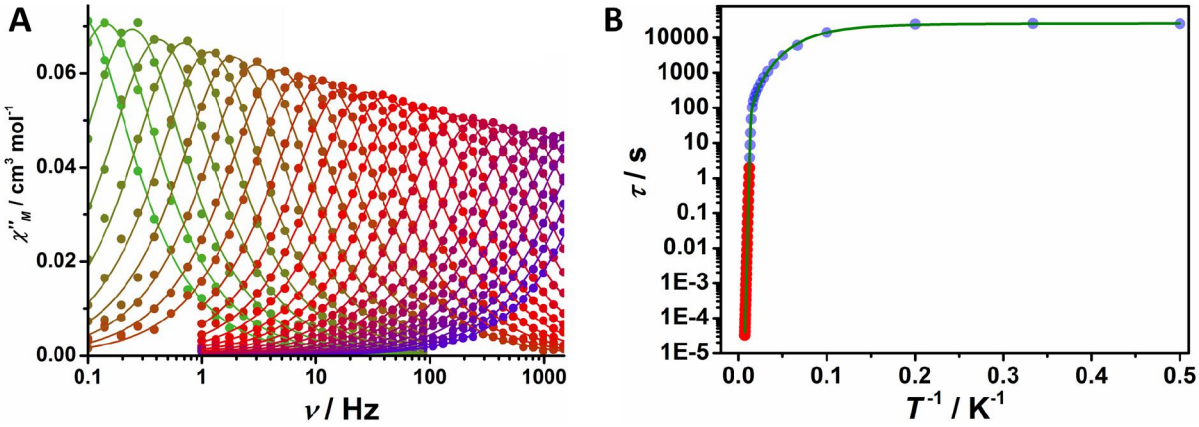

Fig. 2. Dynamic magnetic properties. (**A**) Frequency dependence of the out-of-phase χ''_M molar magnetic susceptibility for **3**, collected in zero D.C. field at A.C. frequencies of $\nu = 0.1$ to 1488 Hz from 82 K (green trace) to 138 K (purple trace) in 2 K intervals. Solid lines represent fits to the data using equations S1 and S2, with adjusted $R^2 = 0.99823$-0.99988. (**B**) Temperature dependence of the relaxation time for **3**. The red points are from the A.C. susceptibility data and the blue points are from measurements of the D.C. magnetic relaxation time. The solid green line is the best fit to $\tau^{-1} = \tau_0^{-1}e^{-U_{\mathrm{eff}}/k_{\mathrm{B}}T} + CT^n + \tau_{QTM}^{-1}$, using the parameters stated in the text.

The resulting values of $\alpha = 0$ to 0.027 indicate a very narrow range of relaxation times in the high-temperature regime. The relaxation times at temperatures in the range 2 to 83 K were determined in intervals of approximately 5 K from plots of the magnetization decay *vs.* time (figs S29-S48, table S8). These data show, for example, that the magnetization in **3** decays almost to zero over a 50-second time period at 77 K, increasing to approximately 500 minutes at 15 K. The temperature at which $\tau = 100$ s is 65 K. The relaxation times determined from the A.C. and D.C. measurements were then combined to obtain further insight into the magnetic relaxation by plotting τ as a function of T^{-1} (fig. 2), which revealed a strong, linear dependence of the relaxation time on temperature in the range 55 to 138 K. The $\tau(T^{-1})$ plot in the range 10 to 55 K is curved in nature and represents an intermediate regime before purely temperature-independent relaxation is observed below 10 K. The relaxation time can be expressed as $\tau^{-1} = \tau_0^{-1}e^{-U_{\mathrm{eff}}/k_{\mathrm{B}}T} + CT^n + \tau_{QTM}^{-1}$, in which the first term represents Orbach relaxation with U_{eff} as the effective energy barrier to relaxation of the magnetization, the second term represents the contribution from Raman processes, and the third term represents the rate of quantum tunneling of the magnetization. Using this equation, an excellent fit (adjusted $R^2 = 0.99958$) of the data was obtained with $\tau_0 = 4.2(6) \times 10^{-12}$ s, $U_{\mathrm{eff}} = 1{,}541(11)$ cm^{-1}, $C = 3.1(1) \times 10^{-8}$ s^{-1} K^{-n} and $n =$

3.0(1), and τ_{QTM} = 2.5(2) × 10^4 s. The U_{eff} value determined for **3** exceeds the value of 1,277 cm^{-1} determined for $[(Cp^{ttt})_2Dy][B(C_6F_5)_4]$ by approximately 20% (*13*).

Potential applications of SMMs in information storage devices rely on the occurrence of magnetic remanence and coercivity: therefore, the hysteresis is a critical consideration (*19*). For **3**, using a relatively fast field sweep rate of 200 Oe s^{-1} revealed $M(H)$ hysteresis from 2 K up to 85 K, with the loops gradually closing as the temperature increased (Figs 3A, 3B). At these temperature limits, coercive fields of 50 kOe and 210 Oe (5.0 T and 21 mT), respectively, were measured (Fig. 3C, fig. S49, table S9). Fixing the temperature at 77 K, a reduction in the sweep rate resulted in the coercive field approximately halving with the rate, i.e. H_c = 5,802 Oe at 700 Oe s^{-1}, 2,946 Oe at 350 Oe s^{-1}, 1,688 Oe at 200 Oe s^{-1}, 825 Oe at 100 Oe s^{-1}, 398 Oe at 50 Oe s^{-1} and 191 Oe at 25 Oe s^{-1} (fig. S50, table S10). The observation of coercivity in **3** at 25 Oe s^{-1} is significant because this sweep rate is slower than the 39 Oe s^{-1} used to determine the blocking temperature of 60 K for $[(Cp^{ttt})_2Dy][B(C_6F_5)_4]$ (*13*). At 80 K and 25 Oe s^{-1}, a coercive field of 63 Oe was measured (Fig. 3D), and the loops were completely closed at higher temperatures. Consistent with this finding, the field-cooled and zero-field-cooled magnetic susceptibilities for **3** diverged at 78 K (fig. S51). By analogy with the development of high-T_C superconductors, we propose to designate the Dy-5* cation in **3** as a high-temperature, or high-T_B, single-molecule magnet.

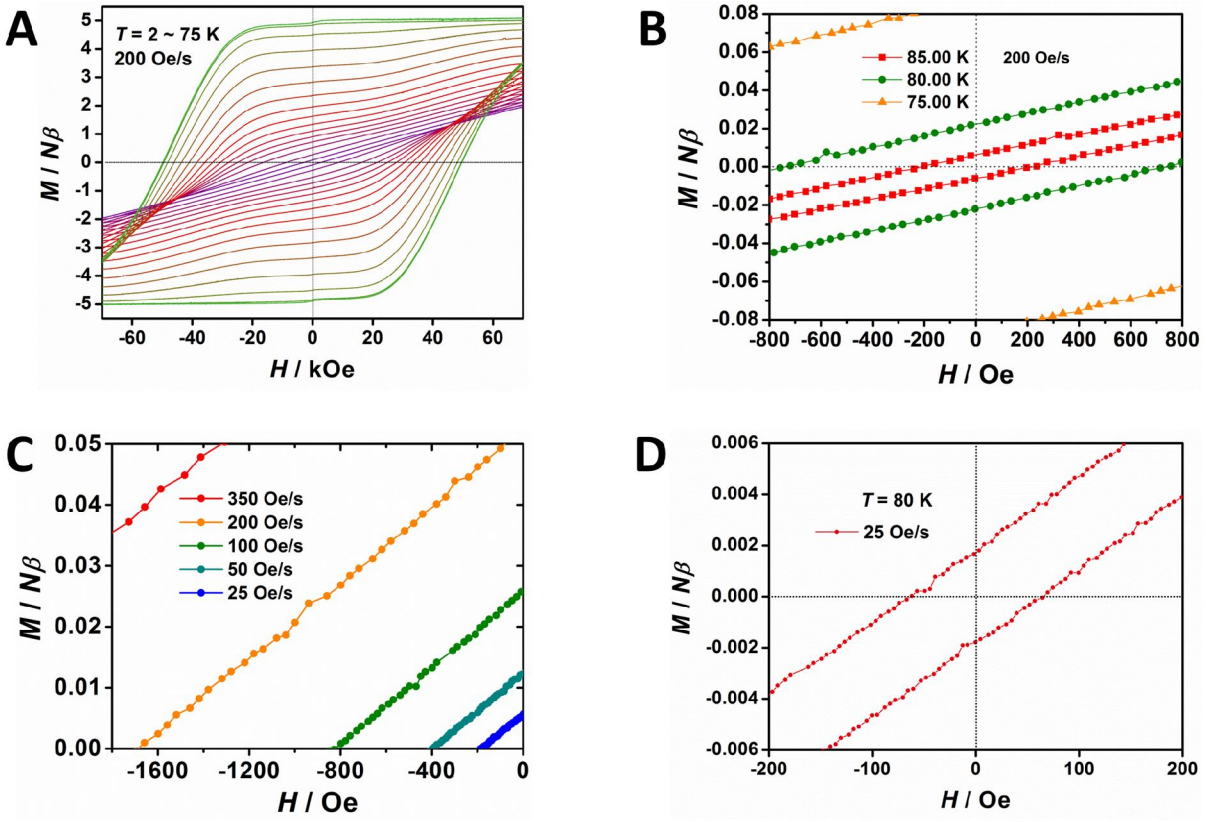

Fig. 3. Magnetic hysteresis properties of 3. Magnetization vs. field hysteresis loops in the temperature ranges of (**A**) 2 to 75 K and (**B**) 75 to 85 K using a field sweep rate of 200 Oe s^{-1}. (**C**) Expansion of the hysteresis loops at 77 K showing the coercive fields. (**D**) Hysteresis loops at 80 K using a field sweep rate of 25 Oe s^{-1}.

The importance of the strong axial crystal field in the Dy-5* cation combined with the absence of an equatorial field is illustrated further by comparing the U_{eff} and T_B values for **3** with those of the precursors **1** and **2**. In the case of **1**, the Cp^{iPr5} ligand provides a strong axial field, but the pseudo-octahedral coordination geometry introduces a non-negligible equatorial field and, whilst slow magnetic relaxation in zero field is observed with this system, the position of the maxima in $\chi''(\nu)$ are temperature-independent up to 10 K and only observed up to 30 K (figs S13-S16). The resulting energy barrier of 241(7) cm^{-1} is comparatively small, and the rate of quantum tunnelling of the magnetization (QTM) is, at $5.0(1) \times 10^{-3}$ s (fig. S17), some seven orders of magnitude faster than found with **3**. The competing equatorial field in **2** is more prominent as the maxima in $\chi''(\nu)$ are very weakly temperature-dependent from 3 to 20 K, with the resulting energy barrier a negligible 7(1) cm^{-1} (figs S19-S22). In both **1** and **2**, the $M(H)$ hysteresis loops collected at 2 K and 200 Oe s^{-1} are waist-restricted, with no coercivity and only small openings as the field magnitude increases (figs S18, S23).

Ab initio calculations have enabled quantitative analysis of the properties of SMMs on a microscopic scale (*20*), particularly systems with η^n-bonded organometallic ligands (*21-30*). Calculations on the Dy-5* cation were performed at the XMS-CASPT2//SA-CASSCF/RASSI level (*31, 32*): the resulting energies, principal components of the ***g***-tensors and the principal magnetic axes of the eight lowest Kramers' doublets in Dy-5* corresponding to the CF-split states of the $^6H_{15/2}$ ground multiplet are listed in table S11. The principal magnetic axis in the ground doublet of Dy-5* (Fig. 4) is projected towards the centroids of the two cyclopentadienyl ligands, with the principal axes of the next six doublets almost collinear and the largest deviation angle 5.3° with the fifth doublet. The highest doublet is perpendicular to the ground doublet.

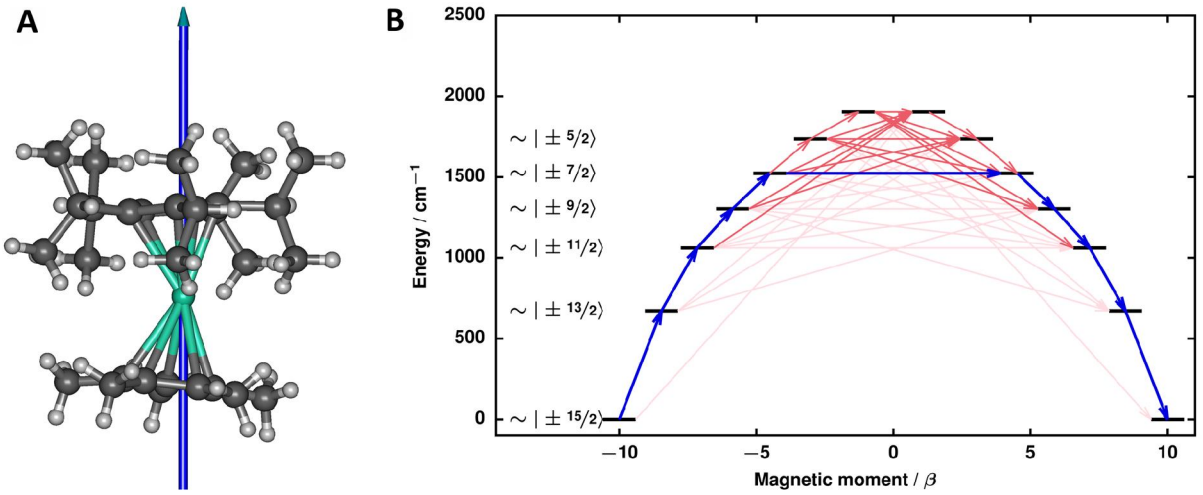

Fig. 4. Magnetic relaxation in the Dy-5* cation. (**A**) The principal magnetic axis of the ground Kramers' doublet. (**B**) Relaxation mechanism for Dy-5*. Blue arrows show the most probable relaxation route and red arrows show transitions between states with less probable but non-negligible matrix elements: darker shading indicates a higher probability.

The ***g***-tensor of the ground doublet is calculated to be perfectly axial, i.e. $g_x = g_y = 0.000$ and $g_z = 20.000$ (table S11), which is consistent with the experimental hysteresis measurements in which QTM is completely blocked at zero field. In the six lowest doublets, the CF is highly axial and each state can be assigned to a definite projection (greater than 96% character) of the total angular

momentum, M_J (table S12). The transverse components of the ***g***-tensors increase roughly by an order of magnitude in each doublet upon moving to higher energy. In the fifth doublet the transverse components start to become significant and in the sixth doublet the transverse components are large enough to allow considerable tunneling. In the two highest states, the axiality is weaker and considerable mixing occurs under the CF, which most likely results from the asymmetry of the coordination environment.

The *ab-initio* CF parameters were calculated for the Dy-5* cation following a previously established methodology (*33, 34*) and are listed in table S13. The off-diagonal elements of the CF operator clearly have non-negligible elements due to the low C_1 point symmetry of Dy-5*, however the axial second-rank parameter B_2^0 is at least two orders of magnitude larger than any other parameter. This creates a highly axial CF environment despite the absence of point symmetry (or pseudo-symmetry) that would be needed for a strictly axial CF. The off-diagonal elements of the CF play some role and, in the higher-lying doublets of the ground multiplet, the axial nature of the CF is lost (*vide infra*). This demonstrates that strict point symmetry is not required to achieve a highly axial CF, provided the axial parameters are sufficiently strong in comparison to the other CF parameters arising from the low-symmetry components of the CF.

The magnetic relaxation in the Dy-5* cation was studied further by constructing a qualitative relaxation barrier from the *ab initio* results, which follows a methodology in which the transition magnetic moment between the different states was calculated and the relaxation pathway follows the largest matrix elements (Fig. 4B, table S14) (*35*). The results predict that the barrier is crossed at the fourth excited doublet, corresponding to a U_{eff} value of 1,524 cm^{-1} for the Orbach process, which is consistent with the calculated ***g***-tensors for this doublet and is in excellent agreement with the experimentally determined barrier height of 1,541(11) cm^{-1}. To gain deeper insight into the nature of the spin-phonon relaxation, the first-order spin-phonon couplings with the optical phonons (approximated as the molecular vibrations) were evaluated from first-principles calculations (tables S15-S18). In earlier work on $[(Cp^{ttt})_2Dy]^+$ (*14*), vibrations of the C–H oscillators in the Cp rings were recognized as the most important contribution to the Orbach relaxation as they initiated the transition from the ground doublet to the first excited doublet. In the case of Dy-5*, these oscillators are absent, and the analogous transition from the ground to the first excited doublet is most likely initiated by out-of-plane vibrations of the Cp^* ligand when comparing the frequency of these modes (632.9 cm^{-1} and 640.5 cm^{-1}) to the calculated gap between the ground and first-excited doublets (672 cm^{-1}) (see Movies S1-S7). Because the out-of-plane vibrations couple strongly to vibrations of the Cp^* methyl groups, it is conceivable that their energies can be tuned by choosing ligand substituents that would bring the vibrational modes out of resonance with the excitation gap. Such an approach should lead to further improvements in SMM performance beyond those of the Dy-5* cation, and therefore enhance their potential for applications in magnetic information storage materials.

References and Notes:

1. N. Ishikawa, M. Sugita, T. Ishikawa, S. Koshihara, Y. Kaizu, *J. Am. Chem. Soc.* **125**, 8694 (2003).
2. B. M. Day, F.-S. Guo, R. A. Layfield *Acc. Chem. Res*. **51**, 1880 (2018).
3. J.-L. Liu, Y.-C. Chen, M.-L. Tong, *Chem. Soc. Rev*. **7**, 2431 (2018).
4. J. M. Frost, K. L. M. Harriman, M. Murugesu, *Chem. Sci*. **7**, 2470 (2016).
5. M. Shiddiq, D. Komijani, Y. Duan, A. Gaita-Ariño, E. Coronado, S. Hill, *Nature* **531**, 348 (2016)
6. S. Thiele, F. Balestro, R. Ballou, S. Klyatskaya, M. Ruben, W. Wernsdorfer, *Science* **344**, 1135 (2014)
7. D. N. Woodruff, R. E. P. Winpenny, R. A. Layfield. *Chem. Rev*. **113**, 5110 (2013).
8. P. Zhang, L. Zhang, J. Tang, *Dalton Trans*. **44**, 3923 (2015).
9. J. D. Rinehart, M. Fang, W. J. Evans J. R. Long, *J. Am. Chem. Soc.* **133**, 14236 (2011).
10. Y.-C. Chen, J.-L. Liu, L. Ungur, J. Liu, Q.-W. Li, L.-F. Wang, Z.-P. Ni, L. F. Chibotaru, X.-M. Chen, M.-L. Tong, *J. Am. Chem. Soc.* **138**, 2829 (2016).
11. S. K. Gupta, T. Rajeshkumar, G. Rajaraman, R. Murugavel, *Chem. Sci*. **7**, 5181 (2016).
12. F. Liu, D. S. Krylov, L. Spree, S. M. Avdoshenko, N. A. Samoylova, M. Rosenkranz, A. Kostanyan, T. Greber, A. U. B. Wolter, B. Büchner, A. A. Popov, *Nat. Commun*. **8**, 16098 (2017).
13. F.-S. Guo, B. M. Day, Y.-C. Chen, M.-L. Tong, A. Mansikkamäki, R. A. Layfield, *Angew. Chem. Int. Ed*. **56**, 11445 (2017).
14. C. A. P. Goodwin, F. Ortu, D. Reta, N. F. Chilton, D. P. Mills, *Nature* **548**, 439 (2017).
15. C. A. P. Goodwin, D. Reta, F. Ortu, N. F. Chilton, D. P. Mills, *J. Am. Chem. Soc.* **139**, 18714 (2017).
16. S. J. Connelly, W. Kaminsky, D. M. Heinekey, *Organometallics* **32**, 7478 (2013).
17. C. Benelli, D. Gatteschi, *Introduction to Molecular Magnetism: From Transition Metals to Lanthanides*, Wiley-VCH, Weinheim, 2015.
18. Y.-N. Guo, G.-F. Xu, Y. Guo, J. Tang, *Dalton Trans*. **40**, 9953 (2011).
19. S. Demir, M. I. Gonzalez, L. E. Darago, W. J. Evans, J. R. Long, *Nat. Commun*. **8**, 2144 (2017).
20. L. Ungur, L. F. Chibotaru, *Inorg. Chem*. **55**, 10043 (2016).
21. L. Ungur, J. J. Le Roy, I. Korobkov, M. Murugesu, *Angew. Chem. Int. Ed*. **53**, 4413 (2014).
22. J. J. Le Roy, L. Ungur, I. Korobkov, L. F. Chibotaru, M. Murugesu, *J. Am. Chem. Soc*. **136**, 8003 (2014).
23. J. J. Le Roy, M. Jeletic, S. I. Gorelsky, I. Korobkov, L. Ungur, L. F. Chibotaru, M. Murugesu, *J. Am. Chem. Soc*. **135**, 3502 (2013).
24. K. L. M. Harriman, J. J. Le Roy, L. Ungur, R. Holmberg, I. Korobkov, M. Murugesu, *Chem. Sci*. **8**, 231 (2017).
25. T. P. Latendresse, N. S. Bhuvanesh, M. Nippe, *J. Am. Chem. Soc*. **139**, 14877 (2017).
26. T. Pugh, N. F. Chilton, R. A. Layfield, *Angew. Chem. Int. Ed*. **55**, 11082 (2016).
27. T. Pugh, F. Tuna, L. Ungur, D. Collison, E. J. L. McInnes, L. F. Chibotaru, R. A. Layfield, *Nat. Commun*. **6**, 7492 (2015).
28. T. Pugh, V. Vieru, L. F. Chibotaru, R. A. Layfield, *Chem. Sci*. **7**, 2128 (2016).
29. T. Pugh, N. F. Chilton, R. A. Layfield, *Chem. Sci*. **8**, 2073 (2017).
30. A. F. R. Kilpatrick, F.-S. Guo, B. M. Day, A. Mansikkamäki, R. A. Layfield F. G. N. Cloke, *Chem. Commun*. **54**, 7085 (2018).

31. L. Ungur, L. F. Chibotaru, *Computational Modelling of Magnetic Properties of Lanthanide Compounds in Lanthanide and Actinides* in *Molecular Magnetism*. R. A. Layfield, M. Murugesu (Eds,. Wiley-VCH, Weinheim, Germany, 2015.
32. T. Shiozaki, W. Gyõrffy, P. Celani, H.-J. Werner. *J. Chem. Phys*. **135**, 081106 (2011).
33. L. Ungur, L. F. Chibotaru. *Chem. Eur. J.* **23**, 3708 (2017).
34. L. F. Chibotaru in *Advances in Chemical Physics*, *Ab initio Methodology for Pseudospin Hamiltonians of Anisotropic Magnetic Complexes*, Vol. 153 (Eds.: S. A. Rice, A. R. Dinner), Wiley, New York, **2013**, pp. 397–519.
35. L. Ungur, M. Thewissen, J.-P. Costes, W. Wernsdorfer, L. F. Chibotaru, *Inorg. Chem.* **52**, 6328 (2013).

Acknowledgments: The authors thank the CSC-IT Center for Science in Finland, the Finnish Grid and Cloud Infrastructure (persistent identifier urn:nbn:fi:research-infras-2016072533), and Prof. H. M. Tuononen (University of Jyväskylä) for providing computational resources.

Funding: The authors thank the European Research Council (CoG grant 646740), the EPSRC (EP/M022064/1), the NSF China (projects 21620102002, 91422302), the National Key Research and Development Program of China (2018YFA0306001) and the Academy of Finland (projects 282499, 289172).

Author contributions: R.A.L. conceived the original idea and formulated the research aims. Synthetic and crystallographic work was carried out by F.-S.G. and B.M.D. Magnetic measurements were conducted by Y.-C.C. and M.-L.T. The theoretical analysis was carried out by A.M. All authors analyzed the data. R.A.L. wrote the manuscript, with contributions from all authors.

Competing interests: The authors declare no competing interests.

Data and materials availability: Metrical data for the solid-state structures of **1**-**3** are available free of charge from the Cambridge Crystallographic Data Centre under reference numbers CCDC 1854466-1854468. All other data are in the main text supplementary materials.

Supplementary Materials:

Materials and Methods

Figures S1-S51

Tables S1-S18

References (*36*-*76*)

Movies S1-S7

Data S1-S3

Science
AAAS

Supplementary Materials for

Magnetic hysteresis up to 80 K in a dysprosium metallocene single-molecule magnet

Fu-Sheng Guo, Benjamin M. Day, Yan-Cong Chen, Ming-Liang Tong, Akseli Mansikkamäki, Richard A. Layfield.

Correspondence to: R.Layfield@sussex.ac.uk

This PDF file includes:

Other Supplementary Materials for this manuscript include the following:

Movies S1 to S7
Data S1 to S3: optimized_geometry.xyz
displacements.xyz
magnetism data.xls

Materials and Methods

General Procedures

All reactions were carried out under rigorous anaerobic, anhydrous conditions under argon or nitrogen atmospheres using standard Schlenk line and glovebox techniques. All solvents were refluxed over an appropriate drying agent for a minimum of three days (molten potassium for toluene and benzene, Na/K alloy for hexane, CaH_2 for CH_2Cl_2) before distilling, and were stored in ampoules over activated 4 Å molecular sieves (toluene, hexane, benzene, CH_2Cl_2). $NaCp^{iPr5}$ (*36*), $Dy(BH_4)_3(THF)_3$ (*37*), KCp* (*38*) and $[Et_3Si(H)SiEt_3][B(C_6F_5)_4]$ (*15*) were prepared according to literature procedures. Elemental analyses were carried out at London Metropolitan University, U.K. IR spectra were collected on a Bruker Alpha FTIR spectrometer fitted with a Platinum ATR module.

Synthesis of $[Cp^{iPr5}Dy(BH_4)_2THF]$ (1): Toluene (15 ml) was added to an ampoule containing a mixture of $NaCp^{iPr5}$ (895 mg, 3.0 mmol), $Dy(BH_4)_3(THF)_3$ (1328 mg, 3.0 mmol) and a glass coated stirrer bar, and the resulting suspension was stirred at room temperature overnight. The toluene was removed under vacuum and the product was extracted into hexane (3 × 10 mL) and filtered. The filtrate was concentrated *in vacuo* until incipient crystallisation occurred. The solution was then gently warmed to re-dissolve the microcrystalline solid and the solution was stored at –40°C overnight, yielding pale yellow crystals of **1**. Yield = 1166 mg, 72 %. Elemental analysis found (calcd.) % for $C_{24}H_{51}B_2ODy$: C 52.13 (53.40); H 9.67 (9.52). IR spectra (cm^{-1}): 2973s, 2929s, 2871s, 2462s, 2364w, 2309m, 2262w, 2198m, 2131s, 1458s, 1365s, 1320w, 1252m, 1194s, 1175s, 1098s, 1083s, 1041m, 1004s, 957w, 909m, 856s, 749w, 666m, 545m, 525s, 484s, 454s.

Synthesis of $[Cp^{iPr5}DyCp^*(BH_4)]$ (2): Toluene (15 ml) was added to an ampoule containing a mixture of **1** (532 mg, 1.0 mmol), KCp* (174 mg, 1.0 mmol) and a glass coated stirrer bar, and the resulting suspension was stirred at 110°C for two days. The toluene was removed under vacuum and the product was extracted into hexane (3 × 10 mL) and filtered. After removal of the solvent, a yellow powder was obtained and recrystallized from hexane at –40 °C to yield yellow crystals of **2**. Yield = 190 mg, 32 %. Elemental analysis found (calcd.) % for $C_{30}H_{54}BDy$: C 61.03(61.27); H 9.39 (9.26). IR spectra (cm^{-1}): 2966s, 2908s, 2866s, 2441m, 2398m, 2294w, 2248w, 2133m, 2038w, 1998w, 1446m, 1380s, 1366s, 1295w, 1218w, 1197w, 1158m, 1129s, 1090m, 1058w, 1030w, 955w, 906w, 861w, 803w, 768w, 710w, 595w, 542w, 504s, 452w.

Synthesis of $[Cp^{iPr5}DyCp^*][B(C_6F_5)_4]$ (3): Cold (–40 °C) hexane (10 ml) was added into a cold ampoule containing $[Et_3Si(H)SiEt_3][B(C_6F_5)_4]$ (180 mg, 0.20 mmol) and a glass coated stirrer bar. Then, a cold (–40 °C) hexane (10 ml) solution of $[Cp^{iPr5}DyCp^*(BH_4)]$ (118 mg, 0.2 mmol) was slowly added to the ampoule, then the resulting suspension was sonicated for three minutes and stirred overnight to give a yellow solid. After letting the solid settle, as much of the solution as possible was decanted away and hexane (10 ml) was added. This was repeated five times before removal of residual volatiles *in vacuo* gave a yellow solid. A crystalline sample of **3** was obtained by storing a saturated dichloromethane solution at –40°C overnight. Isolated crystalline yield = 150 mg, 60 %. Elemental analysis found (calcd.)% for $C_{54}H_{50}BDyF_{20}$: C: 51.63 (51.79); H 4.11 (4.02). IR spectra (cm^{-1}): 2990w, 2970w, 2875w, 2792w, 1641m, 1512s, 1458s, 1424m, 1384m, 1371m, 1310w, 1277m, 1159w, 1084s, 1031w, 978s, 904w, 799w, 775s, 756s, 726w, 684s, 660s, 610w, 573m, 506m, 476w.

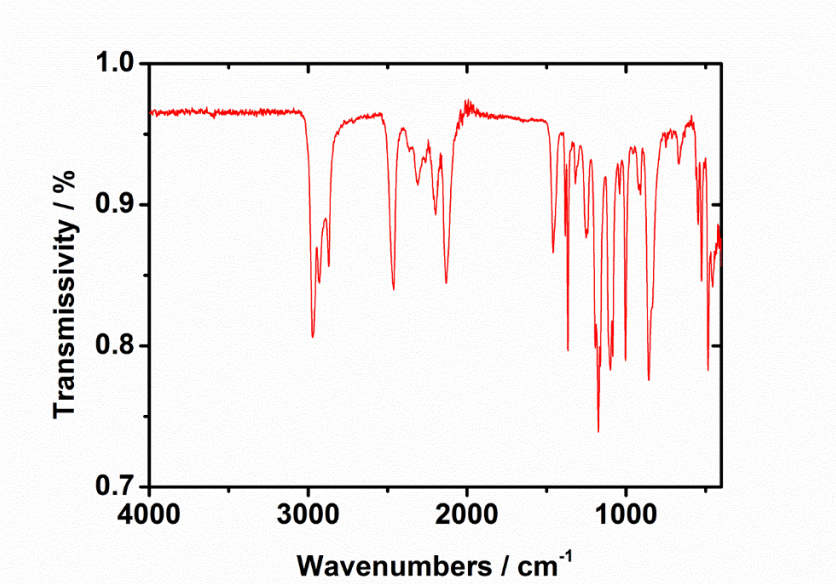

Fig. S1. Infrared spectrum of compound **1**.

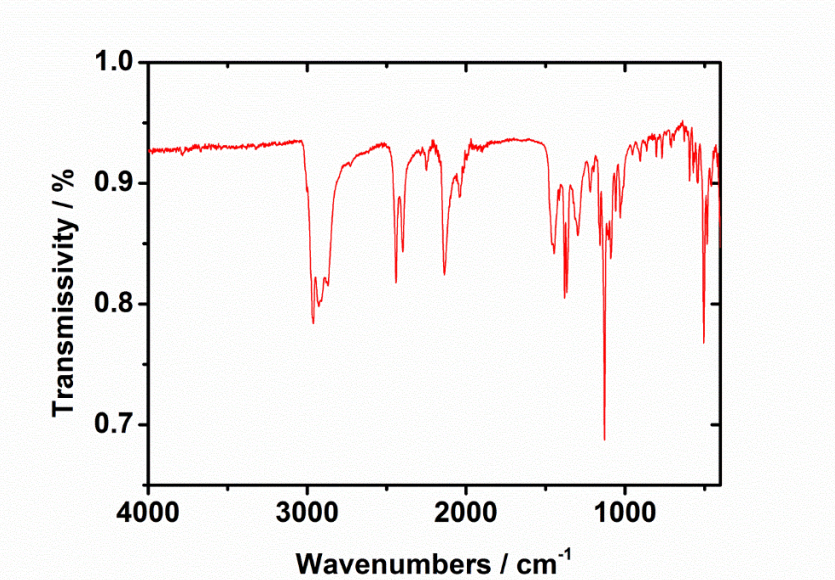

Fig. S2. Infrared spectrum of compound **2**.

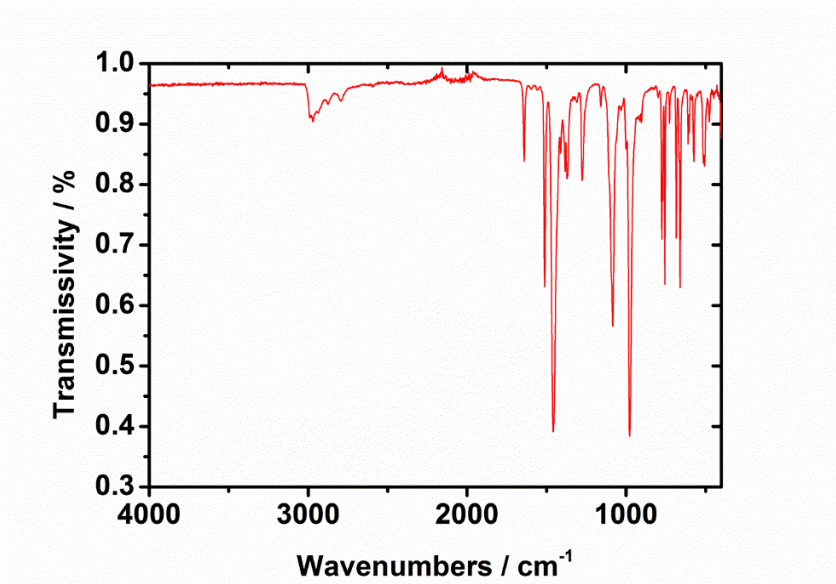

Fig. S3. Infrared spectra of compound **3**.

X-ray crystallography

Single-crystal x-ray diffraction measurements for compound **1-3** were carried out on an Agilent SuperNova diffractometer with graphite monochromated MoKα radiation (λ = 0.71073 Å) at 150 K. Structures were solved in Olex2, either with SHELXS using direct methods or with SHELXT using intrinsic phasing and were refined with SHELXL using least squares minimisation (*39-41*). Anisotropic thermal parameters were used for the non-hydrogen atoms and isotropic parameters for the hydrogen atoms. Hydrogen atoms on carbons were added geometrically and refined using a riding model. Hydrogen atoms for BH_4 fragments in compounds **1-2** could be located from the Q peaks around B atoms and were isotropically refined.

Table S1. Crystal Data and Structure Refinement for **1-3**.

Compound reference	**1**	**2**	**3**
Chemical formula	$2(C_{24}H_{51}B_2DyO)$	$C_{30}H_{54}BDy$	$C_{30}H_{50}Dy{\cdot}BC_{24}F_{20}$
Formula Mass	1079.53	588.04	1252.25
Crystal system	Monoclinic	Monoclinic	Monoclinic
a/Å	9.9666(3)	17.3203(4)	17.3982(7)
b/Å	33.7738(10)	10.3090(2)	13.3024(3)
c/Å	16.3084(8)	16.7462(3)	22.8707(6)
α/°	90	90	90
β/°	94.047(4)	102.635(2)	107.490(4)
γ/°	90	90	90
Unit cell volume/Å^3	5475.9(4)	2917.71(10)	5048.4(3)
Temperature/K	150.0(3)	150.0(3)	150.0(4)
Space group	$P2_1/c$	$P2_1/c$	$P2_1/c$
No. of formula units per unit cell, Z	4	4	4
ρ_{calc}/g cm^{-3}	1.309	1.339	1.648
Absorption coefficient, μ/mm^{-1}	2.740	2.575	1.592
F(000)	2232.0	1220.0	2500.0
Crystal size/mm^3	0.2 × 0.18 × 0.03	0.15 × 0.15 × 0.05	0.12 × 0.1 × 0.08
2θ range for data collection/°	5.436 to 51.998	5.502 to 53	5.61 to 52.994
No. of reflections measured	24697	13185	20241
No. of independent reflections	10766	6023	10452
R_{int}	0.0608	0.0289	0.0386
Final R_1 values ($I > 2\sigma(I)$)*	0.0503	0.0274	0.0666
Final $wR_2(F^2)$ values ($I > 2\sigma(I)$)	0.0748	0.0539	0.1298
Final R_1 values (all data)	0.0804	0.0369	0.0864
Final $wR_2(F^2)$ values (all data)†	0.0879	0.0582	0.1420
Goodness of fit on F^2	1.066	1.041	1.097

*$R_1 = \sum||F_o|-|F_c||/\sum|F_o|$, †$wR_2 = [\sum w(F_o^2-F_c^2)^2/\sum w(F_o^2)^2]^{1/2}$

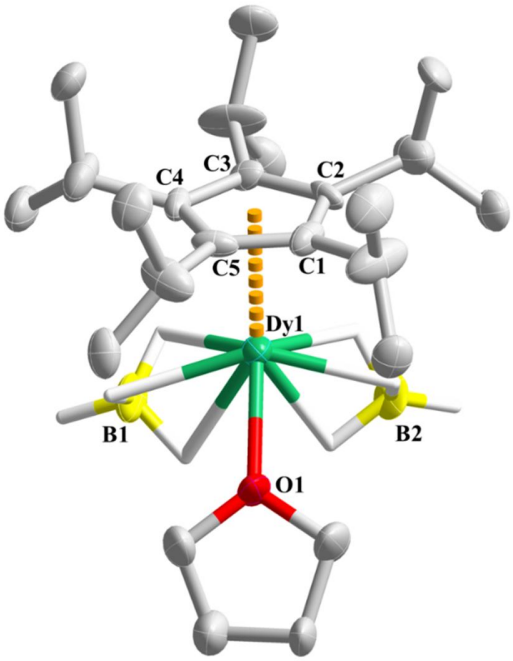

Fig. S4. Thermal ellipsoid representation of the molecular structure of **1** shown at the 50% probability level, hydrogen atoms on carbon groups are omitted for clarity. Colour scheme: Dy, green; C, grey; O, red; B, yellow; H, white.

Table S2. Selected bond lengths (Å) for compound **1**.‡

Molecule A		**Molecule B (disordered part 1)**		**Molecule B (disordered part 2)**	
Dy1-C1	2.633(5)	Dy2-C25	2.683(11)	Dy2-C25A	2.686(3)
Dy1-C2	2.683(6)	Dy2-C26	2.681(13)	Dy2-C26A	2.632(4)
Dy1-C3	2.678(6)	Dy2-C27	2.654(19)	Dy2-C27A	2.633(3)
Dy1-C4	2.671(6)	Dy2-C28	2.608(19)	Dy2-C28A	2.687(5)
Dy1-C5	2.639(6)	Dy2-C29	2.667(14)	Dy2-C29A	2.719(1)
Dy1-O1	2.408(5)	Dy2-O2	2.371(5)		
Dy1-Cp_{centA}	2.377(1)	Dy2-Cp_{cent}	2.365(1)	Dy2-Cp_{cent}	2.383(1)

‡There are two unique molecules in the asymmetric unit of **1**, one of which (molecule B) features a Cp^{iPr5} ligand disordered over two sites.

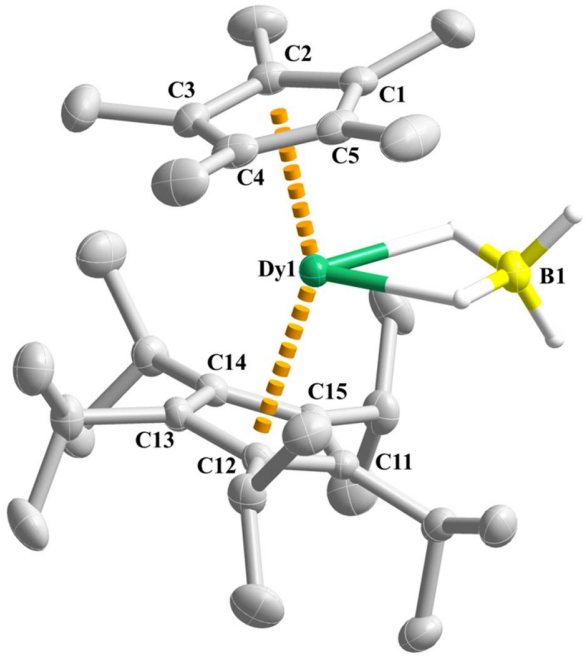

Fig. S5. Thermal ellipsoid representation of the molecular structure of **2** shown at the 50% probability level, hydrogen atoms on carbon groups are omitted for clarity. Colour scheme: Dy, green; C, grey; B, yellow; H, white.

Table S3. Selected bond lengths (Å) and angles (°) for compound **2**.

Dy1-C1	2.660(3)
Dy1-C2	2.660(3)
Dy1-C3	2.677(3)
Dy1-C4	2.640(3)
Dy1-C5	2.626(3)
Dy1–Cp* (centroid)	2.364(1)
Dy1-C11	2.677(3)
Dy1-C12	2.671(3)
Dy1-C13	2.685(3)
Dy1-C14	2.682(3)
Dy1-C15	2.660(3)
Dy1–Cp^{iPr5} (centroid)	2.382(1)
Cp-Dy1-Cp	150.289(1)

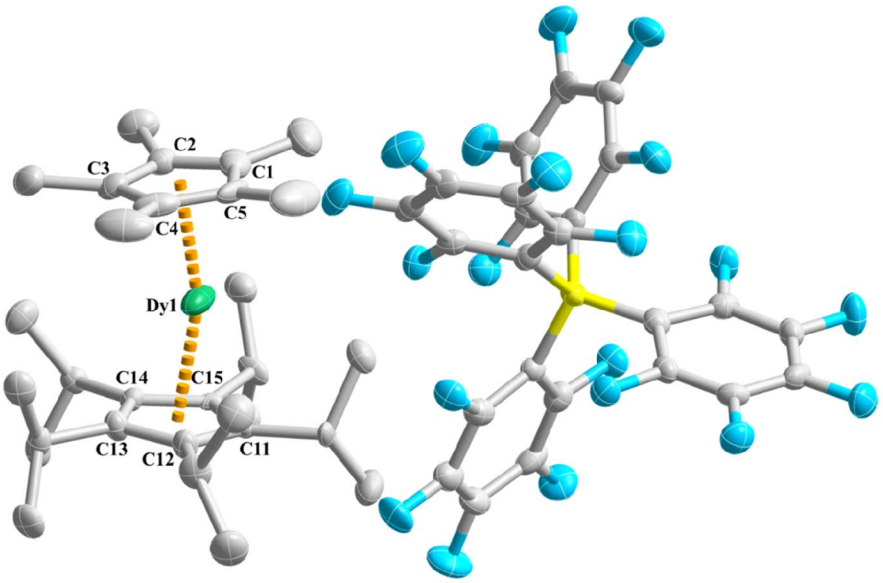

Fig. S6. Thermal ellipsoid representation of the molecular structure of **3** shown at the 50% probability level, hydrogen atoms on carbon groups are omitted for clarity. Colour scheme: Dy, green; C, grey; B, yellow; F, light blue.

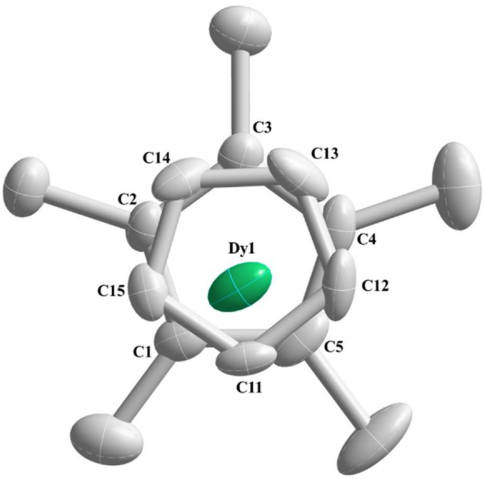

Fig. S7. View of core of Dy-5*, with thermal ellipsoids set at 50% probability. ^{i}Pr Groups on the Cp ring and all hydrogen atoms are omitted for clarity. Color schemes for the structure: Dy, green; C, gray.

Table S4. Selected bond lengths (Å) and angles (°) for compound **3** and compound **2** for comparison.

	3	**2**	**Δ**
Dy1–C1	2.551(6)	2.660(3)	0.109
Dy1–C2	2.604(6)	2.660(3)	0.056
Dy1-C3	2.651(6)	2.677(3)	0.026
Dy1–C4	2.598(6)	2.640(3)	0.042
Dy1–C5	2.550(6)	2.626(3)	0.076
Dy1–Cp* (centroid)	2.296(1)	2.364(1)	0.068
Dy1–C11	2.513(6)	2.677(3)	0.164
Dy1–C12	2.586(7)	2.671(3)	0.084
Dy1–C13	2.653(7)	2.685(3)	0.032
Dy1–C14	2.612(6)	2.682(3)	0.07
Dy1–C15	2.525(6)	2.660(3)	0.135
Dy1–Cp^{iPr5} (centroid)	2.284(1)	2.382(1)	0.098
Cp*-Dy1-Cp^{iPr5}	162.507(1)	150.289(1)	-12.218

Magnetic property measurements

Samples of **1-3** were prepared by adding crushed crystalline samples and eicosane into 7mm NMR tubes. The tubes were evacuated and flame sealed. The eicosane was melted in a water bath 40 °C to prevent crystallite torqueing. The direct current (D.C.) magnetic susceptibility and magnetization data were collected using a Quantum Design MPMS3-VSM SQUID magnetometer in cooling mode. Alternating current (A.C.) magnetic susceptibility measurements were performed using a Quantum Design MPMS XL-7 SQUID magnetometer using an oscillating field of 5 Oe. Measurements of the magnetization decay were performed by first magnetizing the sample in a field of 70 kOe, and then removing the field and measuring the magnetization over time with the VSM option. Diamagnetic corrections were performed using Pascal's coefficients (*42*).

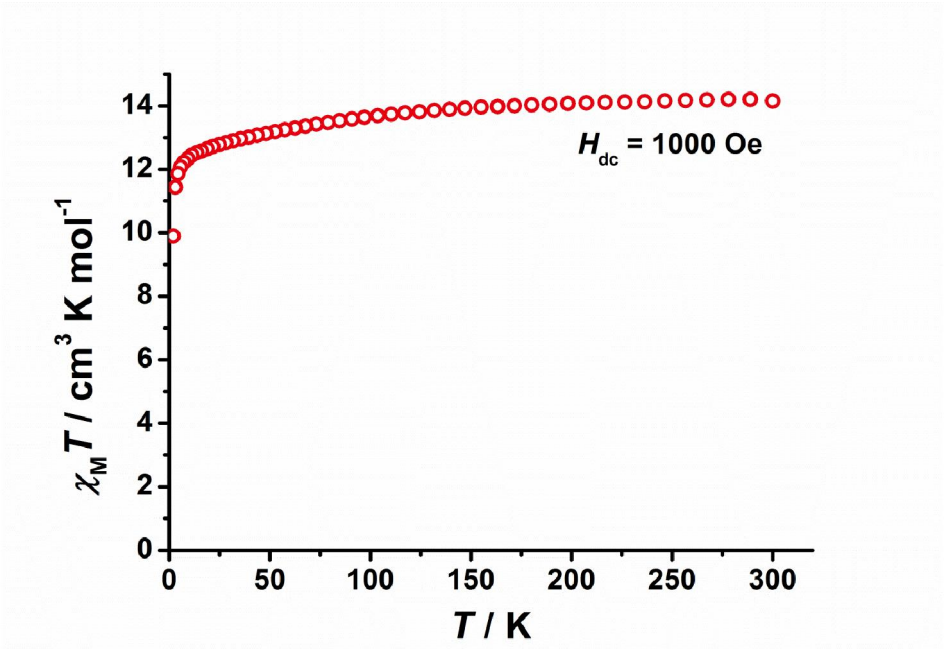

Fig. S8. Plot of $\chi_M T$ versus temperature for **1** in an applied magnetic field of 1 kOe. $\chi_M T$(300 K) = 14.15 cm^3 K mol^{-1}, $\chi_M T$(2 K) = 9.90 cm^3 K mol^{-1}.

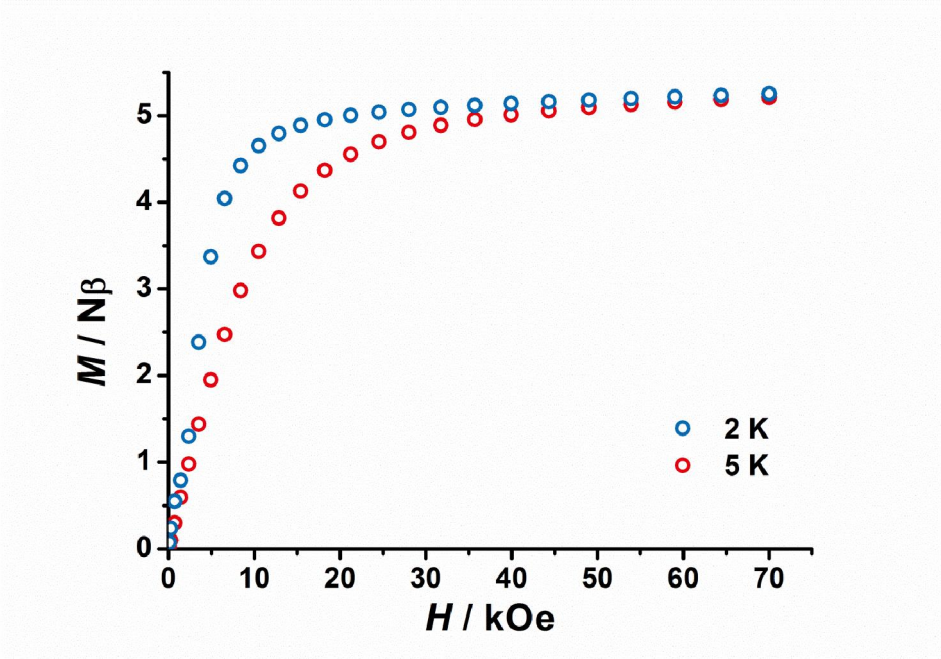

Fig. S9. Field dependence of the magnetization, *M*, at 2 K (blue circles) and 5 K (red circles) for **1**. *M* = 5.25 Nβ at 2 K and 70 kOe.

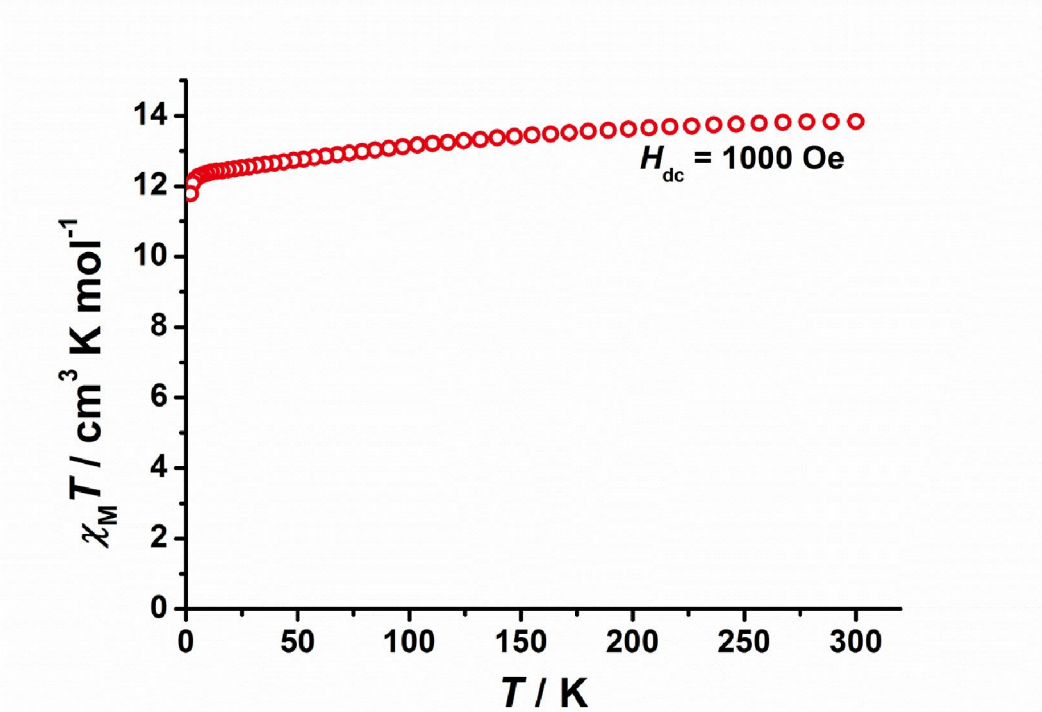

Fig. S10. Plot of $\chi_M T$ versus temperature for **2** in an applied magnetic field of 1 kOe. $\chi_M T$(300 K) = 13.84 cm^3 K mol^{-1}, $\chi_M T$(2 K) = 11.78 cm^3 K mol^{-1}.

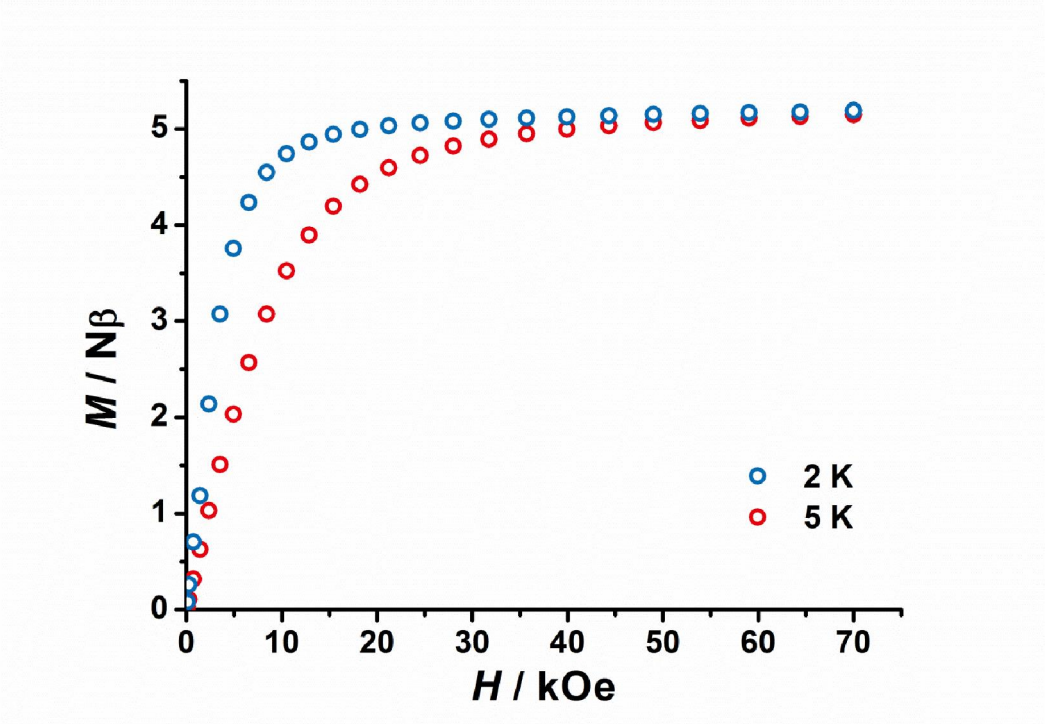

Fig. S11. Field dependence of the magnetization, *M*, at 2 K (blue circles) and 5 K (red circles) for **2**. *M* = 5.19 Nβ at 2 K and 70 kOe.

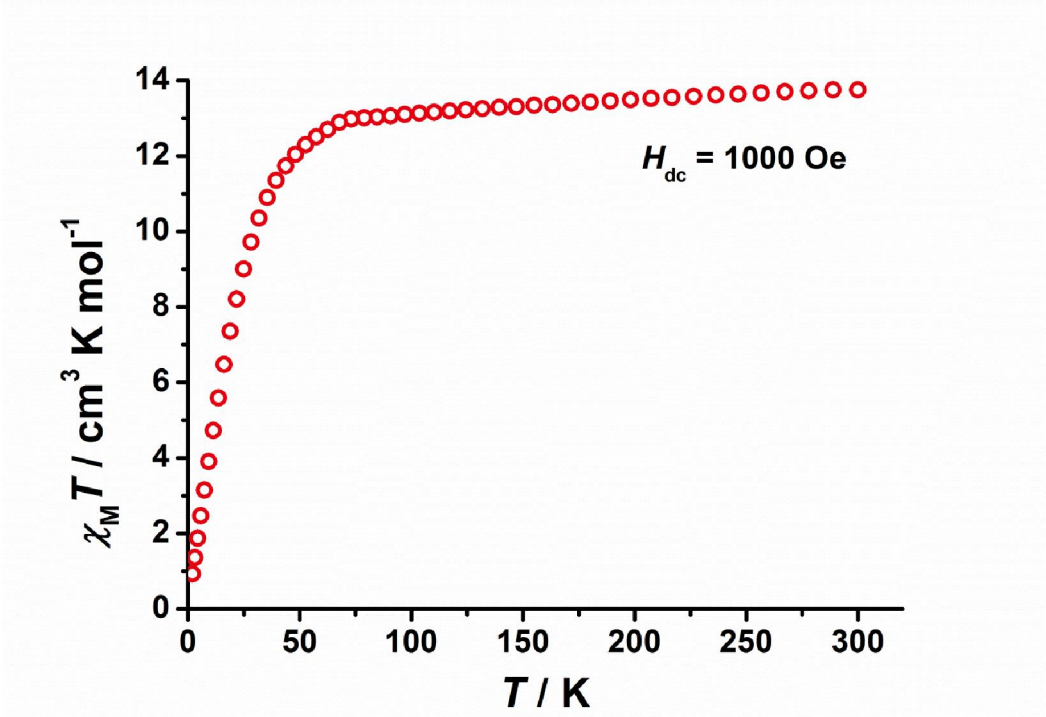

Fig. S12. Plot of $\chi_M T$ versus temperature for **3** in an applied magnetic field of 1 kOe. $\chi_M T$(300 K) = 13.75 cm^3 K mol^{-1}, $\chi_M T$(2 K) = 0.94 cm^3 K mol^{-1}.

5

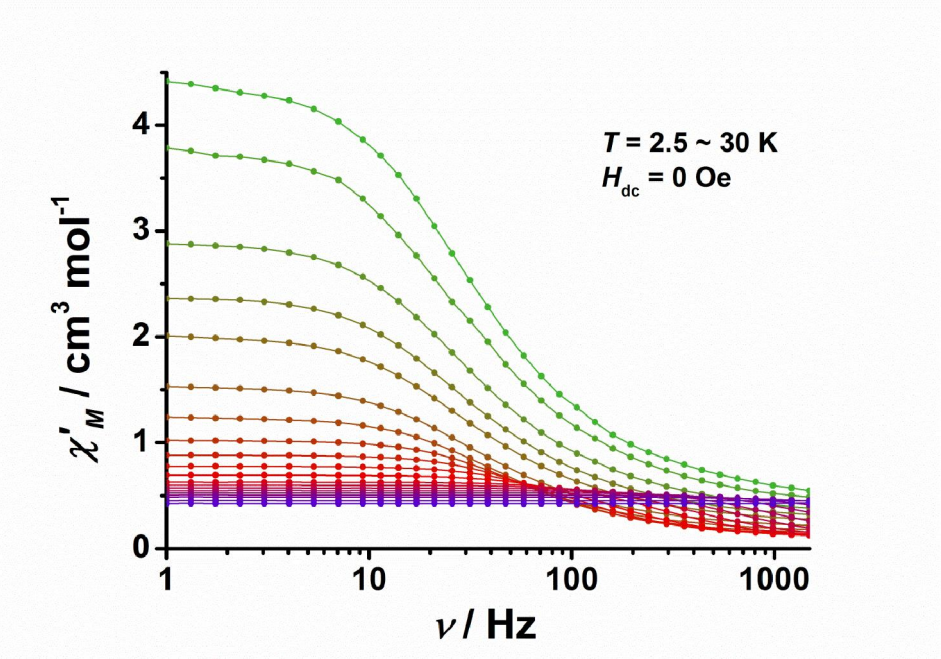

Fig. S13. Frequency dependence of the in-phase susceptibility (χ'_M) for **1** in zero DC field at AC frequencies of 1-1488 Hz from 2.5 to 30 K. Solid lines are a guide to the eye.

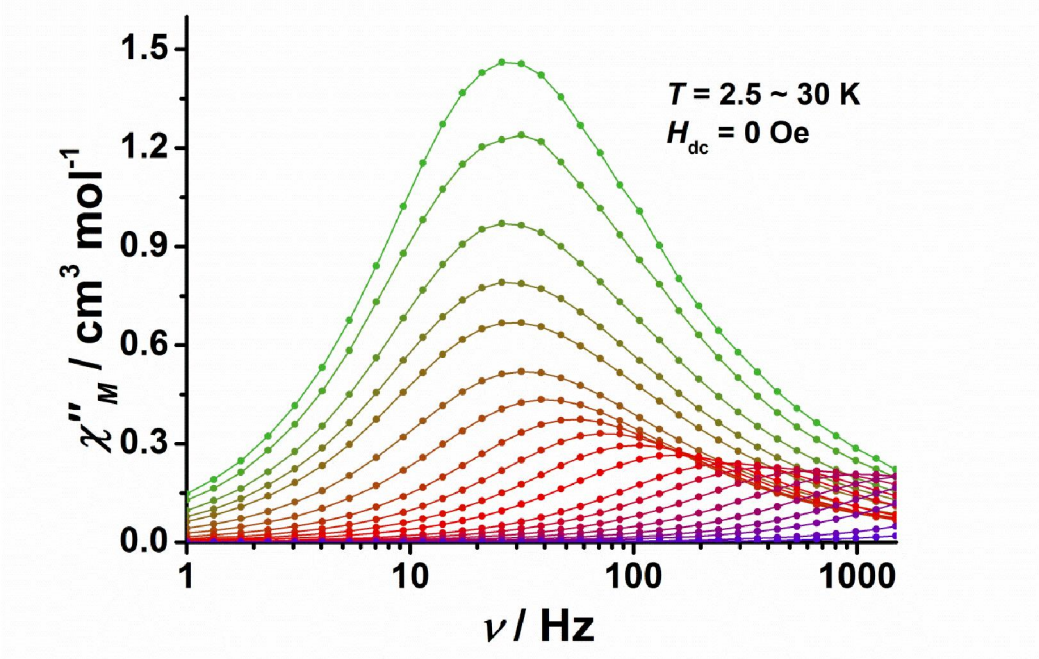

Fig. S14. Frequency dependence of the out-of-phase susceptibility (χ''_M) in zero DC field at AC frequencies of 1-1488 Hz from 2.5 to 30 K. Solid lines are a guide to the eye.

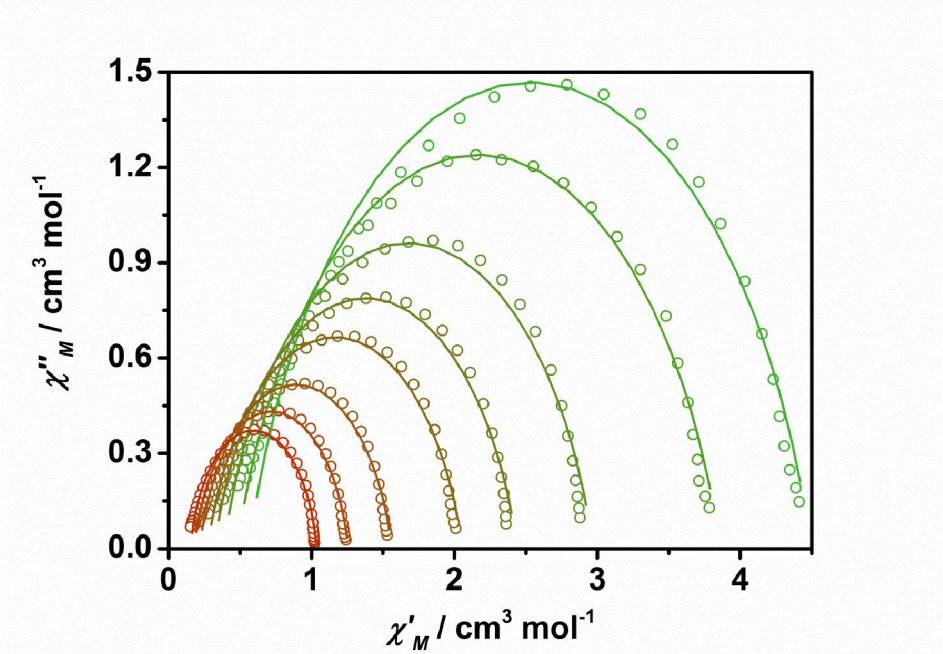

Fig. S15. Cole−Cole plots for the AC susceptibilities in zero DC field for **1** from 2.5-12 K. Solid lines represent fits (adjusted R^2 = 0.99861-0.99923) of the data in figs S13 and S14 using equations 1 and 2, which describe χ' and χ'' in terms of frequency, isothermal susceptibility (χ_T), adiabatic susceptibility (χ_S), relaxation time (τ), and a variable representing the distribution of relaxation times (α) (*43*).

$$\chi'(\nu_{ac}) = \chi_\infty + \frac{(\chi_s - \chi_\infty)[1 + (2\pi\nu_{ac}\tau)^{1-\alpha}\sin(\alpha\pi/2)]}{1 + 2(2\pi\nu_{ac}\tau)^{1-\alpha}\sin(\alpha\pi/2) + (2\pi\nu_{ac}\tau)^{2(1-\alpha)}}$$ Equation S1

$$\chi''(\nu_{ac}) = \frac{(\chi_s - \chi_\infty)(2\pi\nu_{ac}\tau)^{1-\alpha}\cos(\alpha\pi/2)}{1 + 2(2\pi\nu_{ac}\tau)^{1-\alpha}\sin(\alpha\pi/2) + (2\pi\nu_{ac}\tau)^{2(1-\alpha)}}$$ Equation S2

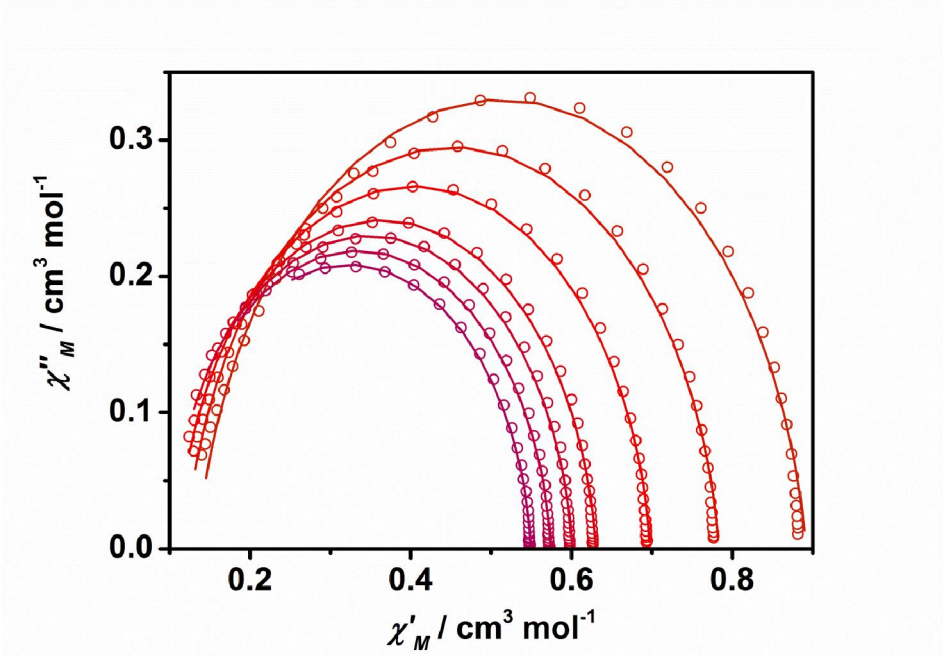

Fig. S16. Cole-Cole plots for the AC susceptibilities in zero DC field for **1** from 14-23 K. Solid lines represent fits (adjusted R^2 = 0.99948-0.99993) of the data in figs S13 and S14 using equations 1 and 2.

Table S5. Relaxation fitting parameters for **1** corresponding to figs S13 and S14 (adjusted R^2 = 0.99861-0.99993).

T / K	χ_T / cm^3 mol^{-1}	χ_S / cm^3 mol^{-1}	α	τ / s
2.5	4.49391(0.02022)	0.56172(0.01671)	0.18318(0.00708)	0.00487(6.94E-5)
3	3.85975(0.0185)	0.47843(0.01515)	0.19404(0.00745)	0.00495(7.56E-5)
4	2.97111(0.01432)	0.3842(0.01191)	0.18576(0.00763)	0.00481(7.42E-5)
5	2.43992(0.01154)	0.31918(0.00962)	0.1859(0.00751)	0.00478(7.25E-5)
6	2.0572(0.00928)	0.27241(0.00784)	0.18414(0.00723)	0.00466(6.77E-5)
8	1.56272(0.00668)	0.21582(0.00595)	0.16666(0.00715)	0.00418(5.83E-5)
10	1.25775(0.00465)	0.1802(0.00454)	0.13956(0.00659)	0.00345(4.23E-5)
12	1.03502(0.00318)	0.15365(0.00354)	0.10738(0.00594)	0.00259(2.73E-5)
14	0.89187(0.00216)	0.13468(0.00274)	0.08744(0.00502)	0.00194(1.68E-5)
16	0.78327(0.00146)	0.11999(0.00215)	0.07435(0.00418)	0.00142(1.00E-5)
18	0.69785(0.00102)	0.10838(0.00182)	0.06474(0.00359)	9.78557E-4(5.9E-6)
20	0.62998(7.760E-4)	0.09887(0.00192)	0.06082(0.00354)	5.61539E-4(3.4E-6)
21	0.60067(7.132E-4)	0.09606(0.0023)	0.05909(0.00389)	3.84293E-4(2.7E-6)
22	0.57423(6.035E-4)	0.09477(0.00282)	0.05795(0.00413)	2.4854E-4(2.1E-6)
23	0.54944(4.499E-4)	0.0957(0.00347)	0.05334(0.00414)	1.54379E-4(1.7E-6)

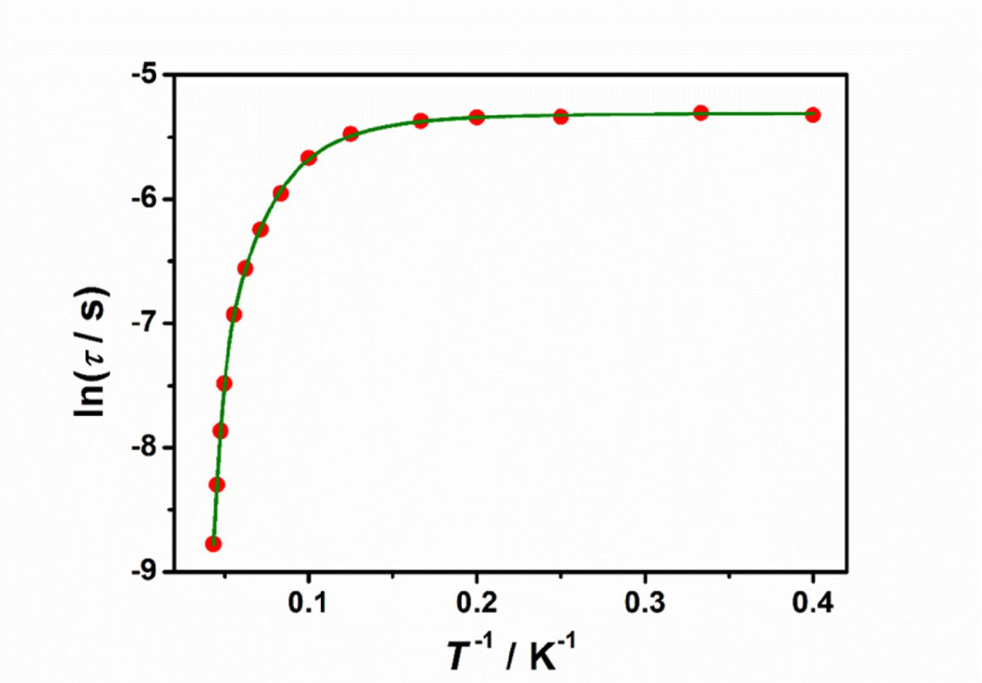

Fig. S17. Plot of natural log of the relaxation time *vs.* inverse temperature for **1**. The red points are from the AC susceptibility measurements. The solid green line is the best fit (adjusted $R^2 = 0.9873$) to equation $\tau^{-1} = \tau_0^{-1} e^{-U_{\mathrm{eff}}/k_{\mathrm{B}}T} + CT^n + \tau_{QTM}^{-1}$, giving: $U_{\mathrm{eff}} = 241(8)$ cm^{-1}, $\tau_0 = 6.4(3) \times 10^{-11}$ s, $C = 2.24(1) \times 10^{-2}$ s^{-1} K^{-n}, $n = 3.6(1)$ and $\tau_{\mathrm{QTM}} = 5.0(1) \times 10^{-3}$ s.

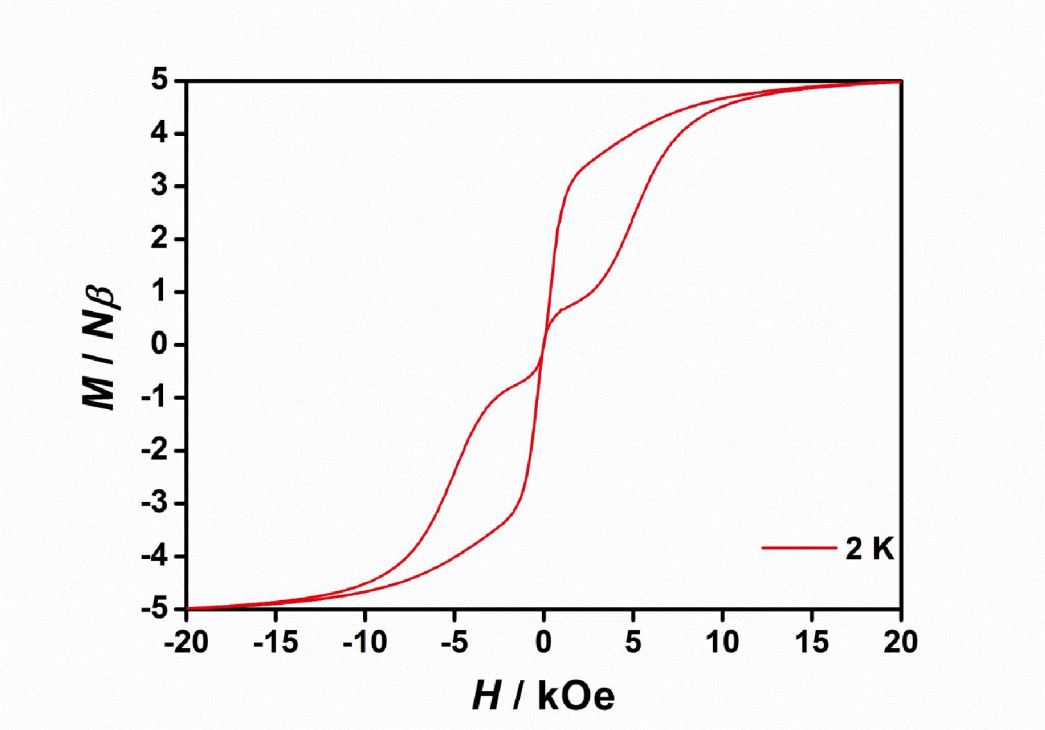

Fig. S18. Magnetic hysteresis loops for **1**. The data were collected continuously at 2 K using a field sweep speed of 200 Oe s^{-1}.

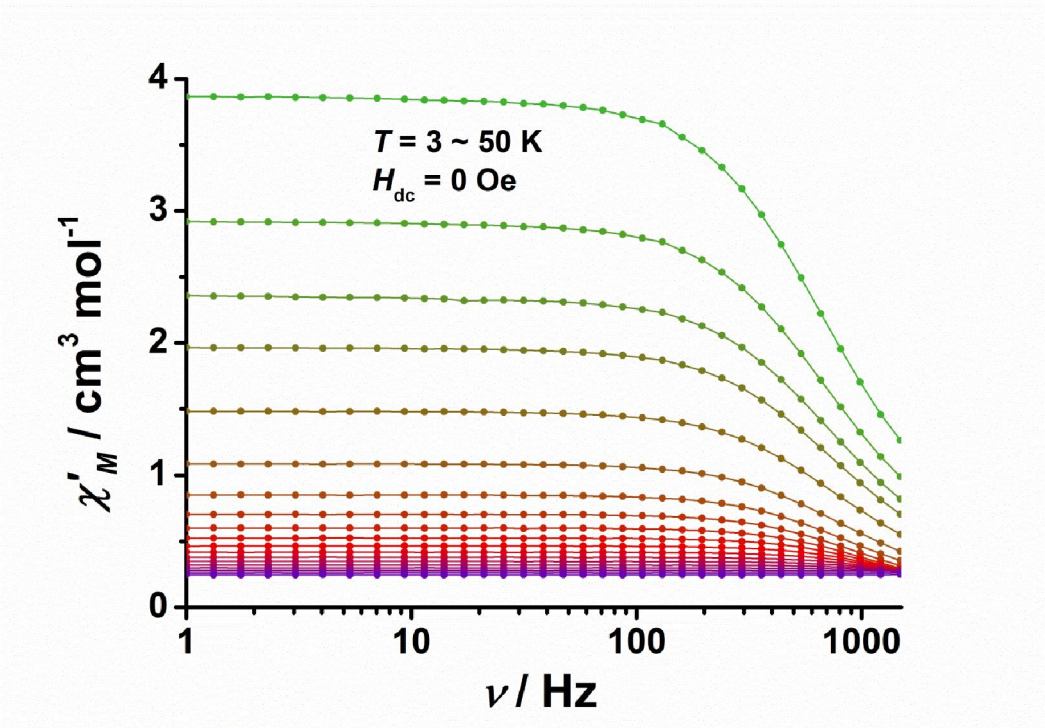

Fig. S19. Frequency dependence of the in-phase susceptibility (χ'_M) for **2** in zero DC field at AC frequencies of 1-1488 Hz from 3-50 K. Solid lines are a guide to the eye.

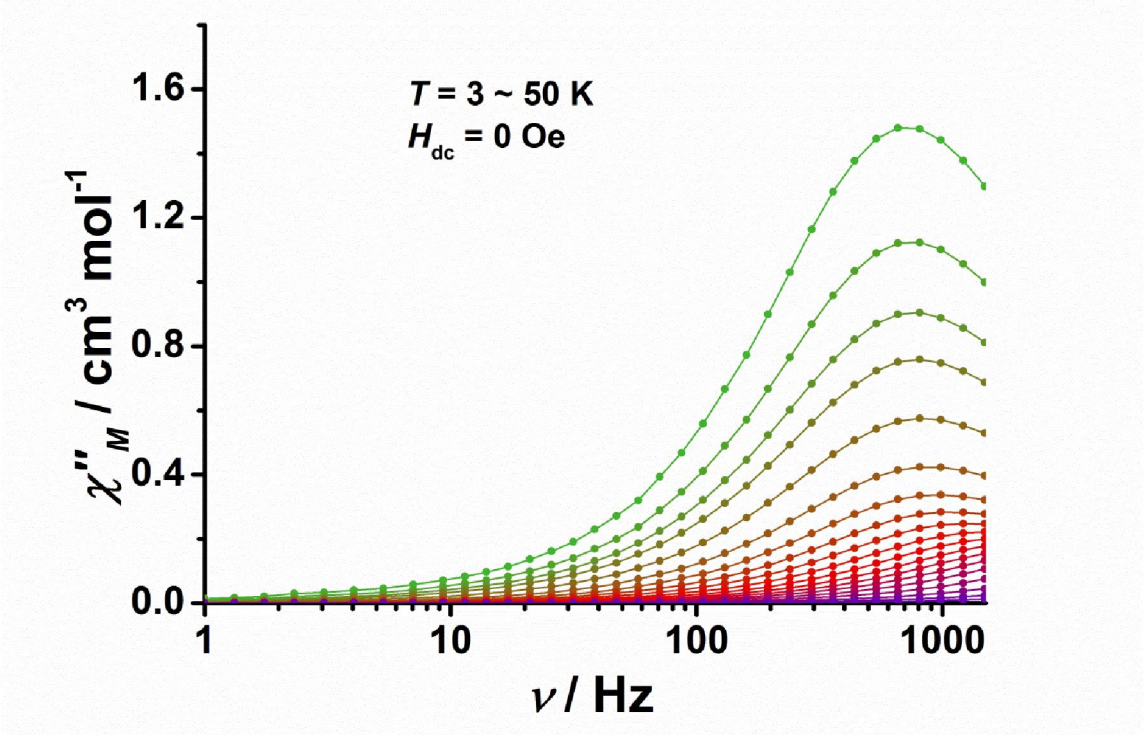

Fig. S20. Frequency dependence of the out-of-phase susceptibility (χ''_M) for **2** in zero DC field at AC frequencies of 1-1488 Hz from 3-50 K. Solid lines are a guide to the eye.

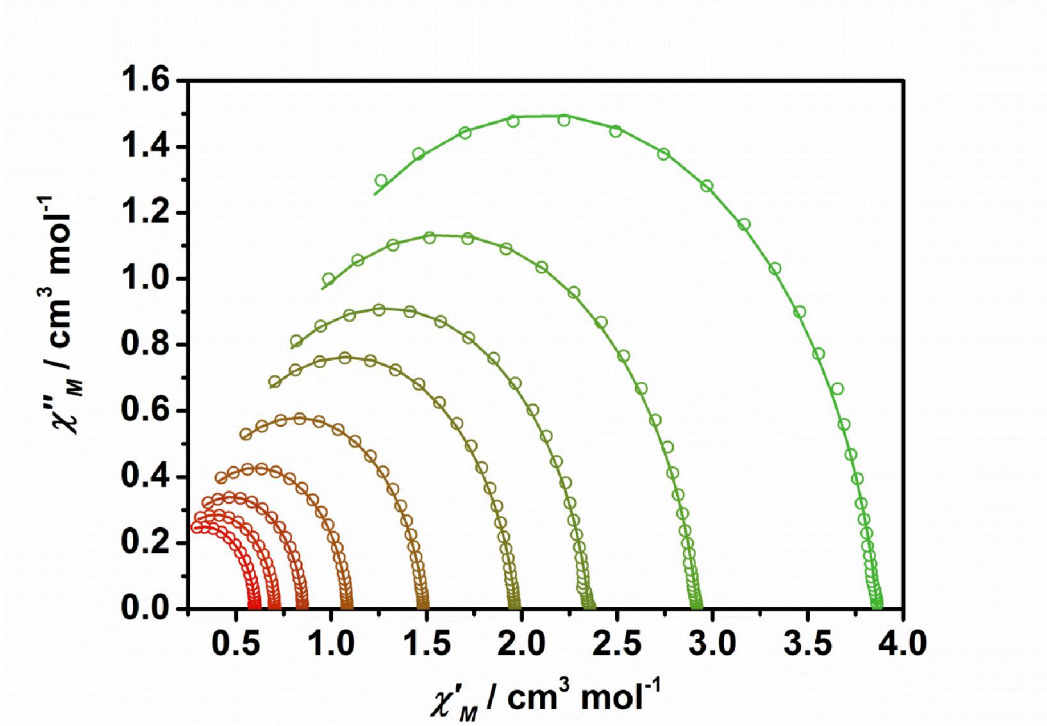

Fig. S21. Cole−Cole plots for the AC susceptibilities in zero DC field for **1** from 3-20 K. Solid lines represent fits (adjusted R^2 = 0.9993-0.99995) to the data in figs S19 and S20 using equations 1 and 2, which describe χ' and χ'' in terms of frequency, isothermal susceptibility (χ_T), adiabatic susceptibility (χ_S), relaxation time (τ), and a variable representing the distribution of relaxation times (α) (*42*).

Table S6. Relaxation fitting parameters for **2** corresponding to figs S19 and S20 (adjusted R^2 = 0.99993-0.99995).

T / K	χ_T / cm^3 mol^{-1}	χ_S / cm^3 mol^{-1}	α	τ / s
3	3.86324(0.00289)	0.37725(0.01579)	0.09626(0.00291)	2.20617E-4(1.55E-6)
4	2.9183(0.00227)	0.27551(0.01293)	0.09689(0.00307)	2.11651E-4(1.60E-6)
5	2.34983(0.00183)	0.22701(0.01079)	0.09658(0.00314)	2.04507E-4(1.61E-6)
6	1.96622(0.00139)	0.19339(0.00848)	0.09481(0.00291)	1.98125E-4(1.46E-6)
8	1.48638(0.00706)	0.1535(0.00111)	0.08907(0.00315)	1.90219E-4(1.53E-6)
11	1.08793(8.94E-4)	0.11988(0.00592)	0.07876(0.00357)	1.80442E-4(1.64E-6)
14	0.85288(6.98E-4)	0.09814(0.005)	0.0671(0.00372)	1.66551E-4(1.60E-6)
17	0.70546(5.11E-4)	0.08254(0.00409)	0.05466(0.00349)	1.49936E-4(1.39E-6)
20	0.60135(3.85E-4)	0.06778(0.00362)	0.04384(0.00332)	1.3084E-4(1.22E-6)

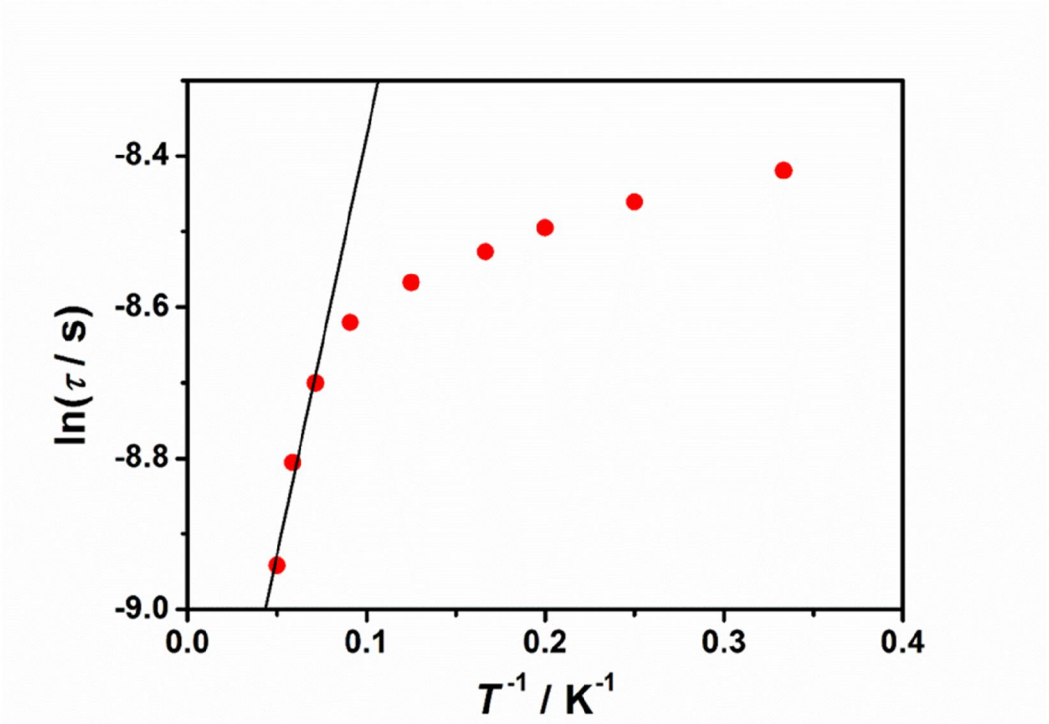

Fig. S22. Plot of natural log of the relaxation time *vs.* inverse temperature for **2**. The solid black line is the best linear Arrhenius fit (three data points at higher temperatures, adjusted $R^2 = 0.9388$) to $\tau = \tau_0 \exp(U_{eff}/k_B T)$, giving $U_{eff} \approx 7(1)$ cm^{-1} and $\tau_0 = 7.6\ (5) \times 10^{-5}$.

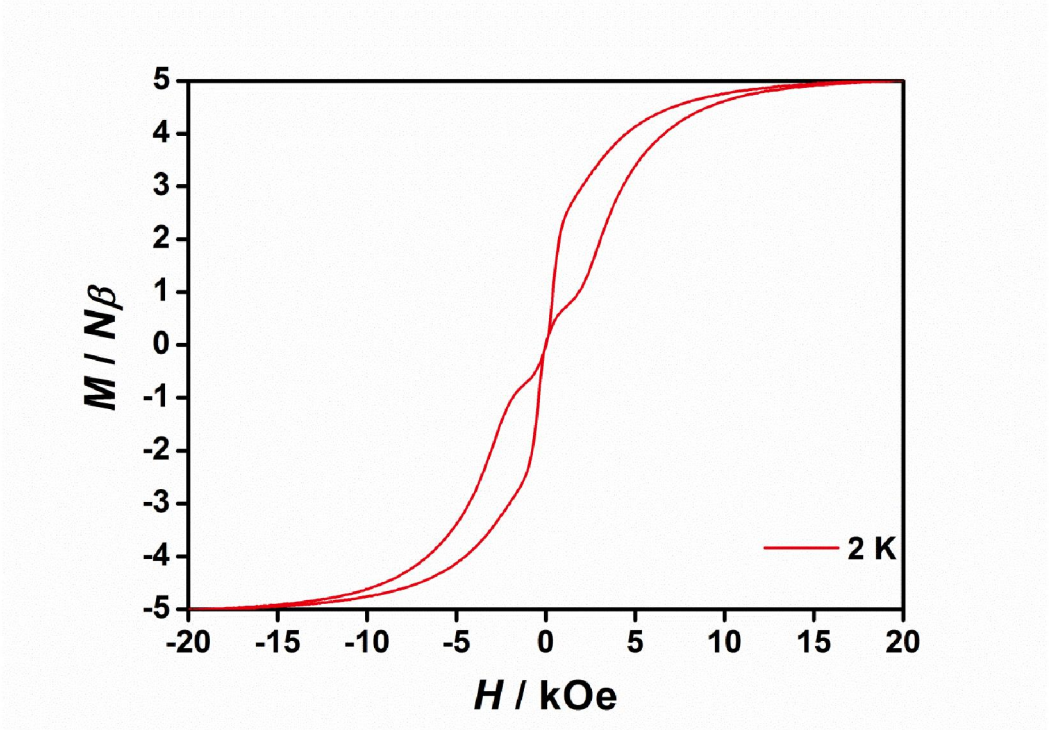

Fig. S23. Magnetic hysteresis loops for **2**. The data were continuously collected at 2 K under a field sweep speed of 200 Oe s^{-1}.

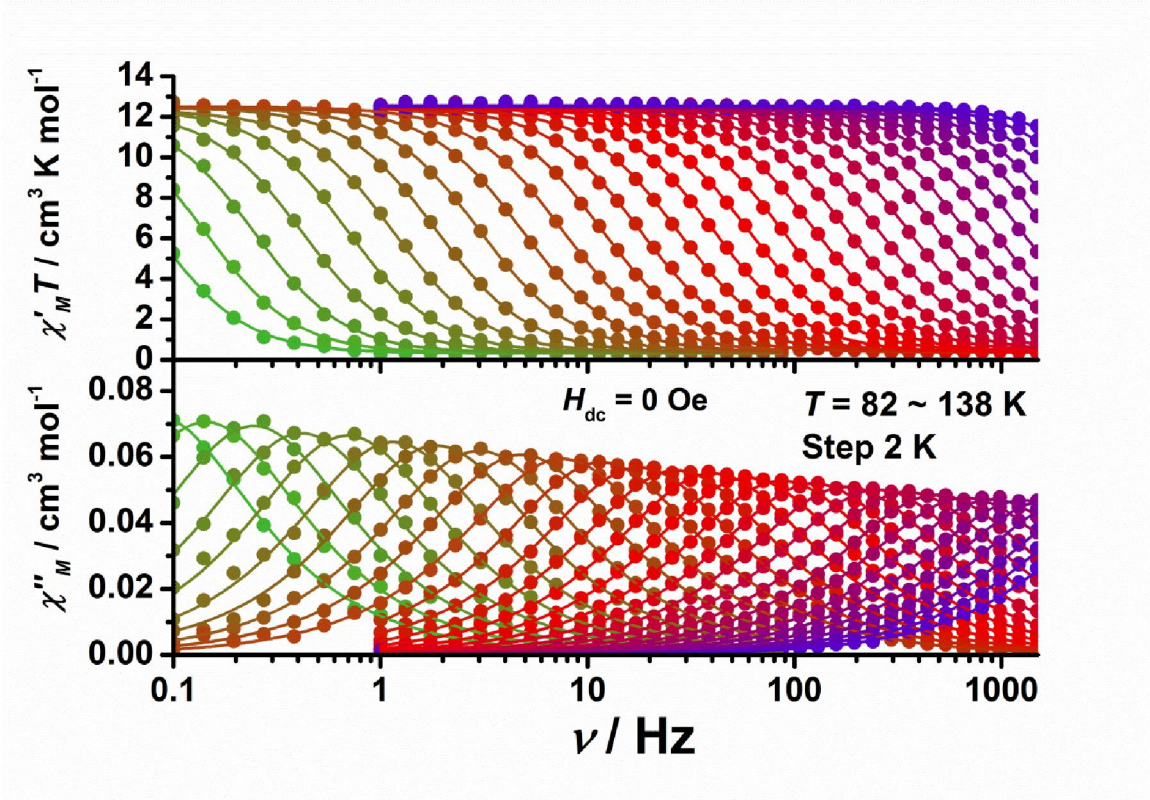

Fig. S24. Frequency dependence of the in-phase $\chi'_M T$ product and the out-of-phase susceptibility χ''_M for **3**, collected under zero D.C. field at ac frequencies of ν = 0.1-1488 Hz from 82-138 K. Solid lines represent fits to the data using equation S1 and S2 (adjusted R^2 = 0.99823-0.99988).

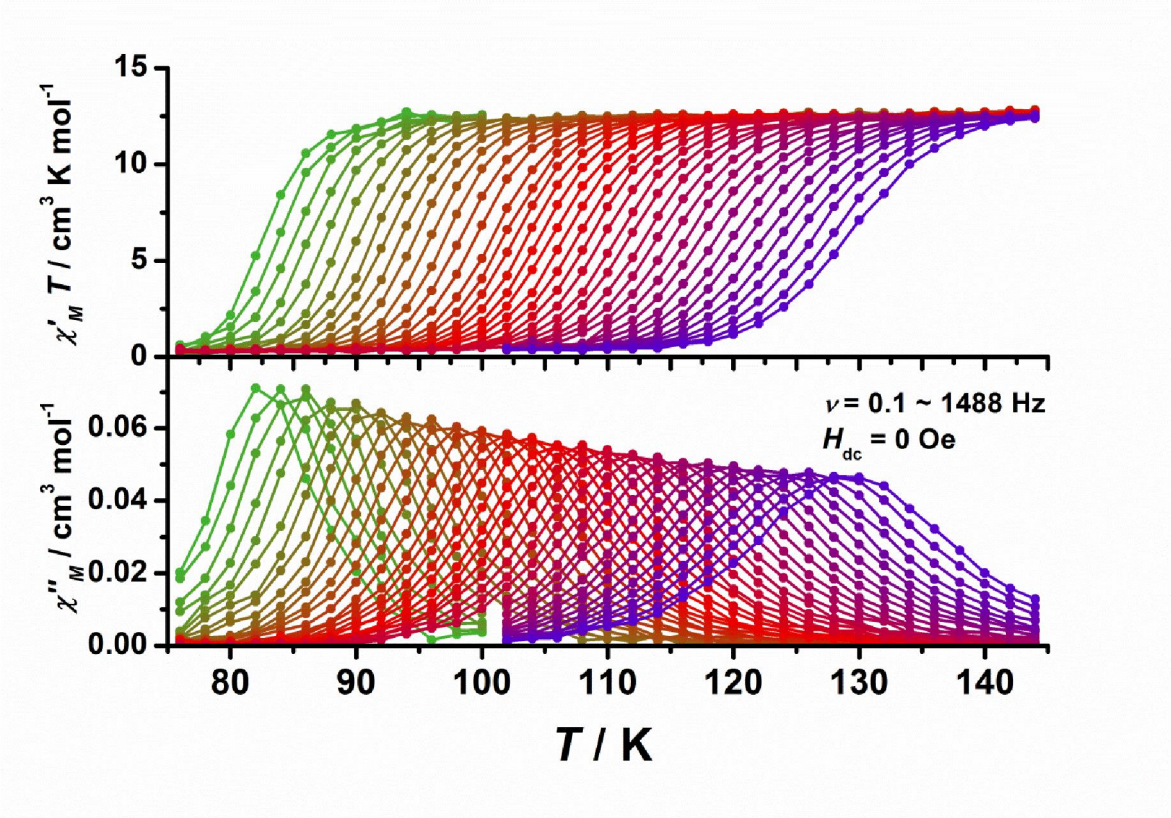

Fig. S25. Temperature dependence of the in-phase $\chi'_M T$ product and the out-of-phase susceptibility χ''_M for **3**, collected under zero D.C. field at ac frequencies of ν = 0.1-1488 Hz from 76-144 K. Solid lines are a guide to the eye.

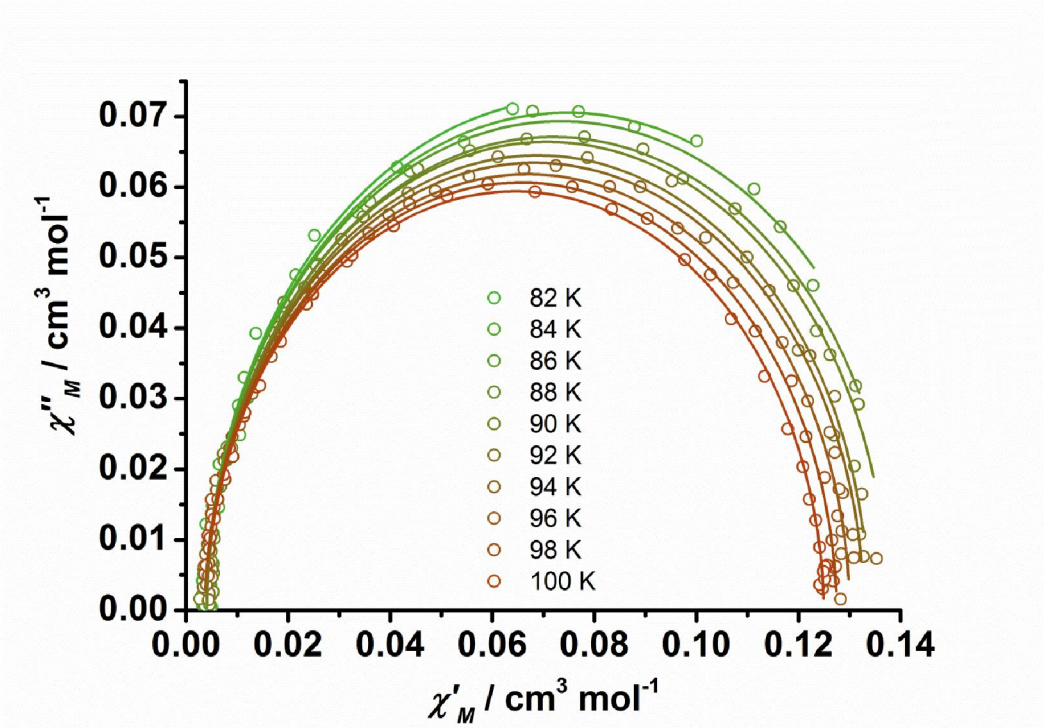

Fig. S26. Cole-Cole plots for the AC susceptibilities in zero DC field for **3** from 82-100 K. Solid lines represent fits to the data in fig. S24 using equations 1 and 2 (adjusted R^2 = 0.99823-0.99970).

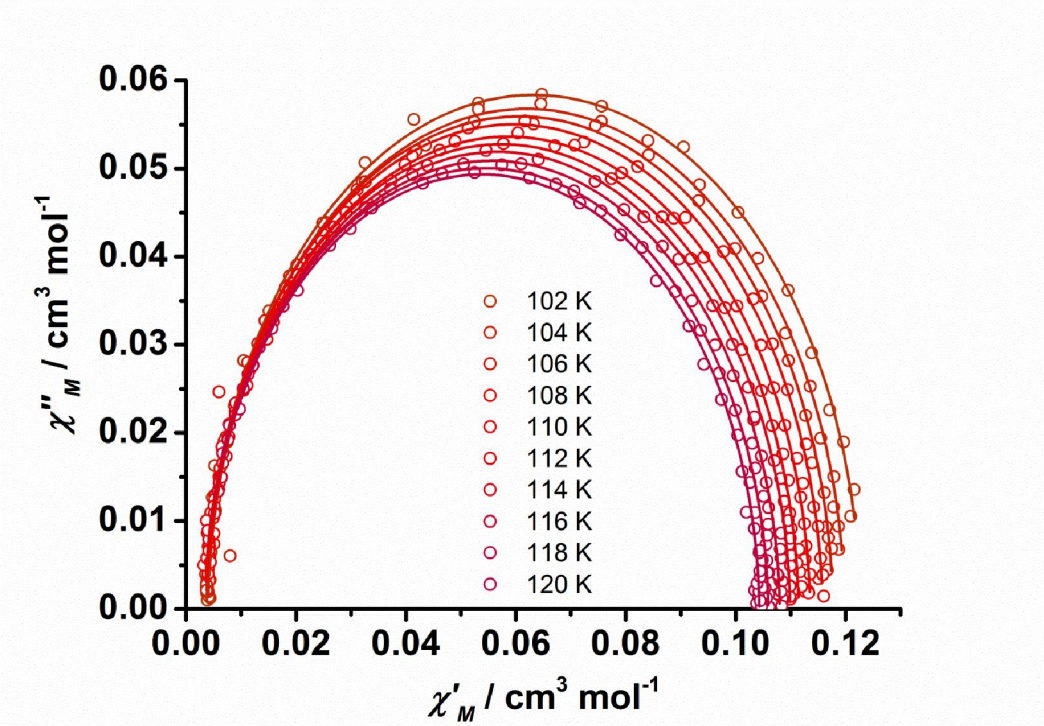

Fig. S27. Cole-Cole plots for the AC susceptibilities in zero DC field for **3** from 102-120 K. Solid lines represent fits to the data in fig. S24 using equations 1 and 2 (adjusted R^2 = 0.99964-0.99988).

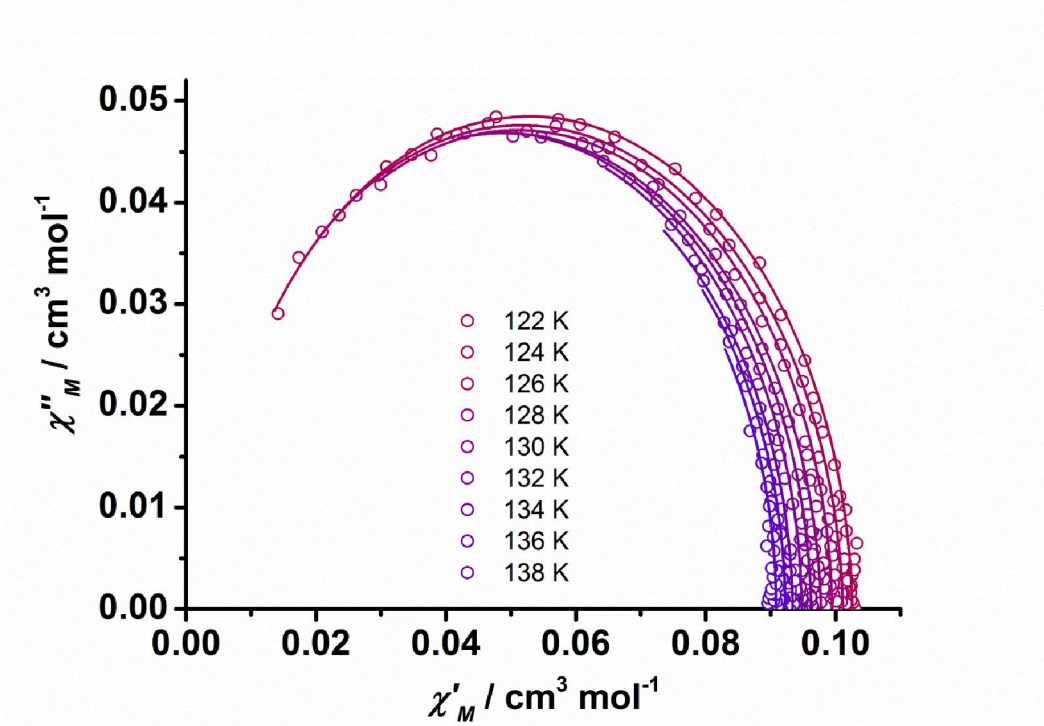

Fig. S28. Cole-Cole plots for the AC susceptibilities in zero DC field for **3** from 122-138 K. Solid lines represent fits to the data in fig. S24 using equations 1 and 2 (adjusted R^2 = 0.99977-0.99986).

Table S7. Relaxation fitting parameters for **3** corresponding to fig. S24 using equations 1 and 2 (adjusted R^2 = 0.99823-0.99988).

T / K	χ_T / cm^3 mol^{-1}	χ_S / cm^3 mol^{-1}	α	τ / s
82	0.14931(0.0015)	0.00407(1.51E-4)	0 [a]	1.93903(0.02372)
84	0.14522(8.51E-4)	0.00409(1.65E-4)	0 [a]	1.11075(0.00924)
86	0.14279(7.79E-4)	0.00406(2.33E-4)	0 [a]	0.64982(0.00593)
88	0.1396(6.34E-4)	0.00409(2.02E-4)	0.00589(0.00427)	0.38196(0.00273)
90	0.13751(6.57E-4)	0.0041(2.84E-4)	0.0027(0.00524)	0.22939(0.00193)
92	0.13368(4.57E-4)	0.00401(2.53E-4)	0.00319(0.00424)	0.13787(9.23E-4)
94	0.13284(4.08E-4)	0.00364(2.79E-4)	0.01134(0.00422)	0.08565(5.71E-4)
96	0.13008(2.89E-4)	0.00378(2.43E-4)	0.01336(0.00337)	0.0531(2.81E-4)
98	0.12747(2.89E-4)	0.0037(3.01E-4)	0.01277(0.00378)	0.0331(1.93E-4)
100	0.12496(2.75E-4)	0.00383(3.57E-4)	0.01234(0.00405)	0.02112(1.29E-4)
102	0.12268(2.41E-4)	0.00374(1.29E-4)	0.01179(0.00237)	0.01361(5.2E-5)
104	0.11981(2.84E-4)	0.004(1.84E-4)	0.01223(0.00314)	0.00893(4.4E-5)
106	0.11765(1.51E-4)	0.00366(1.16E-4)	0.01178(0.00184)	0.00589(1.7E-5)
108	0.11578(2.33E-4)	0.00338(2.13E-4)	0.01342(0.00315)	0.00394(1.9E-5)
110	0.11353(1.46E-4)	0.00362(1.57E-4)	0.01535(0.00218)	0.00267(9E-6)
112	0.11143(1.31E-4)	0.00336(1.67E-4)	0.01497(0.00216)	0.00183(6E-6)
114	0.10988(1.79E-4)	0.00357(2.69E-4)	0.01494(0.00324)	0.00128(6E-6)
116	0.10802(1.45E-4)	0.00337(2.63E-4)	0.01744(0.00292)	8.91887E-4(4E-6)
118	0.10593(1.21E-4)	0.00299(2.69E-4)	0.01764(0.00272)	6.27543E-4(3E-6)
120	0.1043(1.39E-4)	0.00341(3.79E-4)	0.0139(0.0035)	4.53559E-4(3E-6)
122	0.10253(1.18E-4)	0.00311(4.14E-4)	0.01597(0.00341)	3.26751E-4(2E-6)
124	0.10112(1.38E-4)	0.00207(6.51E-4)	0.02504(0.00459)	2.36554E-4(2E-6)
126	0.09944(1.19E-4)	0.00276(7.63E-4)	0.01631(0.00472)	1.75965E-4(2E-6)
128	0.09775(1.29E-4)	0 [§]	0.02697(0.00348)	1.24907E-4(7E-7)
130	0.09623(1.18E-4)	0 [§]	0.01727(0.00376)	9.36102E-5(6E-7)
132	0.09478(1.15E-4)	0 [§]	0.01038(0.00441)	7.22468E-5(5E-7)
134	0.09338(1.33E-4)	0 [§]	0.01333(0.00641)	5.41842E-5(6E-7)
136	0.09225(1.22E-4)	0 [§]	0.00674(0.00732)	4.2074E-5(6E-7)
138	0.09038(9E-5)	0 [§]	0 [§]	3.29312E-5(4E-7)

[§] These parameter values were restricted to non-negative.

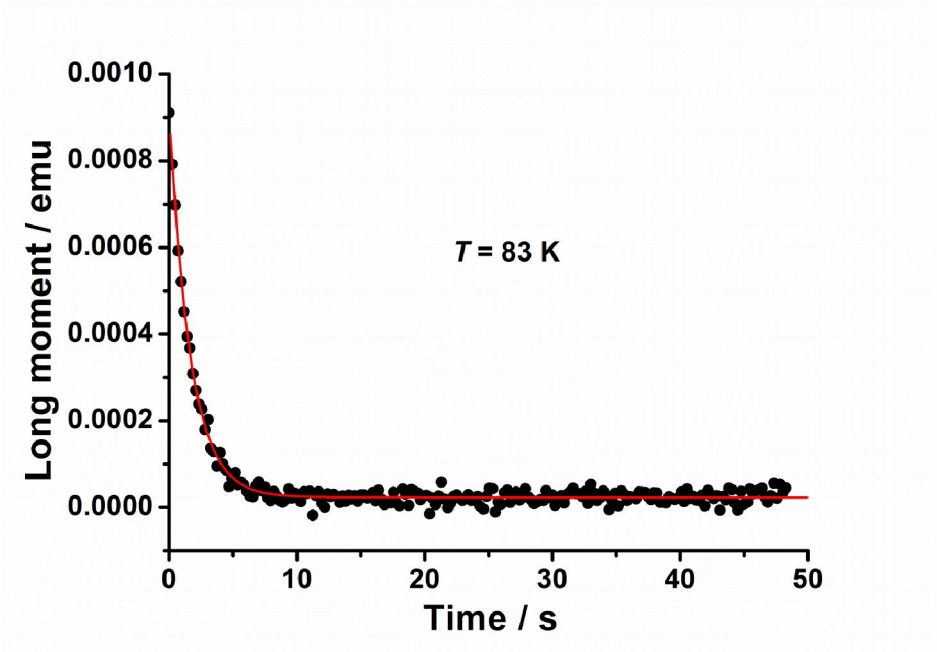

Fig. S29. Plot of magnetization decay *vs.* time used to derive D.C. relaxation times for **3** at 83 K. The solid line is the best fit (adjusted $R^2 = 0.98704$) to the exponential decay as $M(t) = M_f + (M_0 - M_f) \exp[(-(t/\tau)^{\beta}]$, where M_0 is the initial magnetization, M_f is the final magnetization, τ is the relaxation time, and β is a generalized coefficient, which should be equal to 1 for an ideal exponential decay (*44*).

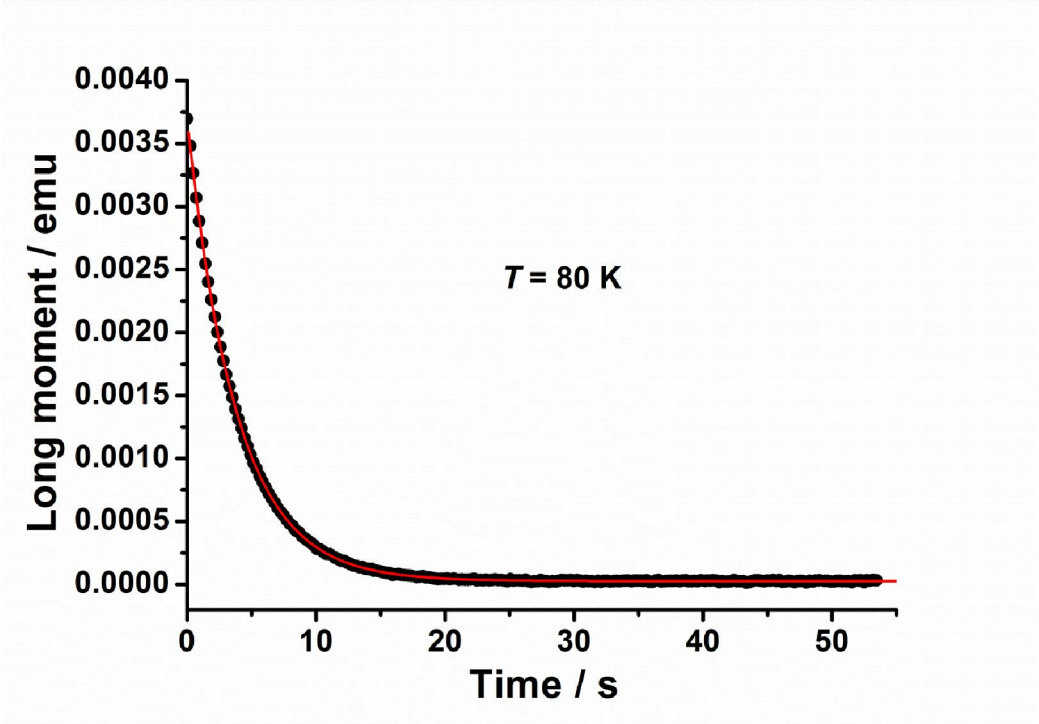

Fig. S30. Plot of magnetization decay *vs.* time used to derive relaxation times for **3** at 80 K. The solid line is the best fit (adjusted $R^2 = 0.99995$).

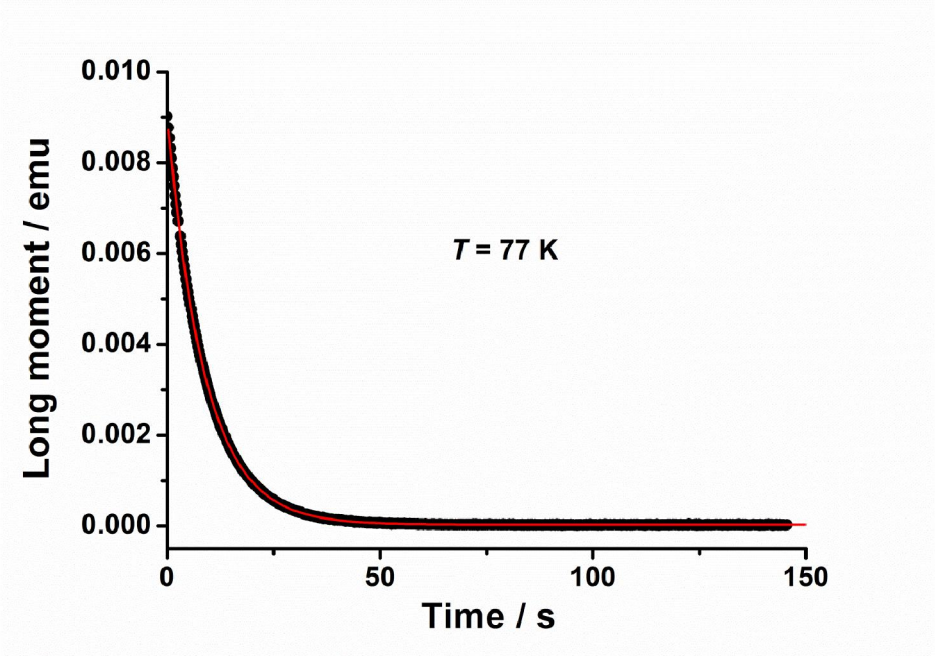

Fig. S31. Plot of magnetization decay *vs.* time used to derive relaxation times for **3** at 77 K. The solid line is the best fit (adjusted $R^2 = 0.99999$)

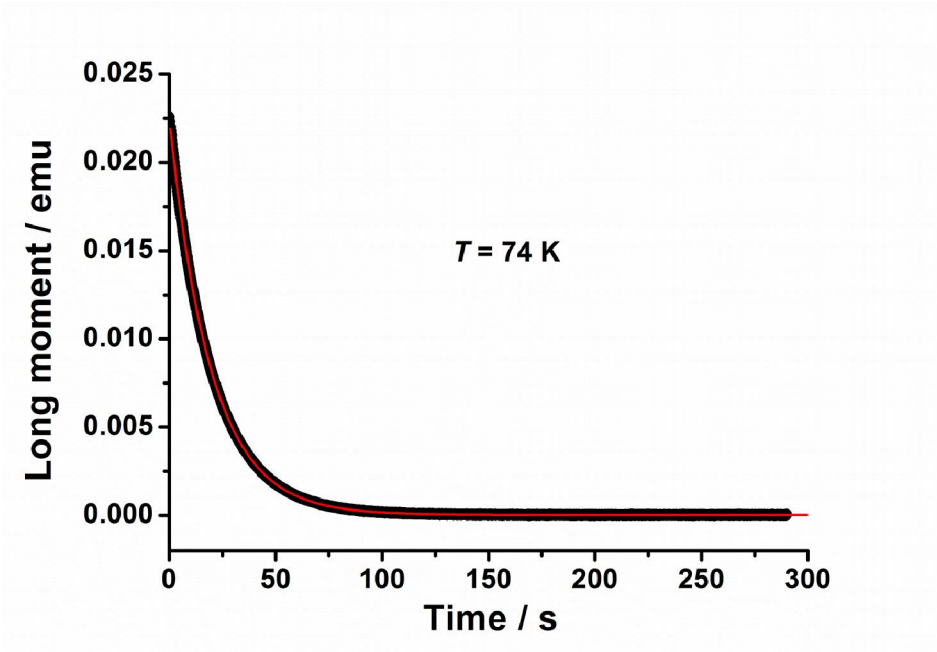

Fig. S32. Plot of magnetization decay *vs.* time used to derive relaxation times for **3** at 74 K. The solid line is the best fit (adjusted R^2 = 0.99999).

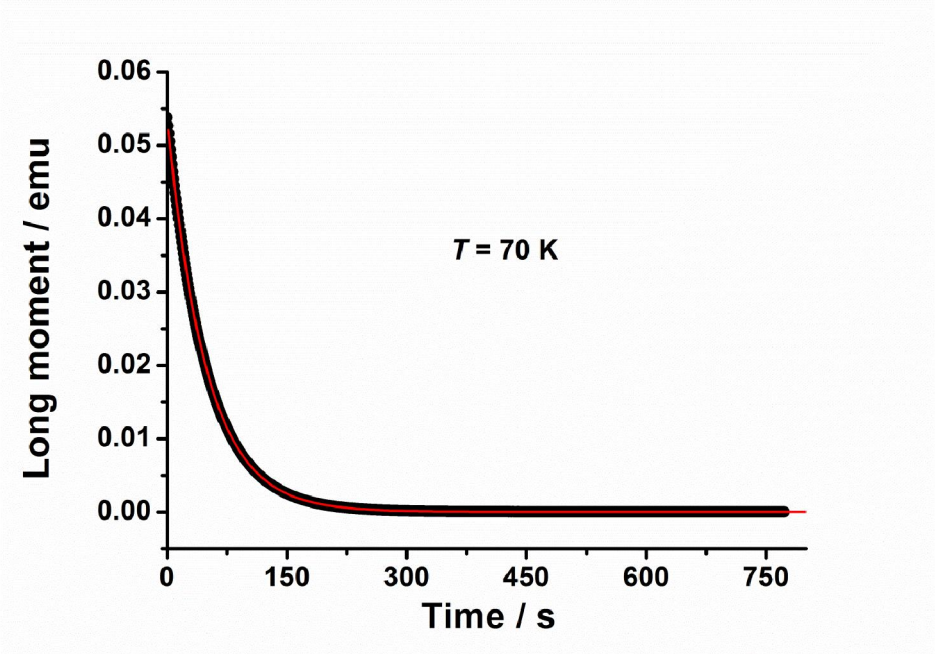

Fig. S33. Plot of magnetization decay *vs.* time used to derive relaxation times for **3** at 70 K. The solid line is the best fit (adjusted R^2 = 0.99999).

5

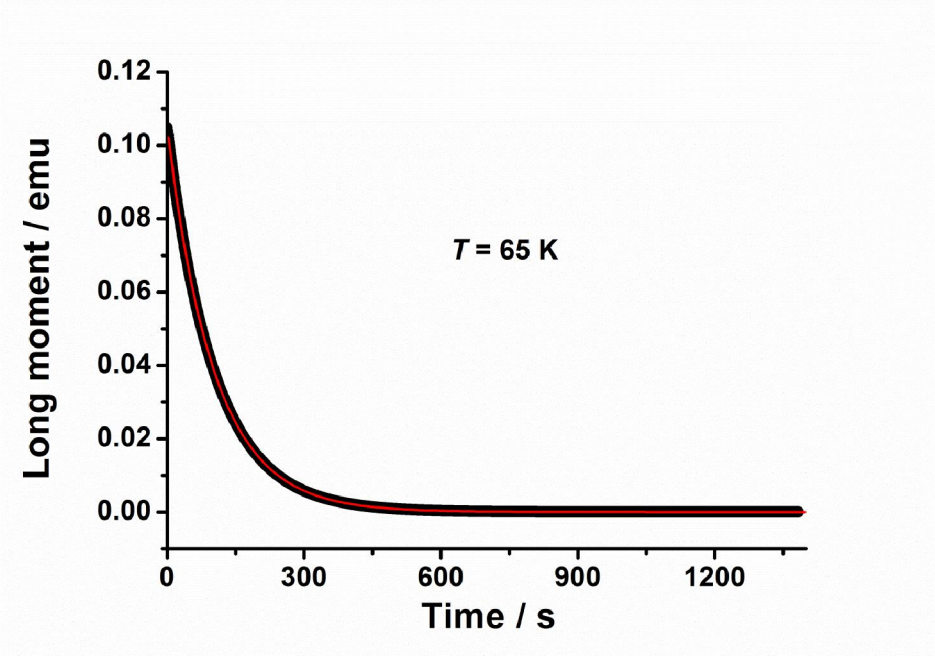

Fig. S34. Plot of magnetization decay *vs.* time used to derive relaxation times for **3** at 65 K. The solid line is the best fit (adjusted R^2 = 0.99999).

5

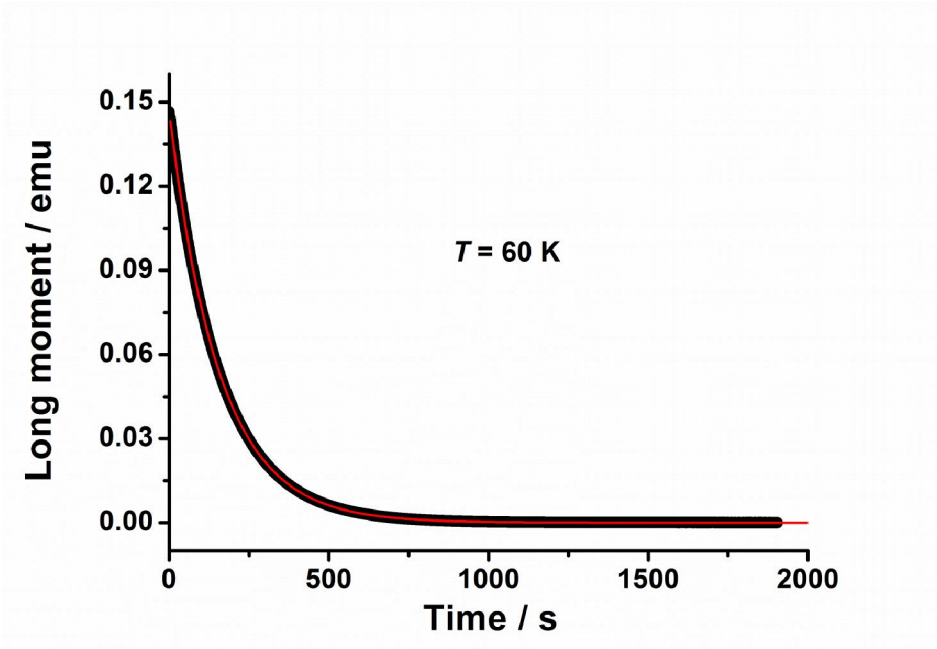

Fig. S35. Plot of magnetization decay *vs.* time used to derive relaxation times for **3** at 60 K. The solid line is the best fit (adjusted R^2 = 0.99999).

5

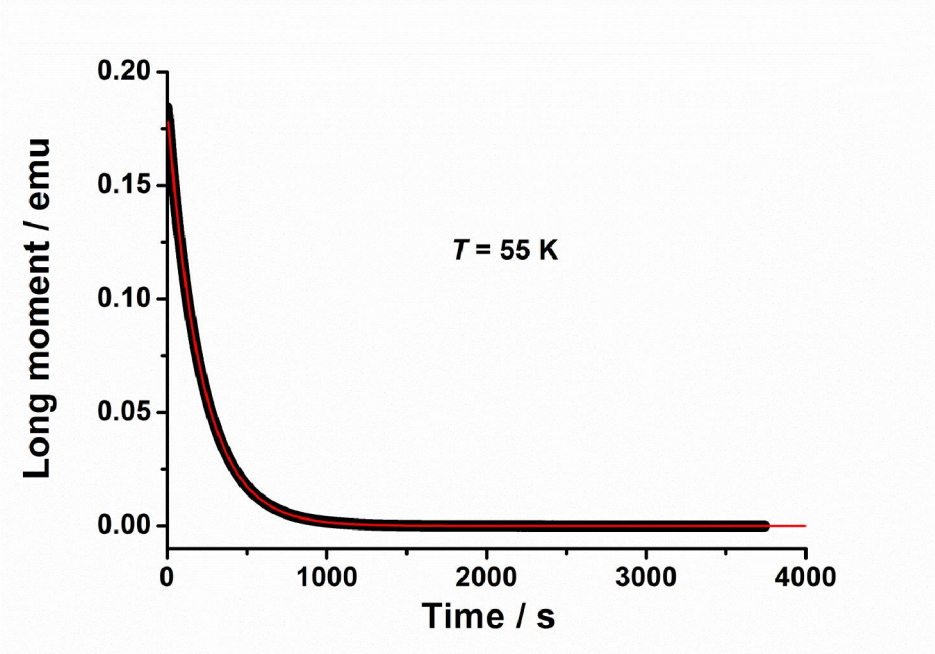

Fig. S36. Plot of magnetization decay *vs.* time used to derive relaxation times for **3** at 55 K. The solid line is the best fit (adjusted R^2 = 0.99999).

5

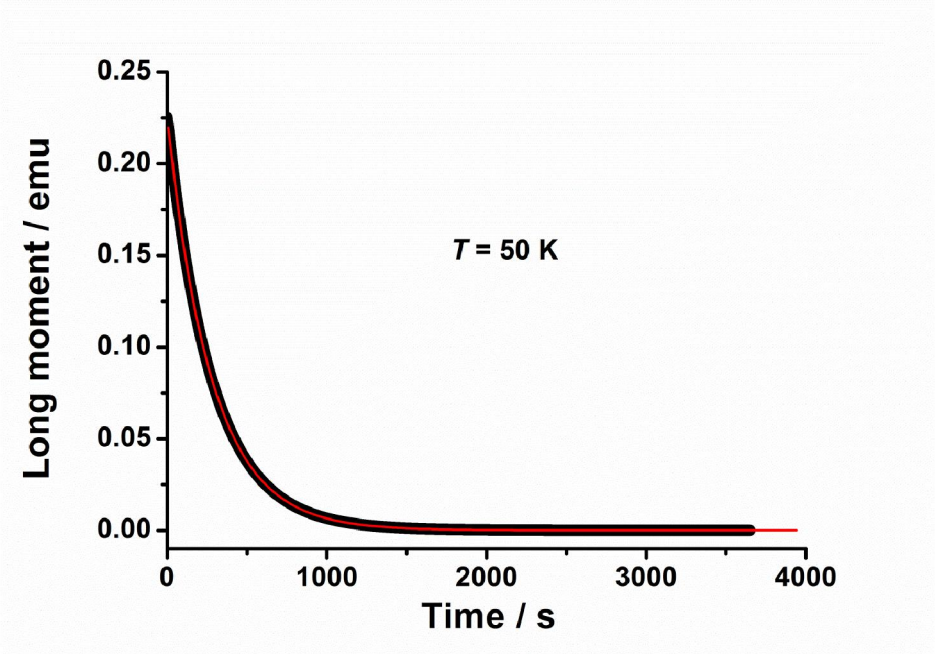

Fig. S37. Plot of magnetization decay *vs.* time used to derive relaxation times for **3** at 50 K. The solid line is the best fit (adjusted R^2 = 0.99999).

5

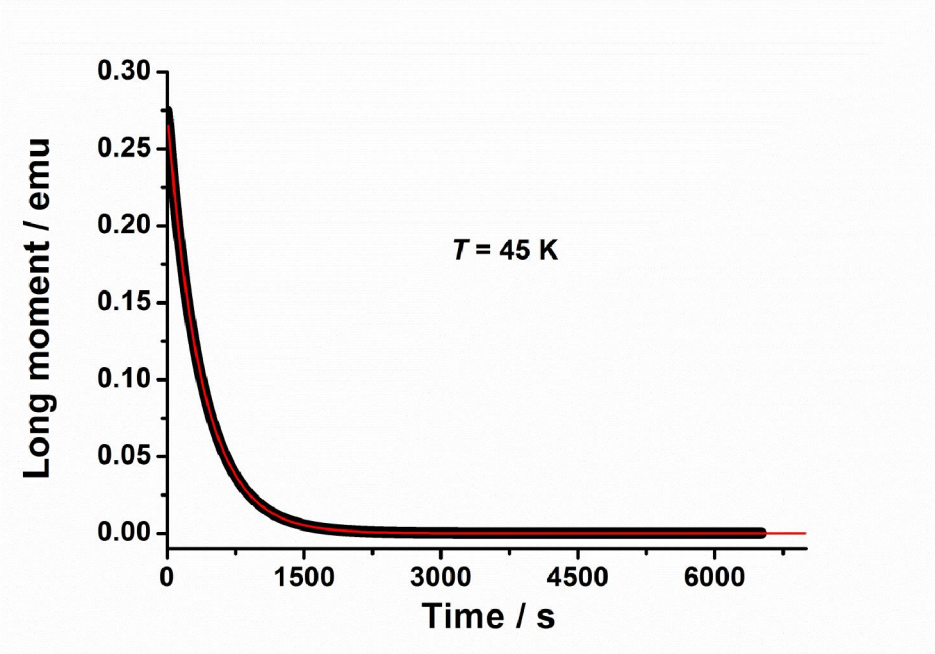

Fig. S38. Plot of magnetization decay *vs.* time used to derive relaxation times for **3** at 45 K. The solid line is the best fit (adjusted R^2 = 0.99999).

5

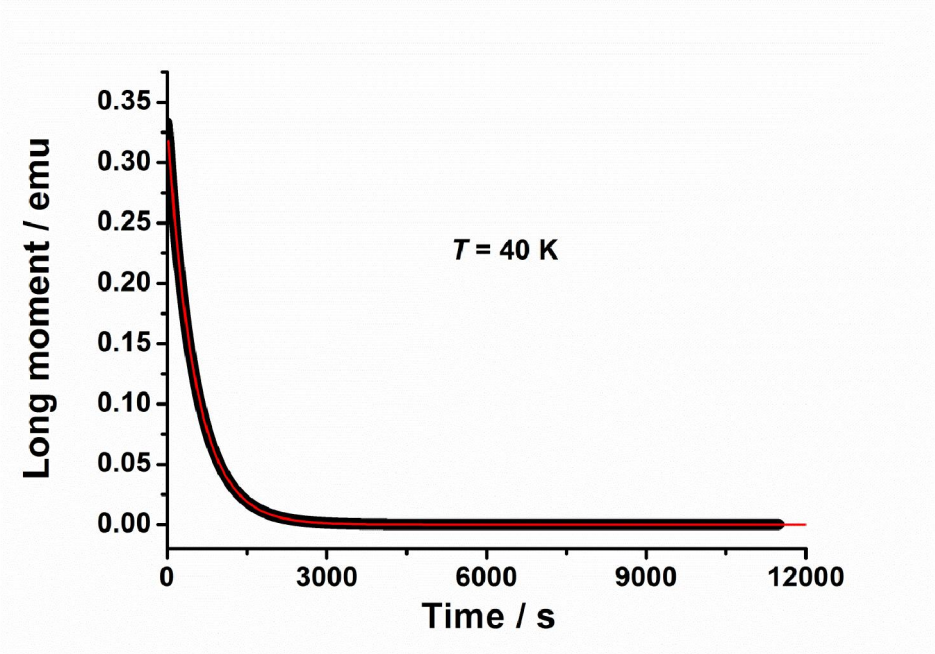

Fig. S39. Plot of magnetization decay *vs.* time used to derive relaxation times for **3** at 40 K. The solid line is the best fit (adjusted R^2 = 0.99999).

5

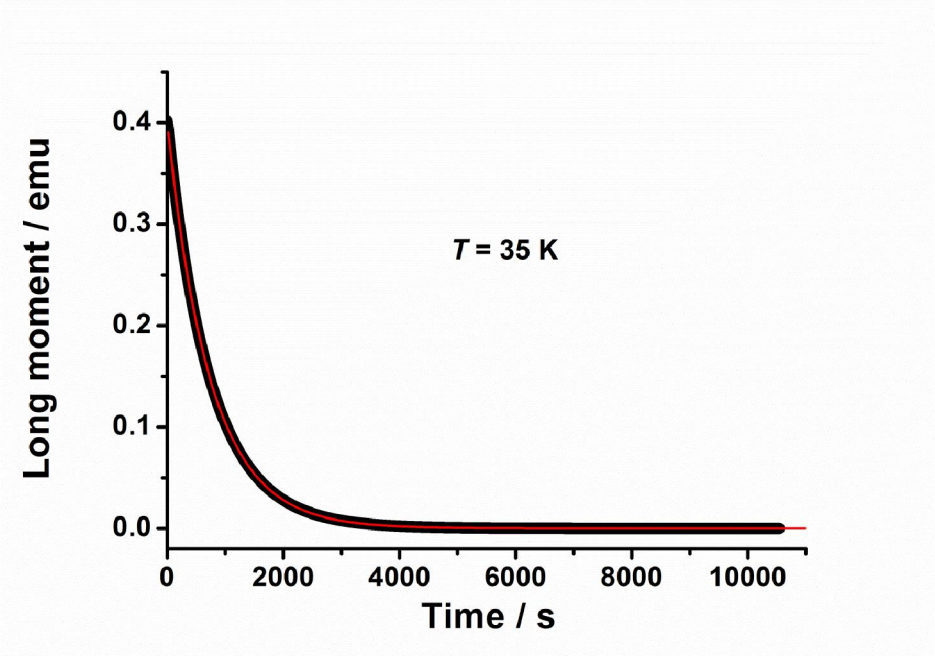

Fig. S40. Plot of magnetization decay *vs.* time used to derive relaxation times for **3** at 35 K. The solid line is the best fit (adjusted R^2 = 0.99999).

5

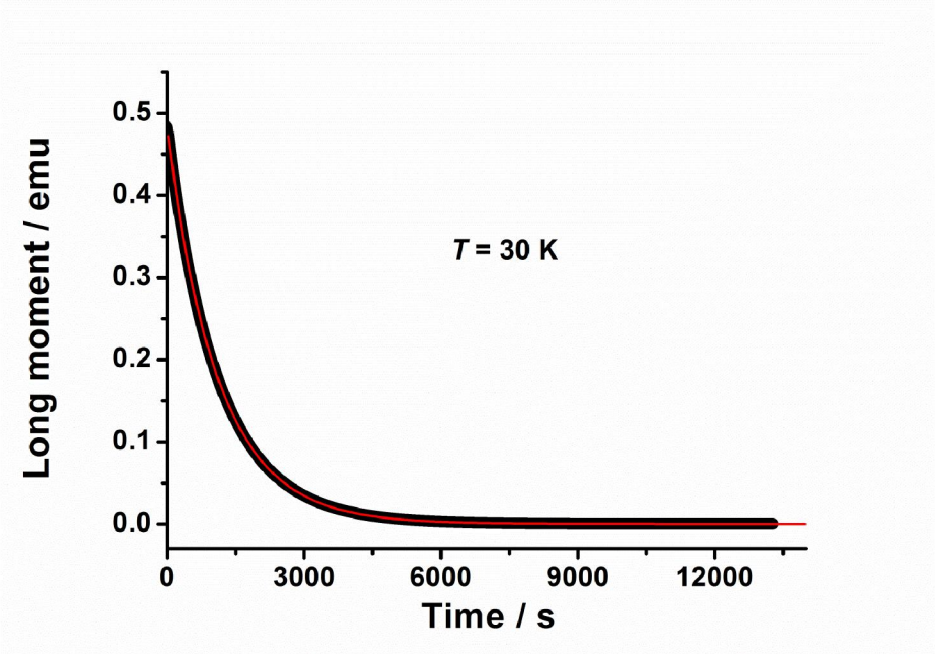

Fig. S41. Plot of magnetization decay *vs.* time used to derive relaxation times for **3** at 30 K. The solid line is the best fit (adjusted R^2 = 0.99999).

5

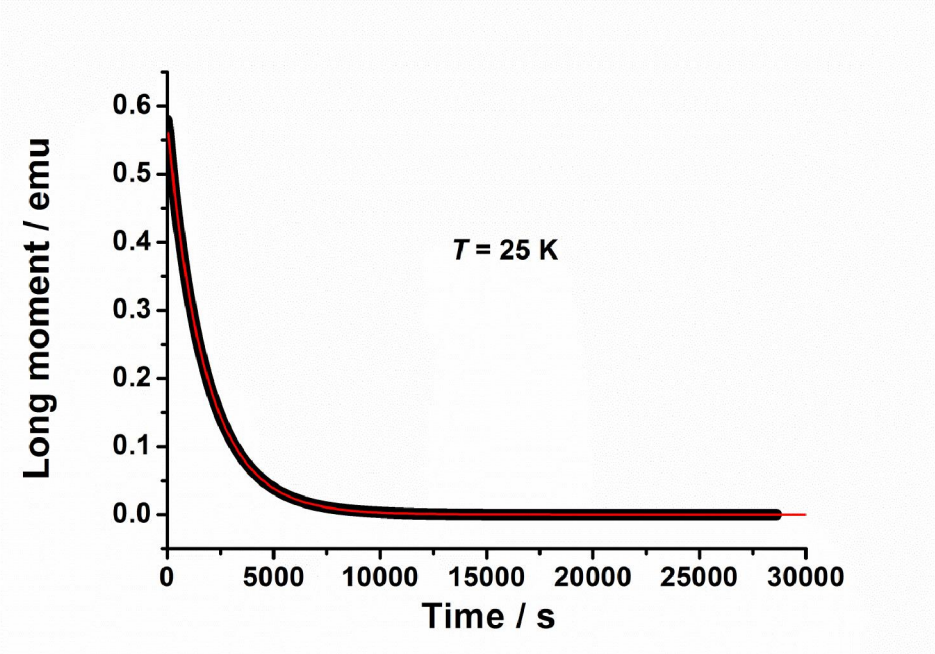

Fig. S42. Plot of magnetization decay *vs.* time used to derive relaxation times for **3** at 25 K. The solid line is the best fit (adjusted R^2 = 0.99999).

5

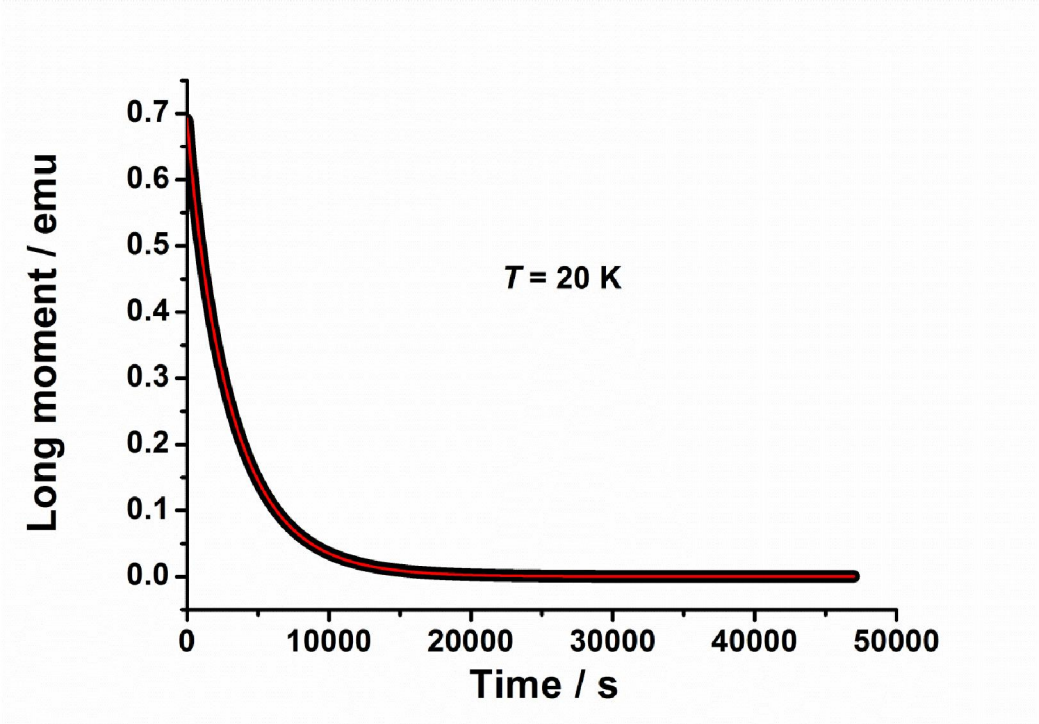

Fig. S43. Plot of magnetization decay *vs.* time used to derive relaxation times for **3** at 20 K. The solid line is the best fit (adjusted $R^2 = 0.99999$).

5

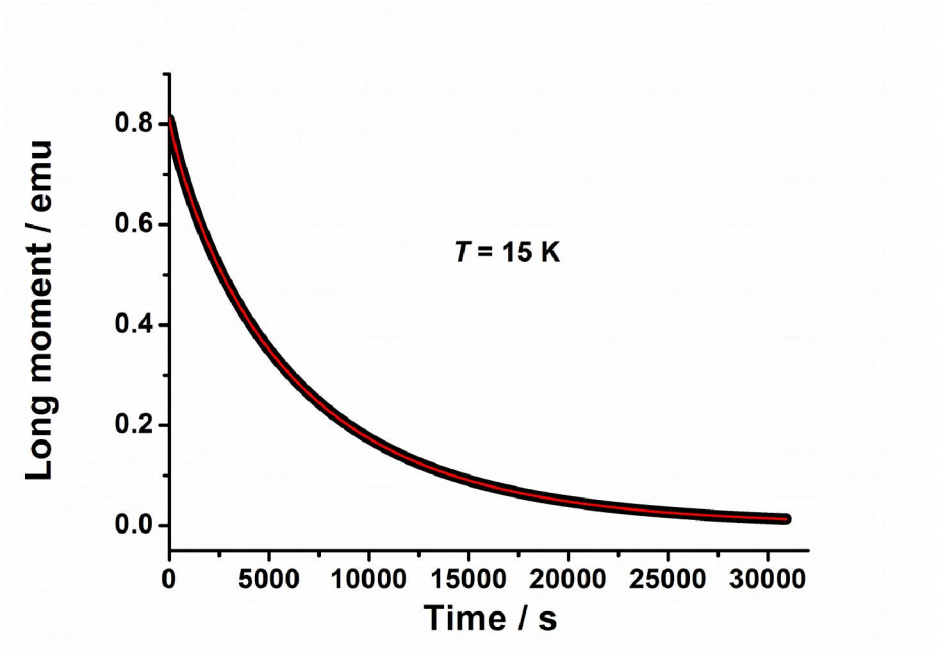

Fig. S44. Plot of magnetization decay *vs.* time used to derive relaxation times for **3** at 15 K. The solid line is the best fit (adjusted R^2 = 0.99999).

5

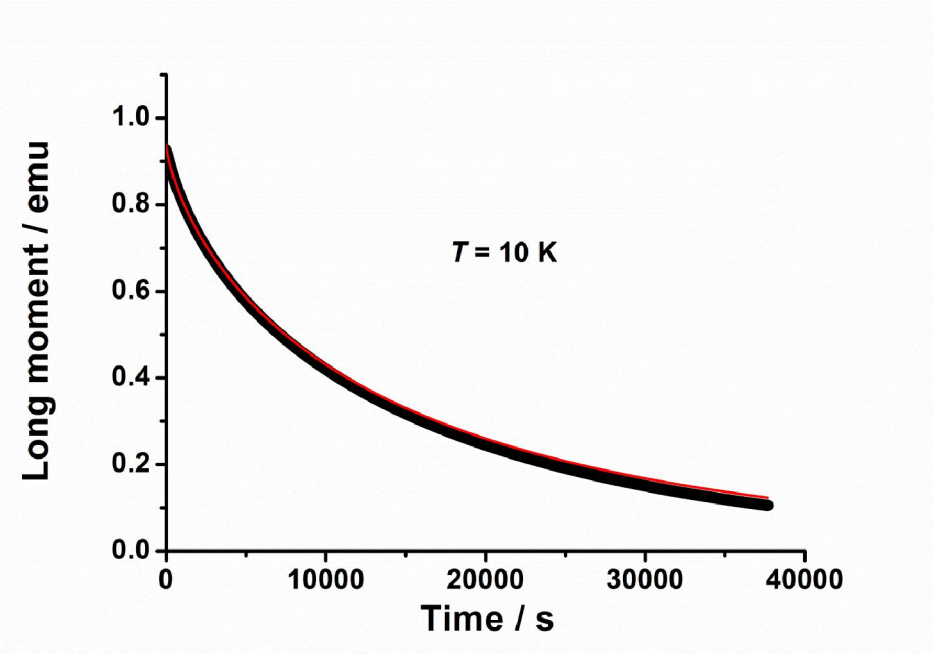

Fig. S45. Plot of magnetization decay *vs.* time used to derive relaxation times for **3** at 10 K. The solid line is the best fit (adjusted $R^2 = 0.99496$).

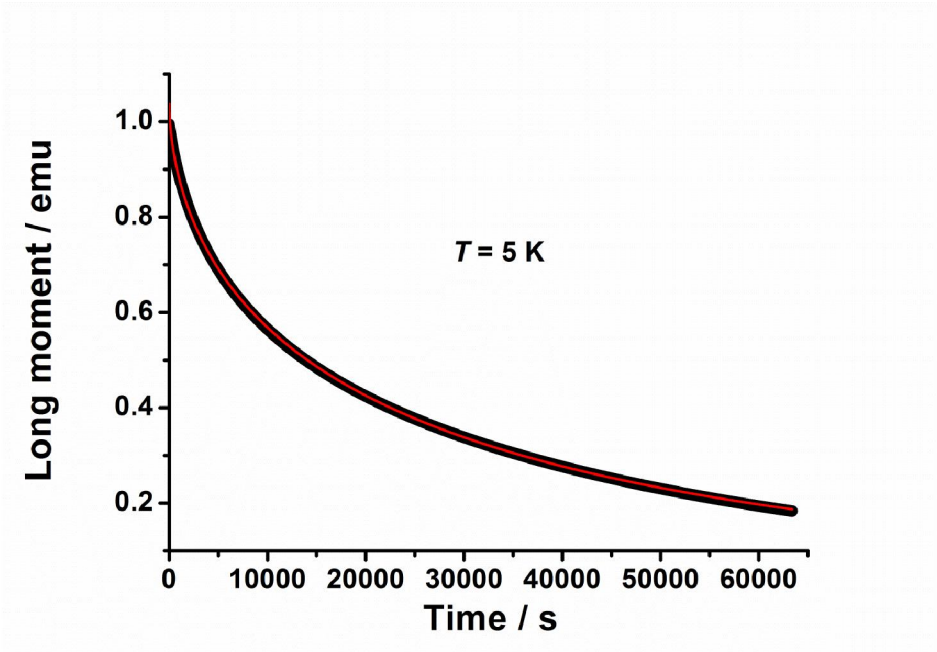

Fig. S46. Plot of magnetization decay *vs.* time used to derive relaxation times for **3** at 5 K. The solid line is the best fit (adjusted $R^2 = 0.99981$).

5

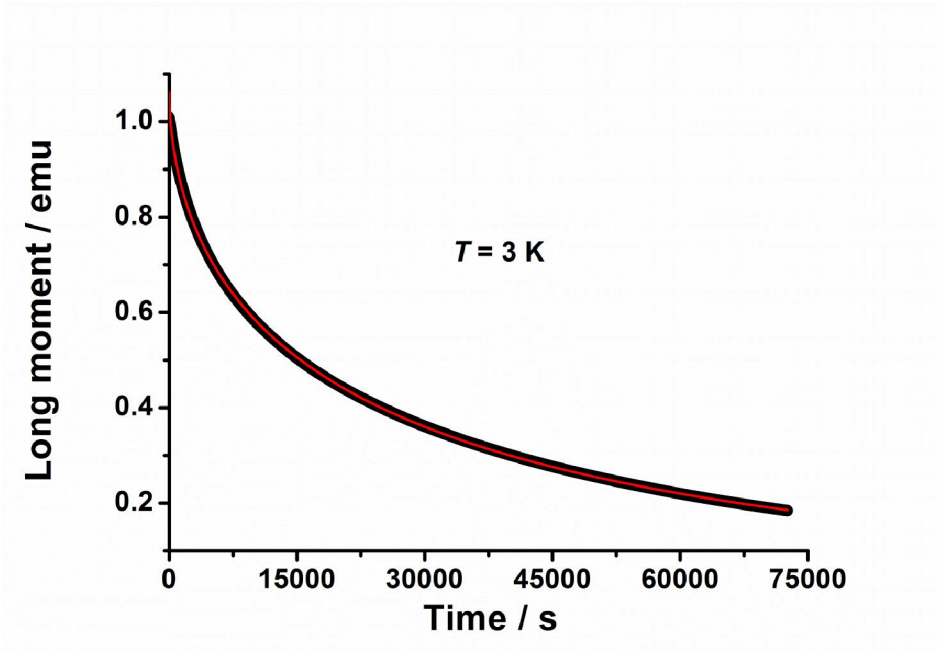

Fig. S47. Plot of magnetization decay *vs.* time used to derive relaxation times for **3** at 3 K. The solid line is the best fit (adjusted $R^2 = 0.99988$).

5

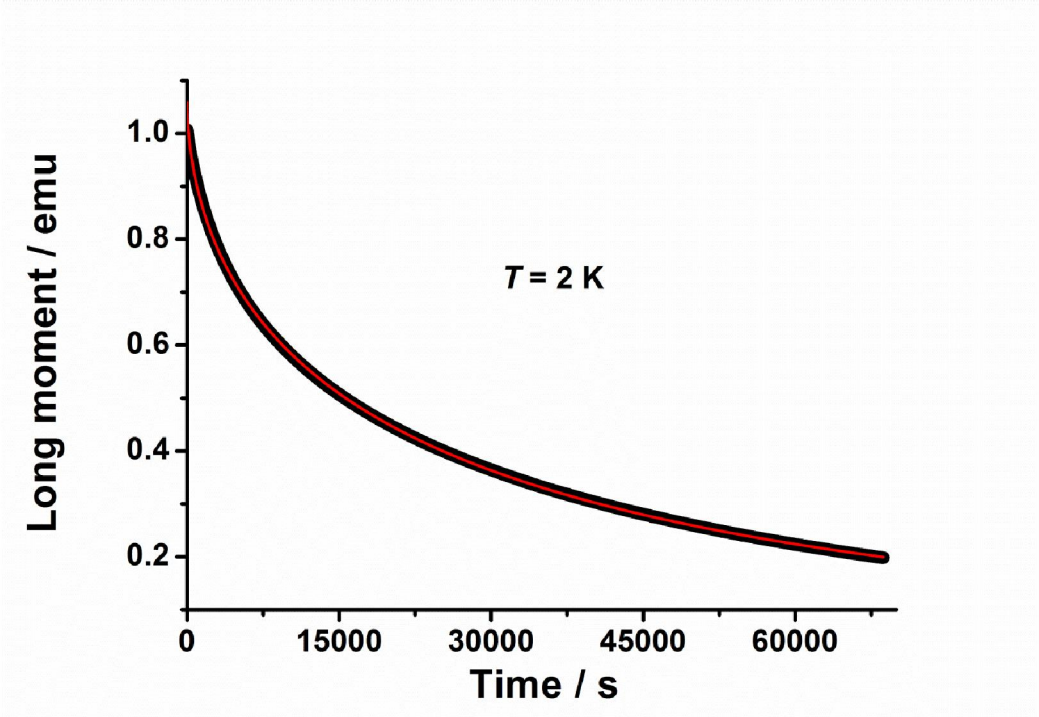

Fig. S48. Plot of magnetization decay *vs.* time used to derive relaxation times for **3** at 2 K. The solid line is the best fit (adjusted $R^2 = 0.99987$).

5

Table S8. Fitting parameters (initial magnetization (M_0), final magnetization (M_f), relaxation time (τ), and generalized coefficient (β)) at different temperatures from the least-squares fitting to the exponential decay as $M(t) = M_f + (M_0 - M_f) \exp[(-(t/\tau)^{\beta}]$, as shown in Figs S28-47.

T / K	M_f	M_0	τ / s	β
83	2.333E-5(1.05456E-6)	9.12426E-4(1.22488E-5)	1.65757(0.03581)	0.99298(0.02524)
80	2.69678E-5(3.87416E-7)	0.0037(3.30042E-6)	3.79986(0.0051)	0.99183(0.00158)
77	2.96495E-5(2.63559E-7)	0.00903(2.77361E-6)	8.7829(0.00397)	0.989(5.14273E-4)
74	3.13749E-5(4.14148E-7)	0.02259(4.20701E-6)	19.42917(0.00526)	0.99038(3.0936E-4)
70	3.81903E-5(3.36062E-7)	0.05387(3.52256E-6)	48.16993(0.0046)	0.99029(1.08888E-4)
65	4.71853E-5(6.12373E-7)	0.10503(5.84923E-6)	102.2216(0.00822)	0.99004(9.23419E-5)
60	5.29568E-5(7.99987E-7)	0.14681(7.11692E-6)	155.65568(0.01085)	0.98951(8.0585E-5)
55	5.51123E-5(5.37387E-7)	0.18458(6.36993E-6)	209.73978(0.01047)	0.98915(5.60495E-5)
50	7.23388E-5(8.6869E-7)	0.22575(8.25764E-6)	277.48637(0.0146)	0.98836(6.0199E-5)
45	7.36067E-5(7.55136E-7)	0.275(8.88649E-6)	372.30721(0.01741)	0.98624(5.21485E-5)
40	7.9442E-5(6.04084E-7)	0.33329(8.4102E-6)	513.33216(0.01882)	0.98311(4.01327E-5)
35	1.03945E-4(1.10555E-6)	0.4027(1.13401E-5)	734.77403(0.02993)	0.97971(4.53101E-5)
30	1.44376E-4(1.42303E-6)	0.48457(1.26912E-5)	1104.31405(0.04179)	0.97338(4.2207E-5)
25	1.46218E-4(1.04778E-6)	0.58096(1.18356E-5)	1771.66403(0.05294)	0.96081(3.14904E-5)
20	2.19179E-4(9.35164E-7)	0.69231(1.01541E-5)	3098.24988(0.06771)	0.93437(2.17103E-5)
15	0¶	0.81241(7.99746E-6)	6110.46111(0.08463)	0.87563(1.7337E-5)
10	0¶	0.93921(8.03942E-4)	14141.90002(42.164)	0.7215(0.00181)
5	0¶	1.03842(1.61675E-4)	24495.33818(17.802)	0.56612(2.55531E-4)
3	0.00384(2.05664E-4)	1.06255(1.29131E-4)	25686.06941(13.116)	0.54542(1.83166E-4)
2	0.01669(2.27147E-4)	1.05863(1.35629E-4)	25219.21229(14.401)	0.55272(2.02263E-4)

¶ These parameter values were restricted to non-negative.

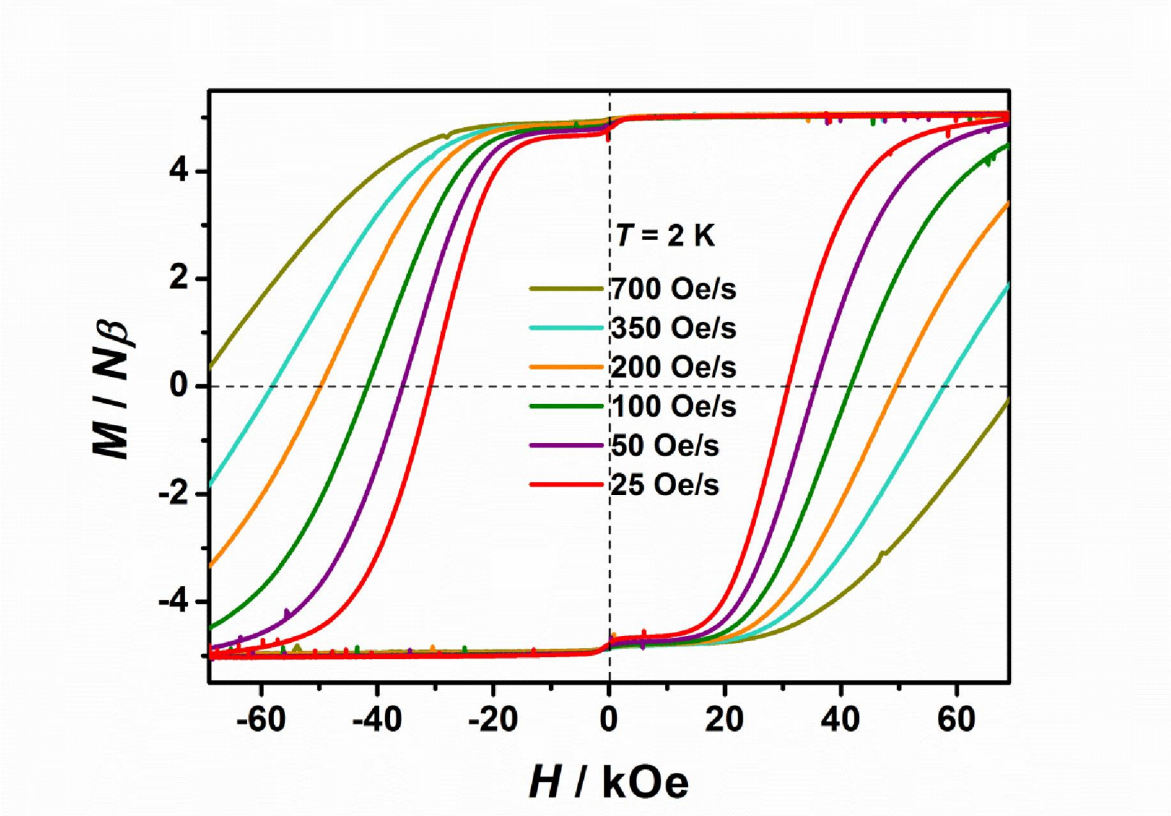

Fig. S49. Magnetic hysteresis loops for **3**, continuously collected at 2 K for selected field ramping speeds.

Table S9. Coercive fields for 3 at different sweep rate at 2 K, corresponding to Fig. S49.

Sweep rate / Oe s^{-1}	Coercive field / Oe
700	> 70000
350	58146
200	49741
100	41722
50	35632
25	30893

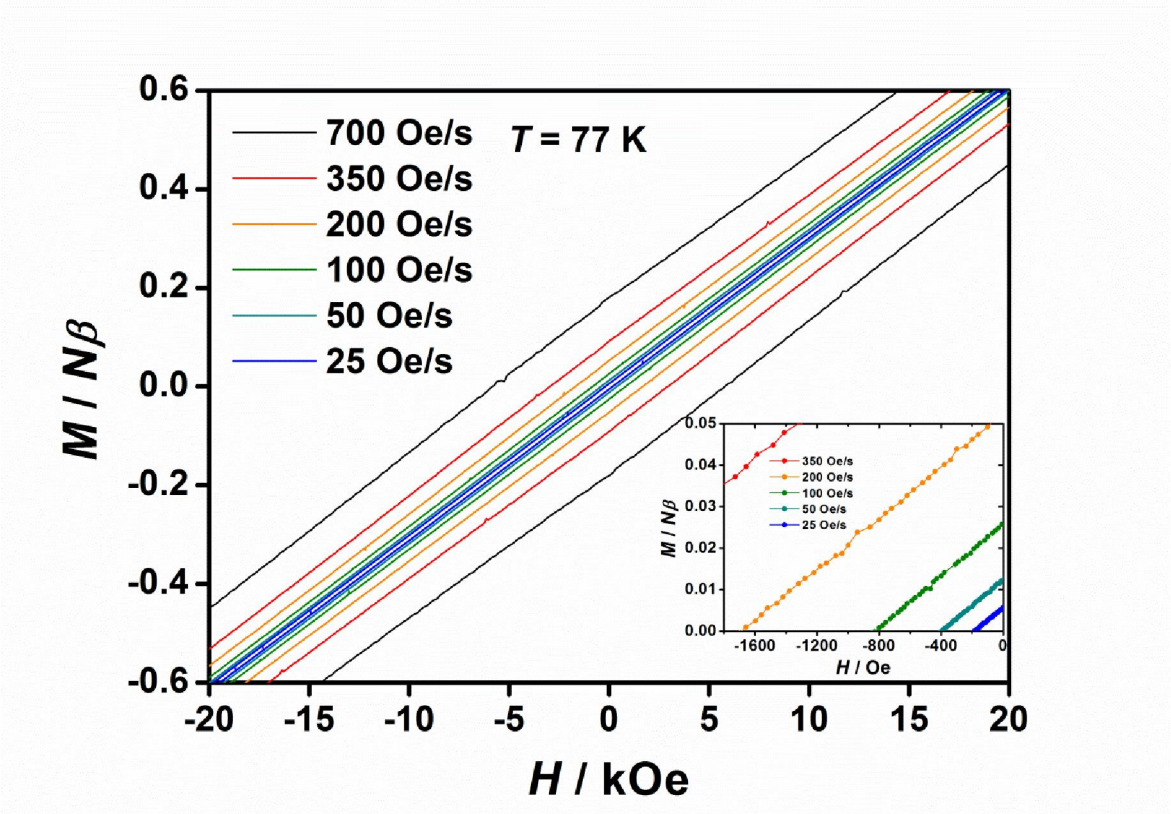

Fig. S50. Magnetic hysteresis loops for **3**, continuously collected at 77 K for selected field ramping speeds. Inset: Local zoom plot of magnetic hysteresis loops for $\mathbf{3}_{\mathbf{Dy}}$ at low field.

Table S10. Coercive fields at different sweep rate at 77 K, corresponding to Fig. S50.

Sweep rate / Oe s^{-1}	Coercive field / Oe
700	5802
350	2946
200	1688
100	825
50	398
25	191

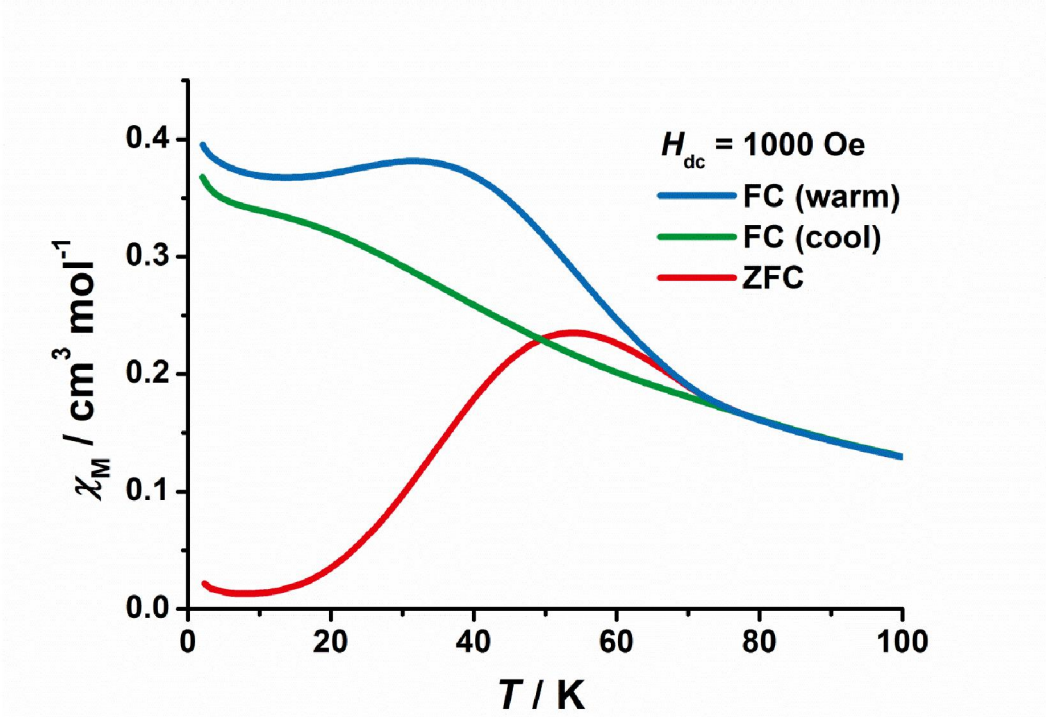

Fig. S51. Field-cooled (FC, blue line) and zero-field-cooled (ZFC, red line) variable-temperature magnetic susceptibility for $\mathbf{3}_{\mathbf{Dy}}$ under 1000 Oe DC filed in warm mode (2 K/min) from 2 to 100 K. The green line represents FC variable-temperature magnetic susceptibility in cool mode (2 K/min) from 100 to 2 K.

Supplementary text:

Computational details:

The static electronic structure was calculated using the multireference XMS-CASPT2//SA-CASSCF/RASSI approach (*33, 34*) and the Molcas quantum chemistry code version 8.2 (*45*). The geometry was extracted from the crystal-structure and the positions of the hydrogen atoms were optimized at density function theory (DFT) level using the same level of theory as in the frequency calculations (*vide infra*) while the coordinates of the heavier atoms were fixed to their XRD-determined positions. The nine 4f electrons and the seven 4f orbitals of the Dy(III) ion were used as the active space. Relativistically contracted atomic natural orbital (ANO-RCC) basis sets were used throughout (*46, 47*). A polarized valence quadruple-ζ quality (ANO-RCC-QZVP, [9s8p6d4f3g2h] contraction) basis set was used for the Dy(III) ion, polarized valence triple-ζ quality (ANO-RCC-VTZP, [4s3p2d1f] contraction) basis set was used for the carbon atoms in the Cp rings, and polarized valence double-ζ quality (ANO-RCC-VDZP, [3s2p1d] and [2s1p] contractions) basis sets were used for the other C and H atoms. Scalar relativistic effects were treated using the exact two-component (X2C) transformation (*48-50*) as implemented in Molcas. Cholesky decomposition using a threshold of 10^{-8} was used to reduce the storage size of the two-electron integrals.

Three separate state-averaged (SA) complete active space self-consistent field (CASSCF) calculations (*51-54*) were carried out to solve the 21 sextet, 228 quartet, and 490 doublet roots. Then, a series of extended multistate (XMS) complete active space perturbation theory at second order (CASPT2) calculations were conducted on the lowest 21 sextet, 128 quartet, and 130 doublet states corresponding to an energy cut-off of 50,000 cm^{-1} at CASSCF level. The XMS version (*30*) of the well-known CASPT2 approach (*55-58*) was chosen to avoid artificial splitting of spatially degenerate or near-degenerate states observed in the conventional multistate CASPT2 approach (*59*). The XMS-CASPT2 corrections were only calculated to the eigenvalues and no mixing of the CASSCF eigenstates under dynamic electron correlation was taken into account (the "NOMULT" keyword in Molcas). The states chosen into each XMS group correspond to some term or closely spaced group of terms of the free Dy(III) ion. A total of three groups containing 11, 7, and 3 CASSCF states were used for the sextets, twelve groups were containing 13, 7, 19, 9, 15, 17, 5, 11, 3, 9, 7, and 13 CASSCF states were used for the quartet CASSCF states, and ten groups containing 17, 15, 3, 21, 7, 19, 11, 5, 9, and 23 states were used for the doublets. Finally, all states used in the XMS-CASPT2 calculations were mixed by spin-orbit coupling (SOC) using the well-established restricted active space state interaction (RASSI) approach (*59*). The static magnetic properties (***g***-tensors, magnetic susceptibility, and magnetization) were calculated using the SINGLE_ANISO routine (*31, 59, 60*) The CF parameters were calculated using the *ab-initio* crystal-field approach (*33, 34*) as implemented in SINGLE_ANISO.

The vibrational modes were calculated at DFT level using the Gaussian 09 code revision D.01 (*61*). The PBE0 hybrid exchange-correlation functional (*62-65*) was used along with Ahlrichs' TZVP basis sets (*66*). A 4f-in-core effective core potential (ECP), which treated the inner 55 electrons as an effective potential, along with a core-polarized valence triple-ζ quality basis was used for the Dy(III) ion (*67-70*). The geometry was fully optimized without any constraints. Dispersion effects were introduced using the empirical DFT-D3 dispersion correction (*71*) with

the Becke-Johnson damping function (*72*) The "UltraFine" integration grid (99 radial points and 590 angular points per atom) and "tight" convergence criteria (thresholds 1.5 · 10–5, 1.0 · 10–5, 6.0 · 10–5, and 4.0 · 10–5 for maximum force, RMS, force, maximum displacement, and RMS displacement, respectively) were used in Gaussian. All normal modes correspond to bound vibrations.

The differentials of the CF parameters were calculated using single point-calculations at XMS-CASPT2//CASSCF/RASSI level on geometries generated by displacing the equilibrium structure along the normal modes. The total displacement (i.e. the sum of all displaced distances) was normalized to 2.0 Å. Several different values of this number were tried in preliminary calculations to minimize the numerical error and to maximize the stability of the numerical derivatives with respect to small variations of the normalized distance. Two displacements (positive and negative) were used for each normal mode, and the first derivatives of the CF parameters were evaluated using a finite difference method (symmetric derivative). The level of theory in the single point *ab initio* calculations was lowered somewhat to reduce the overall computational costs. The basis set was reduced so that the Dy(III) ion wast treated with a polarized valence triple-ζ quality (ANO-RCC-VTZP) basis set, the carbon atoms in the cyclopentadienyl rings were treated with a polarized valence double-ζ quality (ANO-RCC-VTZP, [8s7p5d3f2g1h] contraction) basis set, and the other atoms were treated with double-ζ (ANO-RCC-VDZ, [3s2p] and [2s] contractions for C and H, respectively) basis sets. In the CASSCF calculations and the subsequent XMS-CASPT2 and RASSI calculations, only the 21 sextet states were considered. This approximation does introduce some error but should still yield results very close to those obtained at a considerably higher cost by calculating also the quartet and doublet states. With the exception of the simplifications listed above, the single-point calculations were carried out at the same level as the calculations on the static electronic structure. The generation of the displaced geometries and the subsequent calculations of the derivatives was carried out using a custom code.

The *ab initio* CF parameters were calculated for the Dy-5* cation following previously established methodology (*32, 33*). The CF parameters that normally correspond to Stevens' original definition of operator equivalents (written as $\hat{O}_{kq}^{S}(\hat{\mathbf{J}})$) were converted to the newer Iwahara-Chibotaru definition (written as $\hat{O}_{kq}(\hat{\mathbf{J}})$) of the CF Hamiltonian (*73, 74*):

$$\hat{H}_{CF} = \sum_{kq} B_{kq} \hat{O}_{kq}(\hat{\mathbf{J}}) = \sum_{kq} B_{kq} \frac{\hat{O}_{kq}^{S}(\hat{\mathbf{J}})}{O_{k0}^{S}(J)} \quad (1)$$

where B_{kq} are the CF parameters and $O_{k0}^{S}(J)$ is obtained from $\hat{O}_{kq}^{S}(\hat{\mathbf{J}})$ by the replacement $\hat{J}_z \rightarrow J$. The ranks, k, are even numbers and run up to $2J$. The components q run from $-k$ to k for each rank k. The newer definition of the operator equivalents has several advantages over the conventional definition; namely, the matrix elements of the operators are always of order unity and the magnitudes of the parameters are therefore easy to compare between different operator ranks. Furthermore, a simple general expression is available for the matrix elements, and the magnitudes of the CF parameters are symmetric in q: $|B_{kq}| = |B_{k-q}|$. The main disadvantage of the definition is that the off-diagonal CF parameters are complex. We are, however, mostly interested in the magnitudes of the parameters as these enter the expressions for the transition probabilities (*vide infra*).

The first- and second-order contributions of optical phonons to the electronic part of the spin-phonon coupling Hamiltonian can be estimated as (*74, 75*):

$$\hat{H}_{sp}^{(1)} = \sum_{n} Q_n \sum_{kq} \left| \frac{\partial B_{kq}}{\partial Q_n} \right|_{Q_n=0} \hat{O}_{kq}(\hat{\mathbf{J}}) \quad (2)$$

$$\hat{H}_{sp}^{(2)} = \sum_{nm} Q_n Q_m \sum_{kq} \left| \frac{\partial^2 B_{kq}}{\partial Q_n \partial Q_m} \right|_{Q_n, Q_m=0} \hat{O}_{kq}(\hat{\mathbf{J}}) \quad (3)$$

where Q_n is displacement along the nth normal mode, B_{kq} are CF parameters in the Iwahara–Chibotaru definition, and $\hat{O}_{kq}(\hat{\mathbf{J}})$ are operator equivalents in the Iwahara–Chibotaru definition. The transition probabilities between CF states $|\psi\rangle$ and $|\psi'\rangle$ following the direct, first-order Raman, and second-order Raman mechanisms, in that order, are given by (*42, 74, 76*):

$$P(\psi \leftarrow \psi') = \frac{2\pi}{\hbar^2}\left|\left\langle\psi\left|\hat{H}_{sp}^{(1)}\right|\psi'\right\rangle\right|^2 f(\omega), \quad (4)$$

$$P(\psi \leftarrow \psi') = \frac{2\pi}{\hbar^2}\left|\left\langle\psi\left|\hat{H}_{sp}^{(2)}\right|\psi'\right\rangle\right|^2 f(\omega), \text{ and} \quad (5)$$

$$P(\psi \leftarrow \psi') = \frac{2\pi}{\hbar^2}\left|\frac{\left\langle\psi\left|\hat{H}_{sp}^{(1)}\right|\psi''\right\rangle\left\langle\psi''\left|\hat{H}_{sp}^{(1)}\right|\psi'\right\rangle}{\Delta}\right|^2 f(\omega), \quad (6)$$

where $\hbar$ is the reduced Planck constant, $f(\omega)$ is a factor depending on the vibrational modes and the energy difference between the states $|\psi\rangle$ and $|\psi'\rangle$, $|\psi''\rangle$ is an intermediate state in the first-order Raman process, and Δ is the energy of the intermediate state relative to the initial state. Thus, in each case the spin-phonon transition probability is proportional to the matrix elements of the first- or second-order spin-phonon coupling Hamiltonian. The actual Orbach process consists of several consecutive direct transitions.

The normal modes of Dy-5* were calculated at density functional theory (DFT) level and the respective frequencies are listed in Table S15. This introduces some approximation as the geometry must be optimized and a gas-phase optimization necessarily excludes crystal-packing effects. Furthermore, the effect of 4f configuration and 4f–ligand covalency were neglected in the calculations as these are difficult to treat at DFT-level. The optimized bond distances between the Dy ion and the centroids of the Cp* and Cp$^{i\text{Pr5}}$ rings are 2.322 Å and 2.304 Å, respectively, and the Cp*–Dy–Cp$^{i\text{Pr5}}$ angle is 158.42°. The respective experimentally determined parameters are 2.296(1) Å, 2.284(1) Å, and 162.507(1) Å. Although, the geometric parameters are qualitatively similar, the calculated bond-lengths are overestimated roughly by 0.02 Å most likely due to the fact that the 4f–ligand covalency is neglected. The calculated bend angle is also slightly more acute. Although the errors in the bond lengths are less than a percent and the error in the bend angle is less than three percent, these deviations are large enough to cause quantitative errors in the calculated CF parameters.

To analyze the extent to which different approximation in the calculations affect the results, the CF splitting of the ground $^6H_{15/2}$ multiplet was calculated on the optimized geometry using the same level of theory used in the evaluation of the spin-phonon couplings (see section Computational details for further details). The results are listed in Table S16. The CF splitting calculated on the DFT-optimized geometry is roughly 75% of that calculated on the crystal structure geometry. This is consistent with the overestimated Dy–ligand distances. Despite these errors, the splitting is still qualitatively correct, and since the evaluation of derivatives concerns energy differences of slightly distorted structures, most of the error present in the absolute values of the splittings should cancel, and the evaluated energy differences should be much more accurate than the absolute splittings. Thus, the 25% error in the splittings defines the maximum error in the derivatives and the actual errors should be much smaller. It is therefore reasonable to assume that

the errors originating from the DFT optimization are not much larger than the errors originating from assuming that the molecular vibrations are an approximation of the optical phonons.

The first derivatives of the CF parameters with respect to each of the 237 normal modes of Dy-5* were numerically evaluated by single point calculations at XMS-CASPT2//SA-CASSCF/SO-RASSI level on geometries displaced in positive and negative directions along the normal modes. Evaluation of the second derivatives, although in principle possible, is unfeasible in terms of computational time required. Thus, the vibrational contributions to first-order Raman relaxation were not evaluated. Only operator equivalents up to rank $k = 6$ were considered. In principle, operators up to rank $k = 14$ can make contributions and the derivatives were calculated, but the small values of the respective CF parameters and resulting derivatives makes it impossible to reliably distinguish the values from numerical noise. Since only the magnitudes of the derivatives enter the final relaxation rate expressions, only these are considered, and since $|B_{kq}| = |B_{k-q}|$, only positives values of q are listed. The squared magnitudes of the first derivatives are listed in Table S17.

It is clear that the largest derivatives are those of the 2nd rank parameters and, thus, these terms in the operator lead to the largest matrix elements and the first-order (non-Raman) relaxation can be qualitatively understood by considering the 2nd rank terms only. The states in the lowest six doublets have very large projections on some $|JM\rangle$ state, and can be, to a first approximation, considered as pure $|JM\rangle$ states: $|\psi\rangle \sim |JM\rangle$ and $|\psi'\rangle \sim |JM'\rangle$. Then, the $\hat{O}_{2\pm2}(\hat{\mathbf{J}})$ operators induce direct transitions between two $|JM\rangle$ states differing by $\Delta M = M - M' = \pm 2$, the $\hat{O}_{2\pm1}(\hat{\mathbf{J}})$ operators induce transitions between neighboring states differing by $\Delta M = \pm 1$, and the $\hat{O}_{20}(\hat{\mathbf{J}})$ operator does not induce any transitions. If one confines themselves to the lowest six doublets (the seventh and eighth doublets do not take part in the Orbach process based on the experimental effective barrier height and on the extent of QTM due to the transverse components of the $\boldsymbol{g}$-tensors), the energy range of the $\Delta M = \pm 1$ transitions (the energy difference between the relevant doublets) ranges from 432 cm^{-1} to 1061 cm^{-1} and the energy range of the $\Delta M = \pm 2$ transitions from 212 cm^{-1} to 672 cm^{-1}. The normal modes within these energy scales causing the largest spin-phonon couplings $\left|\partial B_{2\pm1}/Q_n\right|^2$ and $\left|\partial B_{2\pm2}/Q_n\right|^2$ are listed in Table S18.

Examining the values in Table S18, the respective vibrational modes, and confining the analysis to vibrational modes that cause spin-phonon couplings larger than $\left|\partial B_{2\pm1}/Q_n\right|^2 = 1000$ and $\left|\partial B_{2\pm1}/Q_n\right|^2 = 1000$, all relevant spin-phonon couplings are associated to vibrational modes of the Cp cores of the Cp$^{i\mathrm{Pr5}}$ and Cp* ligands. Only the modes 75 and 98 are mostly confined to the $i\mathrm{Pr}_5$ and CH_3 groups, respectively, with minor coupling to the Cp ring vibrations. The largest $\left|\partial B_{2\pm1}/Q_n\right|^2$ couplings are caused by rocking vibrations where the Cp core rocks relative to the rest of the molecular structure. The modes 54 and 55, which cause the most significant spin-phonon couplings, are associated to rocking of the Cp core of the Cp* ligand and the modes 67 and 68 are associated to the rocking of the Cp core of the Cp$^{i\mathrm{Pr5}}$ ligand. The modes 70 and 71 are out-of-plane vibrations of the Cp* ligand with significant coupling with CH_3 vibrations and mode 66 corresponds to a symmetric in-plane stretching vibration of the Cp$^{i\mathrm{Pr5}}$ ligand. The $\left|\partial B_{2\pm1}/Q_n\right|^2$ couplings are caused by a variety of modes including in-plane asymmetric vibrations of the Cp$^{i\mathrm{Pr5}}$ ligand (modes 73, 97, and 100) and the Cp* ligand (mode 62); out-of-plane vibrations of the Cp$^{i\mathrm{Pr5}}$

ligand (modes 70, 74, and 75) and the Cp* ligand (modes 71); in-plane symmetric vibrations of the Cp^{iPr5} ligand (modes 79) and the Cp* ligand (modes 63, 90, 92); and rocking of the Cp^{iPr5} ligand (modes 67 and 68) and the Cp* ligand (modes 54 and 55).

5

Table S11. The energies, principal values of the g-tensors, the directions of the principal magnetic axes, and the angle between the principal axis of the ground doublet (θ) of the eight lowest Kramers' doublets (KDs) in **3** corresponding to the CF-split states of the $^6H_{15/2}$ multiplet.

KD	E / cm^{-1}	g_x	g_y	g_z	θ/°
1	0	0.00000	0.00000	20.00428	-
2	672	0.00005	0.00006	16.93927	2.3
3	1061	0.00662	0.00715	14.35416	4.2
4	1304	0.03384	0.04607	11.74560	2.6
5	1524	0.05323	0.13563	9.06000	5.3
6	1736	2.27195	3.02978	6.08129	5.1
7	1903	9.37909	6.51116	2.56325	0.9
8	2104	0.33393	1.09830	17.47525	90.3

Table S12. The squared projections of the CF eigenstates corresponding to the states in the eight lowest Kramers' doublets (KD) on the angular momentum eigenstates $|JM\rangle$.

M	KD 1		KD 2		KD3		KD 4	
+15/2	**1.000**	0.000	0.000	0.000	0.000	0.000	0.000	0.000
+13/2	0.000	0.000	**0.998**	0.000	0.002	0.000	0.000	0.000
+11/2	0.000	0.000	0.002	0.000	**0.986**	0.000	0.010	0.000
+9/2	0.000	0.000	0.000	0.000	0.010	0.000	**0.982**	0.000
+7/2	0.000	0.000	0.000	0.000	0.002	0.000	0.004	0.000
+5/2	0.000	0.000	0.000	0.000	0.000	0.000	0.003	0.000
+3/2	0.000	0.000	0.000	0.000	0.000	0.000	0.000	0.000
+1/2	0.000	0.000	0.000	0.000	0.000	0.000	0.000	0.000
–1/2	0.000	0.000	0.000	0.000	0.000	0.000	0.000	0.000
–3/2	0.000	0.000	0.000	0.000	0.000	0.000	0.000	0.000
–5/2	0.000	0.000	0.000	0.000	0.000	0.000	0.000	0.003
–7/2	0.000	0.000	0.000	0.000	0.000	0.002	0.000	0.004
–9/2	0.000	0.000	0.000	0.000	0.000	0.010	0.000	**0.982**
–11/2	0.000	0.000	0.000	0.002	0.000	**0.986**	0.000	0.010
–13/2	0.000	0.000	0.000	**0.998**	0.000	0.002	0.000	0.000
–15/2	0.000	**1.000**	0.000	0.000	0.000	0.000	0.000	0.000

M	KD 5		KD 6		KD 7		KD 8	
+15/2	0.000	0.000	0.000	0.000	0.000	0.000	0.000	0.000
+13/2	0.000	0.000	0.000	0.000	0.000	0.000	0.000	0.000
+11/2	0.001	0.000	0.000	0.000	0.000	0.000	0.000	0.000
+9/2	0.005	0.000	0.002	0.000	0.000	0.000	0.000	0.000
+7/2	**0.992**	0.000	0.001	0.000	0.000	0.000	0.000	0.000
+5/2	0.001	0.000	**0.961**	0.001	0.010	0.019	0.007	0.000
+3/2	0.000	0.000	0.000	0.014	**0.566**	**0.234**	**0.016**	**0.170**
+1/2	0.000	0.000	0.021	0.000	**0.058**	**0.114**	**0.749**	**0.058**
–1/2	0.000	0.000	0.000	0.021	**0.114**	**0.058**	**0.058**	**0.749**
–3/2	0.000	0.000	0.014	0.000	**0.234**	**0.566**	**0.170**	**0.016**
–5/2	0.000	0.001	0.001	**0.961**	0.019	0.010	0.000	0.007
–7/2	0.000	**0.992**	0.000	0.001	0.000	0.000	0.000	0.000
–9/2	0.000	0.005	0.000	0.002	0.000	0.000	0.000	0.000
–11/2	0.000	0.001	0.000	0.000	0.000	0.000	0.000	0.000
–13/2	0.000	0.000	0.000	0.000	0.000	0.000	0.000	0.000
–15/2	0.000	0.000	0.000	0.000	0.000	0.000	0.000	0.000

Table S13. *Ab initio* CF parameters for **3** using the Iwahara–Chibotaru definition (*72, 73*):

k	q	Re(B_{kq})	Im(B_{kq})	$\|B_{kq}\|$
2	-2	28.649	-9.636	30.226
2	-1	-17.653	-1.239	17.696
2	0	-1195.305	0.000	1195.305
2	1	17.653	-1.239	17.696
2	2	28.649	9.636	30.226
4	-4	-10.782	2.081	10.981
4	-3	0.427	-0.248	0.494
4	-2	-24.584	0.178	24.585
4	-1	1.411	0.410	1.469
4	0	-37.444	0.000	37.444
4	1	-1.411	0.410	1.469
4	2	-24.584	-0.178	24.585
4	3	-0.427	-0.248	0.494
4	4	-10.782	-2.081	10.981
6	-6	-0.559	0.730	0.920
6	-5	1.015	3.785	3.919
6	-4	0.944	2.663	2.825
6	-3	-2.956	-1.541	3.333
6	-2	21.692	-1.398	21.737
6	-1	6.300	0.227	6.304
6	0	-59.535	0.000	59.535
6	1	-6.300	0.227	6.304
6	2	21.692	1.398	21.737
6	3	2.956	-1.541	3.333
6	4	0.944	-2.663	2.825
6	5	-1.015	3.785	3.919
6	6	-0.559	-0.730	0.920
8	-8	-0.020	0.028	0.035
8	-7	-0.010	0.014	0.017
8	-6	0.008	-0.001	0.008
8	-5	-0.073	-0.172	0.186
8	-4	-0.290	-0.237	0.375
8	-3	0.242	0.097	0.261
8	-2	-3.477	0.360	3.495
8	-1	-0.529	-0.034	0.530
8	0	4.484	0.000	4.484
8	1	0.529	-0.034	0.530
8	2	-3.477	-0.360	3.495
8	3	-0.242	0.097	0.261
8	4	-0.290	0.237	0.375
8	5	0.073	-0.172	0.186
8	6	0.008	0.001	0.008
8	7	0.010	0.014	0.017
8	8	-0.020	-0.028	0.035
10	-10	-0.001	0.000	0.001
10	-9	0.000	-0.001	0.001
10	-8	0.001	-0.002	0.003
10	-7	0.003	0.001	0.003
10	-6	-0.001	-0.005	0.005
10	-5	0.003	-0.005	0.006
10	-4	0.027	0.009	0.028
10	-3	0.001	0.010	0.010
10	-2	0.341	-0.038	0.343
10	-1	-0.001	0.000	0.001
10	0	0.012	0.000	0.012
10	1	0.001	0.000	0.001
10	2	0.341	0.038	0.343
10	3	-0.001	0.010	0.010
10	4	0.027	-0.009	0.028
10	5	-0.003	-0.005	0.006
10	6	-0.001	0.005	0.005
10	7	-0.003	0.001	0.003
10	8	0.001	0.002	0.003
10	9	0.000	-0.001	0.001
10	10	-0.001	0.000	0.001

Table S14. Numerical values of the transition magnetic moments of Dy-5* connecting two states belonging to two Kramers doublets (KDs) on the opposite sides or same sides of the barrier.

Barrier-crossing transitions

	KD1	KD2	KD3	KD4	KD5	KD6	KD7	KD8
KD1	0.000005	0.000012	0.000089	0.000088	0.000293	0.000626	0.001926	0.001707
KD2	0.000012	0.000240	0.000425	0.001394	0.000420	0.002808	0.004807	0.008878
KD3	0.000089	0.000425	0.003344	0.003951	0.004044	0.008199	0.012900	0.021555
KD4	0.000088	0.001394	0.003951	0.007630	0.008357	0.050925	0.048651	0.074128
KD5	0.000293	0.000420	0.004044	0.008357	0.014736	0.090351	0.601266	0.278220
KD6	0.000626	0.002808	0.008199	0.050925	0.090351	1.090432	0.335532	0.734593
KD7	0.001926	0.004807	0.012900	0.048651	0.601266	0.335532	2.742924	1.868092
KD8	0.001707	0.008878	0.021555	0.074128	0.278220	0.734593	1.868092	0.203850

Transitions on same side of the barrier

	KD1	KD2	KD3	KD4	KD5	KD6	KD7	KD8
KD1		1.781753	0.113105	0.058649	0.013888	0.005817	0.001070	0.001567
KD2	1.781753		2.374867	0.078361	0.081337	0.024588	0.012556	0.002410
KD3	0.113105	2.374867		2.811686	0.154033	0.026191	0.033527	0.012693
KD4	0.058649	0.078361	2.811686		3.090063	0.157327	0.200615	0.039105
KD5	0.013888	0.081337	0.154033	3.090063		3.223099	0.074974	0.252528
KD6	0.005817	0.024588	0.026191	0.157327	3.223099		3.150441	0.711041
KD7	0.001070	0.012556	0.033527	0.200615	0.074974	3.150441		1.843109
KD8	0.001567	0.002410	0.012693	0.039105	0.252528	0.711041	1.843109	

Table S15. The frequencies (ω, in units cm^{-1}) of the calculated normal modes (n) of Dy-5*

n	ω	n	ω	n	ω	n	ω
1	18.0	61	526.6	121	1221.9	181	1514.3
2	28.6	62	554.9	122	1235.9	182	1516.1
3	39.3	63	555.8	123	1320.2	183	1520.4
4	46.9	64	556.5	124	1329.0	184	1520.7
5	55.3	65	559.4	125	1336.3	185	1522.9
6	58.7	66	574.9	126	1347.1	186	1535.0
7	69.8	67	577.5	127	1351.2	187	1540.2
8	82.3	68	590.6	128	1357.8	188	2949.1
9	95.4	69	605.1	129	1360.4	189	2969.1
10	104.9	70	632.9	130	1363.2	190	3001.1
11	105.5	71	640.5	131	1372.5	191	3042.7
12	112.4	72	713.0	132	1377.7	192	3045.7
13	115.0	73	730.6	133	1381.0	193	3046.5
14	120.8	74	732.5	134	1390.8	194	3047.8
15	126.0	75	754.8	135	1396.1	195	3049.2
16	132.2	76	791.4	136	1397.8	196	3051.3
17	134.0	77	818.0	137	1405.0	197	3052.3
18	141.8	78	822.1	138	1406.3	198	3055.5
19	145.0	79	878.3	139	1407.4	199	3060.8
20	156.7	80	892.2	140	1411.7	200	3062.0
21	165.9	81	902.4	141	1412.6	201	3067.1
22	172.3	82	911.1	142	1415.8	202	3068.0
23	172.8	83	919.2	143	1417.5	203	3069.0
24	175.4	84	925.6	144	1418.5	204	3073.9
25	177.8	85	928.7	145	1421.3	205	3091.4
26	183.1	86	931.0	146	1423.8	206	3095.4
27	186.9	87	931.7	147	1424.7	207	3099.9
28	195.9	88	937.6	148	1432.8	208	3103.3
29	200.3	89	958.9	149	1443.1	209	3105.5
30	212.6	90	961.4	150	1446.5	210	3106.4
31	213.7	91	963.9	151	1450.1	211	3106.9
32	218.8	92	967.2	152	1456.3	212	3107.8
33	236.1	93	970.8	153	1466.2	213	3108.0
34	242.0	94	973.8	154	1467.5	214	3109.0
35	244.2	95	976.3	155	1469.1	215	3118.2
36	248.7	96	1033.3	156	1472.3	216	3119.6
37	254.0	97	1037.3	157	1473.9	217	3127.4
38	265.4	98	1037.7	158	1475.2	218	3127.6
39	270.9	99	1043.8	159	1476.8	219	3131.2

40	272.3	100	1045.0	160	1478.6	220	3131.6
41	276.4	101	1045.3	161	1481.1	221	3133.9
42	279.0	102	1048.4	162	1483.3	222	3135.8
43	280.1	103	1074.8	163	1484.5	223	3137.3
44	288.7	104	1085.3	164	1485.1	224	3138.5
45	292.0	105	1085.8	165	1485.9	225	3141.2
46	294.5	106	1086.7	166	1486.7	226	3141.3
47	302.1	107	1120.6	167	1488.6	227	3141.6
48	308.6	108	1122.6	168	1489.7	228	3151.5
49	317.2	109	1136.4	169	1490.9	229	3151.9
50	338.1	110	1142.6	170	1491.9	230	3153.9
51	350.8	111	1146.9	171	1492.7	231	3155.2
52	356.6	112	1150.3	172	1495.3	232	3155.5
53	373.7	113	1153.7	173	1497.1	233	3160.0
54	394.7	114	1156.6	174	1502.3	234	3162.0
55	409.7	115	1167.6	175	1506.5	235	3173.4
56	440.6	116	1182.9	176	1507.9	236	3182.6
57	458.4	117	1193.6	177	1509.4	237	3188.1
58	465.9	118	1193.7	178	1512.5		
59	489.6	119	1196.9	179	1512.7		
60	510.7	120	1202.9	180	1514.1		

Table S16. The CF splitting of the ground $^6H_{15/2}$ multiplet of Dy-5* as calculated using crystal structure and optimized geometry and different levels of theory

KD	Full level of theory[#] Crystal structure	Lower level of theory[**] DFT geometry
1	0	0
2	672	539
3	1061	824
4	1304	992
5	1524	1143
6	1736	1293
7	1903	1414
8	2104	1536

[#] XMS-CASPT2//SA-CASSCF/SO-RASSI, 50,000 cm^{-1} cutoff for states in XMS-CASPT2 and SO-RASSI calculations.
[**] XMS-CASPT2//SA-CASSCF/SO-RASSI with only sextets included in the XMS-CASPT2 and SO-RASSI calculations

Table S17. The squared magnitudes of the first derivatives of the CF parameters with respect to the normal modes (n, ω) of Dy-5*.

n	ω / cm^{-1}	q	$\lvert\partial B_{kq}/Q_n\rvert^2$ $k=2$	$k=4$	$k=6$
1	18.0	0	3.6	0.0	0.4
		1	66.5	0.7	3.1
		2	91.1	2.2	33.7
		3		0.4	1.9
		4		4.9	0.9
		5			0.2
		6			0.3
2	28.6	0	0.2	1.5	1.0
		1	72.9	1.6	2.2
		2	112.4	1.5	28.0
		3		0.5	2.3
		4		1.6	0.1
		5			0.0
		6			0.5
3	39.3	0	79.7	0.7	6.2
		1	304.3	0.0	9.2
		2	206.4	0.9	8.5
		3		0.3	0.7
		4		0.4	0.1
		5			0.0
		6			0.0
4	46.9	0	112.9	0.2	32.6
		1	68.4	0.0	1.2
		2	32.0	0.1	14.2
		3		0.0	0.0
		4		1.0	0.2
		5			0.1
		6			0.1
5	55.3	0	369.1	0.0	41.7
		1	17.1	0.4	1.0
		2	288.4	4.3	7.7
		3		0.3	0.3
		4		0.4	0.0
		5			0.1
		6			0.2
6	58.7	0	35.9	2.1	26.7
		1	265.7	0.4	13.4
121	1221.9	0	287.4	0.5	2.9
		1	629.0	1.3	1.8
		2	4837.7	16.4	2.6
		3		41.1	9.7
		4		6.0	2.4
		5			0.3
		6			0.0
122	1235.9	0	42.4	4.1	1.3
		1	576.5	17.1	2.1
		2	9673.8	96.5	31.6
		3		36.1	9.1
		4		0.3	0.4
		5			0.0
		6			0.2
123	1320.2	0	100.7	1.2	0.8
		1	168.3	0.0	4.3
		2	821.7	10.7	0.4
		3		23.1	11.0
		4		1.5	1.4
		5			0.1
		6			0.2
124	1329.0	0	1151.9	0.0	9.0
		1	67.0	1.7	3.3
		2	441.8	8.6	6.7
		3		17.7	8.2
		4		0.3	2.7
		5			0.1
		6			0.0
125	1336.3	0	25.0	0.8	1.7
		1	109.1	0.4	2.6
		2	176.6	4.2	3.5
		3		6.0	4.1
		4		0.0	0.7
		5			0.1
		6			0.0
126	1347.1	0	298.0	0.0	0.2
		1	33.3	0.0	1.2

		2	419.1	4.9	1.4			2	683.9	3.5	0.3
		3		1.2	0.2			3		2.5	1.2
		4		0.2	0.1			4		0.0	0.1
		5			0.1			5			0.0
		6			0.3			6			0.1
7	69.8	0	438.6	0.1	23.7	127	1351.2	0	0.7	1.1	2.4
		1	82.3	0.4	3.3			1	189.5	0.3	1.0
		2	14.5	0.3	2.6			2	2098.8	5.4	1.3
		3		0.2	0.4			3		6.3	2.7
		4		1.7	0.1			4		0.4	0.4
		5			0.1			5			0.1
		6			0.3			6			0.1
8	82.3	0	3.5	1.2	1.3	128	1357.8	0	380.5	0.7	10.6
		1	13.3	0.9	0.0			1	118.1	0.7	0.2
		2	20.4	0.1	0.1			2	367.9	1.1	2.4
		3		0.1	0.2			3		6.9	3.9
		4		0.4	0.0			4		1.0	1.6
		5			0.0			5			0.0
		6			0.0			6			0.5
9	95.4	0	354.2	15.9	3.1	129	1360.4	0	11.1	0.1	0.2
		1	33.7	0.6	5.6			1	103.9	0.7	2.0
		2	210.5	0.9	2.0			2	1261.0	9.7	3.9
		3		0.2	0.3			3		12.7	6.7
		4		2.4	0.6			4		1.9	1.2
		5			0.0			5			0.0
		6			0.2			6			0.0
10	104.9	0	46.8	3.7	0.6	130	1363.2	0	121.4	0.1	3.6
		1	11.9	0.7	1.5			1	50.9	2.5	0.5
		2	34.2	3.4	4.5			2	370.2	5.7	8.1
		3		0.3	0.1			3		2.2	2.2
		4		0.6	0.3			4		0.6	0.7
		5			0.0			5			0.1
		6			0.2			6			0.2
11	105.5	0	194.3	4.8	25.8	131	1372.5	0	3.7	0.4	3.0
		1	0.5	3.7	1.8			1	125.9	5.2	2.1
		2	32.7	0.1	2.0			2	121.1	2.8	2.4
		3		0.2	0.0			3		5.1	2.6
		4		0.8	0.6			4		0.4	0.6
		5			0.1			5			0.9
		6			0.0			6			0.7
12	112.4	0	36.2	0.1	5.8	132	1377.7	0	329.6	7.2	0.8

		1	17.3	0.3	0.1			1	42.0	0.6	0.7
		2	12.6	0.2	0.2			2	160.8	13.9	11.4
		3		0.4	0.6			3		5.7	5.3
		4		0.1	0.0			4		0.6	1.7
		5			0.0			5			0.0
		6			0.0			6			0.0
13	115.0	0	11.4	0.3	21.4	133	1381.0	0	227.6	0.4	4.8
		1	9.2	0.6	0.3			1	55.2	3.8	0.1
		2	10.6	0.0	1.6			2	171.1	6.6	9.0
		3		0.4	0.1			3		8.3	11.8
		4		0.2	0.2			4		0.1	2.8
		5			0.1			5			0.0
		6			0.0			6			0.0
14	120.8	0	107.0	0.2	35.6	134	1390.8	0	324.4	0.0	2.1
		1	6.8	0.3	0.7			1	2.5	0.1	1.1
		2	114.6	2.3	10.1			2	2.8	2.8	1.2
		3		0.2	0.2			3		1.4	0.1
		4		1.4	0.1			4		0.8	0.4
		5			0.2			5			0.4
		6			0.0			6			0.8
15	126.0	0	216.1	17.3	8.9	135	1396.1	0	53.1	0.2	0.8
		1	1.9	1.2	5.2			1	11.8	0.2	0.0
		2	9.0	0.9	5.3			2	24.9	0.4	0.2
		3		0.1	0.3			3		0.2	0.1
		4		2.3	0.6			4		0.1	0.2
		5			0.1			5			0.0
		6			0.4			6			0.0
16	132.2	0	34.7	47.5	55.0	136	1397.8	0	4.1	0.1	0.1
		1	24.1	0.0	9.1			1	4.6	0.1	0.1
		2	26.0	1.6	13.9			2	52.5	0.0	0.3
		3		0.0	2.0			3		0.1	0.0
		4		1.3	0.4			4		0.2	0.0
		5			0.3			5			0.0
		6			0.4			6			0.0
17	134.0	0	1.3	0.4	0.3	137	1405.0	0	11.0	17.1	0.2
		1	6.0	3.0	3.0			1	61.5	1.3	0.3
		2	27.8	0.4	2.8			2	2382.1	6.5	1.2
		3		0.1	0.8			3		7.4	3.7
		4		1.2	0.1			4		1.1	0.3
		5			0.1			5			0.0
		6			0.1			6			0.5

18	141.8	0	21.6	0.1	0.3	138	1406.3	0	6.9	30.9	5.4
		1	1.8	4.5	2.6			1	86.8	0.0	0.8
		2	8.9	0.7	4.9			2	1318.6	13.3	5.5
		3		0.8	1.0			3		1.1	0.5
		4		0.6	0.0			4		0.0	0.3
		5			0.1			5			0.0
		6			0.1			6			0.0
19	145.0	0	107.6	5.6	0.1	139	1407.4	0	44.9	0.1	1.1
		1	91.9	0.4	2.3			1	171.6	0.1	0.1
		2	42.9	0.2	0.8			2	2479.8	0.6	1.2
		3		0.3	0.3			3		18.9	6.3
		4		0.1	0.1			4		0.2	1.4
		5			0.1			5			0.1
		6			0.1			6			0.0
20	156.7	0	90.9	10.9	9.4	140	1411.7	0	21.7	0.3	0.9
		1	115.1	5.0	3.7			1	0.9	0.2	0.2
		2	88.5	4.1	1.6			2	23.0	0.3	0.1
		3		1.5	1.9			3		0.1	0.1
		4		2.0	0.2			4		0.1	0.0
		5			0.4			5			0.0
		6			0.0			6			0.0
21	165.9	0	229.8	3.4	36.0	141	1412.6	0	130.4	1.4	0.2
		1	254.4	5.4	1.1			1	1.0	0.0	0.5
		2	100.8	6.0	4.8			2	53.9	0.4	0.3
		3		0.1	2.1			3		0.6	0.4
		4		3.2	0.2			4		0.3	0.1
		5			0.2			5			0.0
		6			0.3			6			0.0
22	172.3	0	163.6	0.2	6.6	142	1415.8	0	17.5	0.0	0.0
		1	89.7	3.1	1.5			1	1.0	0.3	0.1
		2	123.0	6.1	4.2			2	24.0	0.1	0.3
		3		0.1	0.0			3		0.1	0.1
		4		2.8	0.4			4		0.0	0.0
		5			0.4			5			0.0
		6			0.1			6			0.0
23	172.8	0	64.0	12.4	25.6	143	1417.5	0	205.5	10.9	4.9
		1	72.9	2.1	2.1			1	2.1	0.0	0.1
		2	16.6	3.5	6.0			2	298.9	0.4	1.7
		3		0.1	0.4			3		3.7	2.2
		4		0.2	0.1			4		0.0	0.1
		5			0.2			5			0.1

		6			0.5			6			0.0
24	175.4	0	447.2	1.3	2.5	144	1418.5	0	18.6	65.9	0.3
		1	185.4	5.7	2.4			1	1.0	3.4	0.9
		2	61.2	5.3	5.1			2	121.7	2.7	6.0
		3		0.7	0.6			3		8.7	4.4
		4		1.2	0.5			4		0.2	0.2
		5			0.0			5			0.5
		6			0.0			6			0.0
25	177.8	0	3.6	0.3	33.9	145	1421.3	0	93.1	0.0	1.0
		1	13.4	0.5	0.7			1	35.6	1.7	0.1
		2	80.3	0.9	1.4			2	275.0	4.3	3.0
		3		0.1	0.1			3		4.7	2.2
		4		0.1	0.1			4		0.1	0.7
		5			0.2			5			0.0
		6			0.0			6			0.0
26	183.1	0	334.3	2.4	0.7	146	1423.8	0	616.6	6.3	0.0
		1	268.4	3.3	1.7			1	23.7	1.8	0.5
		2	4.1	0.9	1.1			2	25.2	0.6	0.8
		3		0.0	0.1			3		0.3	0.4
		4		0.7	0.1			4		0.2	0.1
		5			0.1			5			0.0
		6			0.0			6			0.0
27	186.9	0	100.2	0.1	16.4	147	1424.7	0	42.3	3.2	0.8
		1	68.7	1.6	0.7			1	5.0	0.7	0.2
		2	20.8	2.1	1.0			2	9.8	1.0	0.7
		3		0.0	0.0			3		1.0	0.6
		4		0.6	0.8			4		0.4	0.0
		5			0.4			5			0.0
		6			0.8			6			0.0
28	195.9	0	31.7	0.1	2.2	148	1432.8	0	892.1	21.6	0.7
		1	94.4	2.2	0.2			1	3.5	2.3	1.5
		2	77.6	0.2	0.8			2	504.2	1.1	3.9
		3		0.3	0.2			3		14.7	8.5
		4		1.1	0.1			4		1.1	0.2
		5			0.1			5			0.4
		6			0.1			6			0.0
29	200.3	0	571.7	1.7	50.2	149	1443.1	0	290.8	22.5	21.5
		1	591.1	13.1	9.8			1	76.1	6.9	13.5
		2	21.0	0.1	1.9			2	400.9	2.3	2.2
		3		0.2	0.3			3		9.8	20.3
		4		3.1	0.6			4		1.3	11.2

		5			2.2			5			0.2
		6			0.9			6			0.0
30	212.6	0	12.1	0.3	0.3	150	1446.5	0	43.0	10.1	2.1
		1	191.8	3.7	0.7			1	859.9	1.8	4.2
		2	142.4	1.0	0.3			2	334.6	70.6	74.0
		3		0.6	0.0			3		2.6	1.5
		4		2.9	0.2			4		3.6	0.7
		5			0.1			5			1.3
		6			1.7			6			0.1
31	213.7	0	10.9	0.7	0.1	151	1450.1	0	166.1	41.1	0.3
		1	271.0	5.4	0.5			1	234.0	0.3	0.8
		2	293.8	0.0	1.7			2	3153.0	26.8	16.8
		3		0.9	0.8			3		44.6	23.7
		4		0.8	0.4			4		7.4	9.9
		5			0.4			5			0.8
		6			1.3			6			0.2
32	218.8	0	92.4	1.3	0.0	152	1456.3	0	839.1	45.9	0.0
		1	64.0	3.0	1.5			1	1282.8	1.5	1.8
		2	127.7	1.4	1.7			2	1855.7	31.5	14.9
		3		1.9	0.3			3		31.5	28.1
		4		7.8	0.2			4		1.6	1.5
		5			0.0			5			0.3
		6			0.0			6			0.4
33	236.1	0	678.4	28.5	8.7	153	1466.2	0	639.9	90.6	18.4
		1	21.2	11.2	10.1			1	73.7	25.1	24.7
		2	331.4	5.1	0.0			2	174.1	2.6	5.2
		3		2.6	1.4			3		1.9	0.2
		4		22.4	2.8			4		1.6	0.7
		5			0.4			5			0.2
		6			1.9			6			0.0
34	242.0	0	24.7	4.2	0.1	154	1467.5	0	16.0	0.3	0.7
		1	15.8	3.1	1.7			1	22.9	3.9	1.0
		2	39.9	0.4	0.1			2	206.6	8.2	9.2
		3		0.1	0.0			3		0.7	0.2
		4		0.5	0.5			4		1.2	0.1
		5			0.0			5			0.1
		6			0.0			6			0.4
35	244.2	0	3.1	0.2	0.6	155	1469.1	0	46.7	3.1	0.0
		1	33.1	0.1	0.6			1	123.1	1.7	1.3
		2	13.9	1.2	0.3			2	192.0	1.5	0.0
		3		0.4	0.4			3		0.4	0.5

		4		1.0	0.1			4		5.4	0.4
		5			0.1			5			0.0
		6			0.4			6			0.2
36	248.7	0	88.5	0.1	0.1	156	1472.3	0	0.8	25.2	9.3
		1	162.2	4.6	0.1			1	62.1	6.3	1.9
		2	38.3	0.1	0.1			2	49.6	3.6	1.4
		3		1.1	0.8			3		0.3	0.8
		4		2.6	0.0			4		1.0	0.1
		5			0.0			5			0.0
		6			0.0			6			0.0
37	254.0	0	82.4	0.4	0.2	157	1473.9	0	876.5	10.3	14.2
		1	4.8	0.5	1.1			1	28.5	4.4	0.7
		2	219.2	1.5	0.5			2	2687.9	1.2	4.2
		3		0.1	0.7			3		0.8	0.7
		4		1.0	0.6			4		1.8	0.0
		5			0.3			5			0.1
		6			2.7			6			0.8
38	265.4	0	41.2	7.7	1.4	158	1475.2	0	100.9	19.0	1.1
		1	40.0	0.7	2.6			1	41.3	4.2	1.5
		2	144.8	3.3	1.2			2	1422.8	2.2	0.3
		3		0.1	1.1			3		4.8	3.1
		4		0.3	0.2			4		2.3	0.3
		5			0.0			5			0.0
		6			0.6			6			1.0
39	270.9	0	5.4	0.2	5.8	159	1476.8	0	139.7	0.0	0.0
		1	42.8	1.0	0.4			1	77.1	9.0	0.7
		2	62.7	1.9	0.9			2	1091.1	10.4	2.4
		3		0.3	0.2			3		0.9	0.2
		4		4.3	0.2			4		12.8	0.4
		5			0.2			5			0.1
		6			1.1			6			1.3
40	272.3	0	14.6	0.4	0.3	160	1478.6	0	348.4	0.1	6.7
		1	24.3	3.5	0.5			1	12.1	0.8	1.1
		2	41.3	6.8	1.8			2	86.2	3.3	0.3
		3		0.3	1.3			3		2.3	1.3
		4		4.9	1.2			4		2.7	0.5
		5			0.3			5			0.1
		6			1.2			6			0.1
41	276.4	0	1.3	0.0	0.6	161	1481.1	0	157.9	1.0	1.5
		1	79.5	2.8	10.0			1	13.9	1.4	1.5
		2	3.5	2.4	5.5			2	754.8	0.7	2.2

		3		0.3	0.5			3		0.1	0.0
		4		0.3	0.1			4		2.0	0.0
		5			0.0			5			0.1
		6			0.0			6			0.7
42	279.0	0	11.0	2.7	16.9	162	1483.3	0	2.0	0.1	0.0
		1	105.8	0.7	5.3			1	80.5	1.2	0.5
		2	45.5	11.4	0.1			2	133.5	0.9	0.0
		3		0.8	1.0			3		0.0	0.1
		4		1.2	0.2			4		4.8	0.3
		5			0.2			5			0.0
		6			0.4			6			0.3
43	280.1	0	18.6	0.4	7.6	163	1484.5	0	12.9	0.2	5.0
		1	25.2	13.6	0.5			1	11.8	1.9	0.7
		2	156.0	42.5	4.0			2	148.1	2.5	0.0
		3		1.2	6.7			3		2.0	1.3
		4		1.9	0.6			4		0.4	0.1
		5			1.1			5			0.0
		6			1.9			6			0.0
44	288.7	0	30.1	2.5	3.4	164	1485.1	0	49.8	1.1	0.5
		1	10.3	1.1	0.2			1	58.8	4.2	1.5
		2	144.1	3.5	0.3			2	1278.9	0.6	0.2
		3		0.2	1.4			3		5.7	3.6
		4		0.5	0.2			4		1.7	0.2
		5			0.7			5			0.1
		6			6.6			6			0.4
45	292.0	0	6.2	0.2	5.8	165	1485.9	0	10.9	0.6	4.6
		1	60.5	0.1	1.0			1	24.3	0.4	0.4
		2	213.1	0.3	0.9			2	15.3	0.5	0.0
		3		2.9	2.4			3		1.3	0.5
		4		0.2	0.1			4		0.4	0.0
		5			0.1			5			0.0
		6			0.1			6			0.0
46	294.5	0	48.3	3.4	15.1	166	1486.7	0	126.1	0.1	0.3
		1	3.7	1.9	0.5			1	133.3	3.8	4.2
		2	213.3	4.8	2.2			2	112.2	4.0	2.3
		3		1.3	1.2			3		0.1	0.2
		4		0.1	0.3			4		6.7	0.5
		5			0.0			5			0.0
		6			0.8			6			0.5
47	302.1	0	120.4	0.0	0.4	167	1488.6	0	338.5	1.2	0.6
		1	13.4	1.7	0.1			1	15.5	1.0	0.6

		2	164.6	3.5	0.3			2	124.0	1.1	0.3
		3		2.9	1.9			3		0.2	0.2
		4		2.3	0.0			4		0.6	0.0
		5			0.1			5			0.0
		6			0.2			6			0.2
48	308.6	0	0.2	2.9	2.6	168	1489.7	0	326.4	2.3	1.1
		1	36.2	0.8	0.0			1	83.4	0.6	1.9
		2	15.9	1.9	0.1			2	429.9	1.0	3.0
		3		0.4	0.1			3		0.6	0.6
		4		4.2	0.1			4		7.6	0.4
		5			0.1			5			0.2
		6			1.6			6			1.7
49	317.2	0	17.7	0.4	7.4	169	1490.9	0	142.0	1.4	4.9
		1	1.0	0.1	0.4			1	11.9	1.0	0.1
		2	23.1	2.9	1.5			2	93.1	1.1	0.2
		3		1.8	0.8			3		1.2	0.6
		4		8.9	2.3			4		2.9	0.2
		5			0.7			5			0.1
		6			1.2			6			0.1
50	338.1	0	3994.8	89.6	146.1	170	1491.9	0	364.8	2.9	8.2
		1	55.6	102.6	182.0			1	99.1	0.9	1.3
		2	71.6	22.4	13.2			2	1044.9	1.7	1.9
		3		2.7	3.5			3		1.8	0.6
		4		1.3	70.6			4		1.7	0.0
		5			165.9			5			0.1
		6			42.0			6			1.4
51	350.8	0	96.1	1.5	13.8	171	1492.7	0	1.1	0.5	0.0
		1	98.9	13.5	4.4			1	248.8	6.2	3.5
		2	995.2	4.1	3.0			2	405.1	2.7	0.3
		3		9.7	5.2			3		1.6	1.1
		4		11.5	4.1			4		2.0	0.1
		5			3.0			5			0.0
		6			18.6			6			0.1
52	356.6	0	44.5	1.7	4.9	172	1495.3	0	106.8	10.1	0.0
		1	15.1	0.9	2.2			1	58.2	3.4	2.1
		2	306.2	1.7	6.2			2	249.8	0.7	0.7
		3		5.5	3.1			3		2.1	1.1
		4		22.8	1.4			4		0.5	0.1
		5			5.0			5			0.1
		6			14.0			6			0.2
53	373.7	0	12.2	1.7	5.4	173	1497.1	0	5.7	8.1	0.2

		1	24.2	3.9	1.9			1	17.3	1.8	1.5
		2	56.5	0.9	2.3			2	266.0	0.2	0.3
		3		1.4	0.4			3		0.6	0.5
		4		2.1	1.6			4		4.6	0.0
		5			0.1			5			0.0
		6			3.2			6			0.5
54	394.7	0	1.1	13.0	14.6	174	1502.3	0	56.0	0.3	5.6
		1	20100.1	37.6	10.1			1	28.8	0.7	0.5
		2	2238.1	3.4	40.8			2	24.7	3.1	0.2
		3		14.6	14.0			3		0.8	0.5
		4		64.4	4.4			4		1.0	0.1
		5			0.3			5			0.0
		6			0.1			6			0.0
55	409.7	0	4942.4	16.6	63.8	175	1506.5	0	506.5	4.8	0.1
		1	21268.8	18.8	5.8			1	30.1	0.8	0.2
		2	4249.5	37.4	6.7			2	132.4	0.4	0.0
		3		26.3	27.3			3		2.4	0.5
		4		21.0	2.9			4		1.7	0.7
		5			2.1			5			0.0
		6			0.4			6			0.0
56	440.6	0	59.0	5.9	18.3	176	1507.9	0	105.3	0.1	2.5
		1	32.9	1.1	2.0			1	27.5	2.7	0.8
		2	88.4	0.6	0.3			2	318.1	3.7	0.4
		3		1.0	0.6			3		1.9	0.9
		4		0.4	0.7			4		1.7	0.2
		5			0.1			5			0.0
		6			0.4			6			0.2
57	458.4	0	74.3	5.4	5.9	177	1509.4	0	0.6	3.0	5.4
		1	44.4	0.7	2.9			1	5.9	0.2	0.1
		2	85.3	0.3	0.5			2	1.2	6.7	1.0
		3		0.8	0.7			3		1.3	0.6
		4		1.0	1.2			4		1.0	1.3
		5			0.0			5			0.1
		6			0.1			6			0.3
58	465.9	0	75.2	0.1	2.9	178	1512.5	0	5.2	0.4	2.0
		1	130.7	2.4	0.1			1	124.7	2.2	2.5
		2	230.2	0.5	0.2			2	2108.9	3.3	3.4
		3		0.2	1.2			3		9.7	4.9
		4		1.3	1.0			4		6.2	1.1
		5			0.1			5			0.1
		6			0.4			6			0.2

59	489.6	0	505.0	4.6	1.3	179	1512.7	0	459.7	1.3	0.2
		1	216.4	2.1	11.9			1	10.4	0.2	0.0
		2	501.1	5.5	3.5			2	183.5	1.8	1.2
		3		0.6	0.8			3		3.8	2.9
		4		0.4	2.5			4		2.2	0.3
		5			0.2			5			0.1
		6			0.4			6			0.2
60	510.7	0	1785.8	6.2	19.9	180	1514.1	0	113.3	0.1	2.0
		1	357.7	15.0	59.8			1	22.8	0.6	0.5
		2	231.4	1.1	1.6			2	1755.1	12.3	9.4
		3		3.9	4.0			3		12.9	8.4
		4		0.8	2.7			4		0.6	3.3
		5			5.1			5			0.3
		6			2.2			6			0.0
61	526.6	0	1572.7	7.4	17.6	181	1514.3	0	0.6	22.0	0.6
		1	839.9	6.4	28.6			1	163.4	0.5	0.0
		2	309.8	4.0	12.5			2	1790.3	20.9	9.4
		3		8.5	3.1			3		23.1	18.4
		4		4.5	1.4			4		2.5	3.5
		5			1.6			5			0.0
		6			1.1			6			0.1
62	554.9	0	16.2	0.4	0.0	182	1516.1	0	7.2	2.4	0.0
		1	78.1	0.4	7.0			1	78.6	0.5	1.0
		2	8212.0	52.7	30.4			2	683.5	0.5	1.0
		3		16.4	2.5			3		0.2	0.2
		4		0.2	0.0			4		0.3	0.0
		5			0.0			5			0.0
		6			0.0			6			1.3
63	555.8	0	84.2	44.6	2.9	183	1520.4	0	6.7	1.5	3.4
		1	262.7	1.3	2.9			1	38.9	1.0	0.6
		2	5208.5	7.4	1.6			2	933.0	0.1	0.3
		3		7.8	14.5			3		3.2	1.2
		4		0.2	4.6			4		2.2	0.2
		5			0.4			5			0.0
		6			0.0			6			0.2
64	556.5	0	11.9	0.0	3.0	184	1520.7	0	4.0	0.1	0.2
		1	28.3	0.3	0.2			1	22.2	1.1	0.9
		2	35.5	0.9	0.7			2	118.7	0.1	0.6
		3		0.3	0.1			3		3.5	1.9
		4		0.3	0.4			4		1.5	0.0
		5			0.4			5			0.1

		6			0.1			6			0.3
65	559.4	0	39.0	38.0	5.8	185	1522.9	0	4892.0	6.8	3.9
		1	786.7	1.3	15.1			1	598.9	43.8	3.1
		2	488.2	4.5	3.1			2	7620.4	2.2	13.0
		3		4.1	3.8			3		34.7	1.2
		4		17.2	5.1			4		40.2	4.1
		5			0.3			5			0.3
		6			0.3			6			7.2
66	574.9	0	19.3	0.7	0.1	186	1535.0	0	3.6	0.0	0.2
		1	1212.1	13.8	0.1			1	387.5	155.4	25.9
		2	370.6	0.8	10.4			2	103.5	25.0	4.8
		3		16.6	6.5			3		0.2	11.0
		4		14.1	1.7			4		0.3	6.1
		5			0.3			5			2.0
		6			0.8			6			0.1
67	577.5	0	2.1	2.7	15.4	187	1540.2	0	495.5	45.2	6.7
		1	14825.0	79.7	0.0			1	46.1	62.3	9.1
		2	2826.1	50.7	52.9			2	716.7	21.5	7.9
		3		4.0	19.4			3		4.9	3.5
		4		33.5	1.9			4		0.4	10.2
		5			0.0			5			1.8
		6			0.9			6			0.2
68	590.6	0	53.4	1.0	244.7	188	2949.1	0	107.5	6.1	0.0
		1	8648.9	160.7	44.8			1	50.8	2.6	0.0
		2	4028.4	159.2	15.0			2	259.7	0.4	0.5
		3		123.7	73.0			3		4.3	0.8
		4		50.3	11.2			4		2.5	0.3
		5			0.8			5			0.1
		6			0.3			6			3.2
69	605.1	0	3682.0	17.4	0.3	189	2969.1	0	463.9	2.2	0.7
		1	516.8	9.9	0.1			1	35.9	0.5	0.6
		2	417.2	4.7	3.7			2	1177.2	0.3	1.5
		3		7.1	3.8			3		0.0	0.1
		4		4.1	4.1			4		2.5	0.2
		5			0.4			5			0.2
		6			0.9			6			1.7
70	632.9	0	80.3	14.4	6.8	190	3001.1	0	1282.5	0.8	0.1
		1	4136.8	24.7	15.1			1	34.2	0.5	0.3
		2	1779.2	277.8	10.9			2	45.3	3.3	0.2
		3		333.5	58.2			3		0.2	0.1
		4		363.6	161.6			4		0.7	0.1

		5			63.3			5			0.0
		6			16.4			6			0.0
71	640.5	0	655.8	388.3	12.4	191	3042.7	0	19.6	0.0	6.8
		1	1466.0	283.5	50.5			1	8.6	0.5	0.3
		2	7103.1	1422.6	403.2			2	101.9	2.1	0.3
		3		207.1	260.5			3		1.4	0.2
		4		120.1	50.2			4		1.6	0.2
		5			8.7			5			0.2
		6			0.1			6			0.3
72	713.0	0	0.3	2.8	0.8	192	3045.7	0	2.0	0.0	1.4
		1	35.1	0.1	21.4			1	45.2	0.2	0.1
		2	638.6	17.1	5.9			2	77.8	3.5	0.8
		3		1.5	3.4			3		0.1	0.1
		4		2.1	1.2			4		3.4	0.0
		5			0.2			5			0.0
		6			0.0			6			0.6
73	730.6	0	757.1	32.8	0.2	193	3046.5	0	53.7	0.0	1.8
		1	1486.5	59.6	20.8			1	25.8	0.3	0.1
		2	5071.8	64.3	1.3			2	13.1	2.0	0.4
		3		181.2	78.0			3		0.0	0.0
		4		24.2	39.9			4		1.6	0.0
		5			2.5			5			0.0
		6			0.1			6			0.1
74	732.5	0	511.1	40.5	13.9	194	3047.8	0	0.0	0.0	0.9
		1	384.0	9.0	2.0			1	9.7	0.0	0.0
		2	2308.7	69.3	3.0			2	63.9	0.6	0.1
		3		180.8	95.8			3		0.0	0.0
		4		39.5	54.0			4		0.2	0.0
		5			11.0			5			0.0
		6			0.7			6			0.0
75	754.8	0	127.8	645.8	218.7	195	3049.2	0	34.1	0.0	2.5
		1	13776.4	3316.7	759.2			1	23.1	0.1	0.1
		2	1669.6	1024.4	1817.2			2	16.3	0.3	0.1
		3		675.0	1579.2			3		0.1	0.1
		4		997.5	864.1			4		0.3	0.0
		5			120.2			5			0.0
		6			7.7			6			0.0
76	791.4	0	3.4	3.8	35.9	196	3051.3	0	13.5	0.0	0.0
		1	111.6	2.9	4.2			1	6.2	0.1	0.2
		2	397.5	4.7	6.5			2	74.7	2.3	0.3
		3		2.2	2.1			3		0.0	0.1

		4		3.7	0.2			4		0.1	0.0
		5			0.1			5			0.0
		6			0.0			6			0.0
77	818.0	0	524.7	24.8	6.4	197	3052.3	0	1.1	0.0	0.3
		1	518.9	3.4	1.0			1	14.2	0.0	0.1
		2	128.1	0.9	3.7			2	3.0	0.3	0.0
		3		4.9	1.2			3		0.0	0.0
		4		20.5	0.1			4		0.2	0.0
		5			0.1			5			0.0
		6			0.0			6			0.0
78	822.1	0	23.2	0.3	0.0	198	3055.5	0	9.8	1.0	1.7
		1	934.0	6.1	1.4			1	3.9	1.3	0.0
		2	19.1	2.1	2.5			2	4.8	0.3	0.2
		3		0.6	0.2			3		0.1	0.0
		4		24.3	1.0			4		0.1	0.1
		5			0.4			5			0.0
		6			0.1			6			0.0
79	878.3	0	23.0	0.3	0.1	199	3060.8	0	11.2	0.3	0.2
		1	7.5	3.0	0.2			1	2.5	0.0	0.1
		2	1850.8	7.7	1.1			2	16.8	0.1	0.2
		3		0.5	0.1			3		0.1	0.1
		4		0.8	0.2			4		0.0	0.0
		5			0.8			5			0.0
		6			0.7			6			0.0
80	892.2	0	10.2	1.0	0.2	200	3062.0	0	4.2	0.1	0.4
		1	25.2	2.7	0.6			1	0.6	0.1	0.0
		2	965.6	0.9	0.6			2	27.1	0.1	0.4
		3		5.2	0.8			3		0.2	0.1
		4		1.1	0.0			4		0.0	0.0
		5			0.1			5			0.0
		6			0.0			6			0.0
81	902.4	0	35.9	2.6	1.0	201	3067.1	0	0.9	0.0	0.2
		1	14.1	0.1	0.2			1	0.5	0.0	0.0
		2	225.6	0.3	0.1			2	18.7	0.0	0.0
		3		0.0	0.0			3		0.0	0.1
		4		1.5	0.1			4		0.0	0.0
		5			0.0			5			0.0
		6			0.1			6			0.0
82	911.1	0	6.1	0.0	0.0	202	3068.0	0	1.9	0.0	0.0
		1	67.3	0.2	0.0			1	0.4	0.1	0.0
		2	482.3	3.4	0.2			2	8.2	0.0	0.1

		3		1.1	0.0			3		0.0	0.0
		4		0.7	0.0			4		0.1	0.0
		5			0.3			5			0.0
		6			0.2			6			0.0
83	919.2	0	1.2	0.0	0.1	203	3069.0	0	1.9	0.0	0.0
		1	8.8	0.1	0.2			1	1.9	0.0	0.1
		2	4.3	0.2	0.0			2	12.2	0.0	0.0
		3		0.0	0.1			3		0.1	0.1
		4		0.2	0.0			4		0.0	0.0
		5			0.1			5			0.0
		6			0.0			6			0.0
84	925.6	0	19.4	0.0	0.0	204	3073.9	0	4.9	0.0	0.0
		1	19.6	0.7	0.1			1	9.6	0.3	0.1
		2	95.5	1.1	0.2			2	19.8	0.0	0.2
		3		0.4	0.1			3		0.1	0.2
		4		0.1	0.0			4		0.0	0.0
		5			0.0			5			0.0
		6			0.0			6			0.0
85	928.7	0	1.7	2.6	2.0	205	3091.4	0	0.3	0.0	0.0
		1	36.3	0.6	0.1			1	3.4	0.0	0.0
		2	29.2	0.5	0.2			2	221.9	0.7	0.0
		3		0.0	0.1			3		0.1	0.1
		4		3.8	0.1			4		0.1	0.0
		5			0.1			5			0.0
		6			0.1			6			0.5
86	931.0	0	2.0	0.0	0.1	206	3095.4	0	5.5	0.0	0.0
		1	23.6	0.3	0.0			1	10.7	1.8	0.0
		2	40.0	0.1	0.2			2	158.2	0.9	0.4
		3		0.1	0.1			3		0.1	0.1
		4		1.0	0.1			4		2.2	0.2
		5			0.0			5			0.0
		6			0.0			6			0.3
87	931.7	0	4.1	0.7	0.5	207	3099.9	0	9.6	0.1	0.2
		1	32.0	0.1	0.3			1	2.9	0.1	0.0
		2	223.8	0.2	0.1			2	7.8	0.0	0.1
		3		1.6	0.5			3		0.1	0.0
		4		0.4	0.5			4		0.0	0.0
		5			0.0			5			0.0
		6			0.0			6			0.0
88	937.6	0	33.4	0.5	0.1	208	3103.3	0	28.8	0.0	0.0
		1	9.3	0.3	0.3			1	0.5	0.1	0.0

		2	12.9	0.1	0.1			2	31.5	0.3	0.0
		3		0.4	0.2			3		0.0	0.0
		4		0.4	0.1			4		0.3	0.0
		5			0.0			5			0.0
		6			0.0			6			0.0
89	958.9	0	347.5	6.3	0.2	209	3105.5	0	151.6	0.1	1.0
		1	239.8	0.2	1.5			1	37.3	2.5	0.0
		2	1723.4	3.9	0.1			2	24.0	0.9	1.6
		3		0.3	0.4			3		0.2	0.0
		4		1.0	0.1			4		0.5	0.0
		5			0.9			5			0.0
		6			1.9			6			0.0
90	961.4	0	0.3	48.8	0.5	210	3106.4	0	11.5	1.0	2.3
		1	190.1	5.2	1.8			1	38.3	1.8	0.0
		2	3337.8	76.8	22.8			2	52.9	1.8	0.9
		3		42.6	22.5			3		0.4	0.0
		4		0.2	3.0			4		0.2	0.0
		5			0.1			5			0.0
		6			0.0			6			0.0
91	963.9	0	5.0	0.1	0.1	211	3106.9	0	70.4	2.6	0.0
		1	12.5	1.1	0.2			1	3.3	0.7	0.1
		2	82.4	5.0	1.0			2	1.3	0.1	0.1
		3		0.5	0.0			3		0.7	0.2
		4		0.9	0.0			4		1.0	0.6
		5			0.1			5			0.1
		6			0.6			6			0.2
92	967.2	0	18.6	0.3	1.1	212	3107.8	0	29.9	1.1	2.5
		1	61.5	0.0	0.0			1	6.7	0.2	0.0
		2	2243.5	1.2	3.6			2	11.8	0.2	0.1
		3		40.7	16.4			3		0.1	0.0
		4		1.9	4.6			4		0.0	0.0
		5			0.3			5			0.0
		6			0.0			6			0.0
93	970.8	0	21.7	0.1	0.7	213	3108.0	0	93.9	0.0	2.2
		1	42.0	0.1	0.1			1	6.3	0.4	0.4
		2	14.3	0.2	0.0			2	10.0	0.0	0.8
		3		0.1	0.2			3		0.1	0.2
		4		0.7	0.0			4		0.3	0.1
		5			0.0			5			0.0
		6			0.0			6			0.0
94	973.8	0	21.2	0.4	0.0	214	3109.0	0	18.1	0.1	4.9

		1	3.1	0.1	0.0			1	3.3	0.7	0.0
		2	79.3	0.1	0.1			2	6.0	0.0	0.7
		3		2.0	1.6			3		0.1	0.1
		4		0.1	0.3			4		0.1	0.1
		5			0.0			5			0.0
		6			0.0			6			0.0
95	976.3	0	70.0	0.3	0.0	215	3118.2	0	1.6	0.9	2.4
		1	47.1	0.2	0.2			1	1.0	0.0	0.1
		2	16.9	0.7	0.2			2	15.8	0.2	0.2
		3		0.9	0.7			3		0.1	0.0
		4		0.7	0.1			4		0.0	0.0
		5			0.0			5			0.0
		6			0.0			6			0.0
96	1033.3	0	20.9	0.0	0.1	216	3119.6	0	50.2	0.9	0.1
		1	2252.6	19.6	23.4			1	41.0	0.3	0.2
		2	500.7	1.3	9.8			2	40.8	1.4	0.1
		3		1.5	1.1			3		0.2	0.2
		4		22.0	1.0			4		1.3	0.1
		5			0.3			5			0.0
		6			0.0			6			0.3
97	1037.3	0	20.7	8.1	12.7	217	3127.4	0	1.4	0.0	0.0
		1	1426.8	5.8	4.5			1	13.4	0.1	0.0
		2	5691.1	61.9	16.0			2	0.5	0.1	0.0
		3		24.3	10.7			3		0.1	0.0
		4		9.4	2.7			4		0.1	0.0
		5			0.1			5			0.0
		6			0.2			6			0.0
98	1037.7	0	1132.4	10.7	32.8	218	3127.6	0	39.6	0.0	0.2
		1	810.1	11.9	1.4			1	4.3	0.2	0.0
		2	1441.6	9.1	10.5			2	22.1	0.1	0.1
		3		5.7	6.1			3		0.0	0.0
		4		16.5	0.3			4		0.1	0.0
		5			0.1			5			0.0
		6			0.0			6			0.0
99	1043.8	0	516.3	20.4	4.5	219	3131.2	0	22.3	0.4	0.1
		1	26.1	8.5	0.8			1	15.8	0.2	0.0
		2	333.9	74.1	27.7			2	3.7	0.4	0.1
		3		4.0	3.8			3		0.0	0.0
		4		0.5	4.1			4		0.0	0.0
		5			1.2			5			0.0
		6			0.1			6			0.0

100	1045.0	0	152.9	11.7	1.2	220	3131.6	0	11.8	0.3	0.4
		1	213.9	3.4	0.8			1	1.5	0.1	0.0
		2	9431.5	59.1	10.2			2	44.9	0.3	0.1
		3		122.5	58.0			3		0.0	0.1
		4		1.2	0.9			4		0.1	0.0
		5			0.7			5			0.0
		6			0.3			6			0.0
101	1045.3	0	286.2	0.6	1.2	221	3133.9	0	24.6	0.0	0.2
		1	48.1	3.2	1.5			1	6.1	0.0	0.1
		2	271.1	14.2	3.3			2	8.9	0.3	0.1
		3		69.2	40.4			3		0.1	0.1
		4		1.8	6.3			4		0.0	0.0
		5			1.1			5			0.0
		6			0.2			6			0.0
102	1048.4	0	454.3	0.0	3.8	222	3135.8	0	8.1	0.1	0.2
		1	18.8	1.6	4.4			1	1.2	0.0	0.0
		2	375.2	37.4	4.1			2	2.0	0.2	0.0
		3		25.0	15.6			3		0.0	0.0
		4		1.8	3.7			4		0.0	0.0
		5			0.1			5			0.0
		6			0.1			6			0.0
103	1074.8	0	6.1	0.0	0.0	223	3137.3	0	69.7	0.1	0.0
		1	46.8	3.6	0.2			1	2.6	0.0	0.1
		2	633.4	15.4	3.1			2	3.9	0.1	0.0
		3		2.7	1.7			3		0.1	0.1
		4		0.8	0.8			4		0.0	0.0
		5			0.1			5			0.0
		6			0.2			6			0.0
104	1085.3	0	10.5	2.8	1.3	224	3138.5	0	125.4	0.1	0.2
		1	14.6	1.1	0.3			1	26.1	3.5	0.3
		2	132.1	3.8	2.8			2	87.4	0.5	0.4
		3		0.9	0.7			3		0.1	0.1
		4		0.2	0.1			4		0.1	0.0
		5			0.0			5			0.0
		6			0.0			6			0.0
105	1085.8	0	7.5	0.0	1.2	225	3141.2	0	0.0	0.0	3.5
		1	303.6	0.7	15.5			1	3.9	0.1	0.1
		2	33.5	0.9	4.7			2	53.3	0.2	0.2
		3		1.8	1.8			3		0.3	0.0
		4		5.6	1.4			4		0.2	0.0
		5			0.2			5			0.0

		6			0.1			6			0.0
106	1086.7	0	8.5	0.7	37.9	226	3141.3	0	42.5	0.9	2.4
		1	173.4	0.2	9.3			1	0.5	0.0	0.1
		2	37.4	1.2	6.1			2	31.9	0.3	0.2
		3		0.0	0.4			3		0.0	0.0
		4		3.5	1.0			4		0.1	0.0
		5			0.3			5			0.0
		6			0.0			6			0.0
107	1120.6	0	2.8	0.0	0.0	227	3141.6	0	0.0	0.2	0.1
		1	2.6	0.2	0.0			1	0.3	0.0	0.0
		2	18.1	0.4	0.5			2	0.9	0.0	0.0
		3		0.2	0.0			3		0.0	0.0
		4		0.1	0.2			4		0.0	0.0
		5			0.1			5			0.0
		6			0.0			6			0.0
108	1122.6	0	161.0	0.3	9.8	228	3151.5	0	14.4	0.1	3.7
		1	12.3	4.1	1.8			1	3.2	0.1	0.1
		2	1028.0	0.7	0.3			2	1.1	0.1	0.0
		3		6.7	5.2			3		0.1	0.0
		4		0.2	1.1			4		0.1	0.0
		5			0.1			5			0.0
		6			0.1			6			0.0
109	1136.4	0	2021.8	25.1	2.4	229	3151.9	0	1.3	0.0	0.3
		1	1269.6	9.5	0.8			1	0.1	0.0	0.0
		2	4745.4	6.3	0.5			2	11.7	0.0	0.0
		3		5.7	0.5			3		0.0	0.0
		4		2.6	0.1			4		0.1	0.0
		5			0.8			5			0.0
		6			0.5			6			0.0
110	1142.6	0	186.6	3.8	18.9	230	3153.9	0	13.7	0.9	1.4
		1	96.7	7.8	4.8			1	3.4	0.2	0.0
		2	2747.1	0.6	0.4			2	42.5	0.3	0.0
		3		13.8	2.4			3		0.0	0.1
		4		0.1	0.3			4		0.1	0.1
		5			0.1			5			0.0
		6			0.0			6			0.2
111	1146.9	0	1765.4	1.3	1.7	231	3155.2	0	25.7	0.0	0.1
		1	1123.6	5.7	0.7			1	0.3	0.0	0.0
		2	3012.1	2.4	2.0			2	34.3	0.6	0.0
		3		20.0	2.6			3		0.0	0.0
		4		0.3	0.6			4		0.3	0.0

		5			0.1			5			0.0
		6			0.2			6			0.0
112	1150.3	0	27.7	1.1	0.0	232	3155.5	0	10.3	0.0	0.1
		1	129.3	0.8	1.8			1	0.2	0.0	0.0
		2	191.7	1.2	0.7			2	9.1	0.2	0.0
		3		3.1	1.3			3		0.0	0.0
		4		0.8	0.1			4		0.1	0.0
		5			0.0			5			0.0
		6			0.0			6			0.1
113	1153.7	0	1016.1	1.0	1.4	233	3160.0	0	27.9	1.0	1.4
		1	239.9	2.1	2.6			1	4.0	0.1	0.0
		2	323.2	0.4	2.1			2	0.4	0.0	0.0
		3		1.7	0.3			3		0.1	0.1
		4		0.2	0.1			4		0.1	0.0
		5			0.0			5			0.0
		6			0.0			6			0.0
114	1156.6	0	751.8	2.1	8.4	234	3162.0	0	2.8	0.0	0.0
		1	64.6	0.1	2.8			1	0.3	0.0	0.0
		2	112.6	1.1	0.1			2	5.4	0.1	0.0
		3		1.8	1.6			3		0.0	0.0
		4		0.0	0.3			4		0.2	0.0
		5			0.0			5			0.0
		6			0.0			6			0.0
115	1167.6	0	90.9	0.8	3.2	235	3173.4	0	4.0	0.0	0.1
		1	36.9	0.6	0.1			1	0.1	0.0	0.0
		2	3116.9	5.8	1.0			2	21.5	0.1	0.0
		3		0.5	0.3			3		0.1	0.0
		4		0.3	0.3			4		0.1	0.0
		5			0.0			5			0.0
		6			0.0			6			0.0
116	1182.9	0	480.0	2.6	2.0	236	3182.6	0	1.5	0.0	0.1
		1	34.0	4.5	2.0			1	1.4	0.0	0.0
		2	535.7	0.1	0.6			2	8.2	0.1	0.0
		3		3.4	3.0			3		0.0	0.0
		4		0.5	1.5			4		0.1	0.0
		5			0.0			5			0.0
		6			0.1			6			0.0
117	1193.6	0	1196.2	104.0	8.0	237	3188.1	0	3.8	0.0	0.1
		1	7428.8	91.5	38.7			1	0.9	0.0	0.0
		2	3196.4	48.6	65.8			2	2.6	0.0	0.0
		3		42.6	6.1			3		0.0	0.0

		4		1.1	1.2
		5			0.0
		6			0.1
118	1193.7	0	44.4	0.5	0.4
		1	256.0	55.4	11.7
		2	10944.8	72.3	16.9
		3		136.4	65.3
		4		2.9	15.3
		5			1.9
		6			0.1
119	1196.9	0	292.9	3.4	0.1
		1	102.0	0.5	0.9
		2	62.1	4.8	1.9
		3		1.6	0.5
		4		7.2	0.6
		5			0.0
		6			0.2
120	1202.9	0	186.9	5.4	2.9
		1	224.8	6.0	0.3
		2	323.1	7.4	1.1
		3		1.3	0.7
		4		4.0	0.3
		5			0.2
		6			0.2

4	0.0	0.0
5		0.0
6		0.0

Table S18. The normal modes of Dy-5* within the relevant energy scale of $\Delta M = \pm 1$ and $\Delta M = \pm 2$ transitions causing the largest spin-phonon couplings $\left|\partial B_{2\pm1}/Q_n\right|^2$ and $\left|\partial B_{2\pm2}/Q_n\right|^2$ in ascending order

n	ω / cm^{-1}	$\left\|\partial B_{2\pm1}/Q_n\right\|^2$
55	409.75	21268.8
54	394.74	20100.1
67	577.48	14825.0
68	590.65	8648.9
70	632.94	4136.8
71	640.55	1466.0
66	574.93	1212.1
61	526.61	839.9
65	559.38	786.7
29	200.27	591.1
69	605.06	516.8
60	510.66	357.7
31	213.74	271.0
63	555.84	262.7
59	489.59	216.4
30	212.56	191.8
36	248.66	162.2
58	465.93	130.7
42	278.97	105.8
51	350.78	98.9
41	276.36	79.5
62	554.86	78.1
32	218.77	64.0
45	291.97	60.5
50	338.11	55.6
57	458.4	44.4
39	270.87	42.8
38	265.43	40.0
48	308.58	36.2
35	244.21	33.1
56	440.58	32.9
64	556.51	28.3
43	280.09	25.2
40	272.34	24.3
53	373.67	24.2
33	236.13	21.2
34	241.95	15.8

n	ω / cm^{-1}	$\left\|\partial B_{2\pm2}/Q_n\right\|^2$
100	1045.03	9431.5
62	554.86	8212.0
71	640.55	7103.1
97	1037.26	5691.1
63	555.84	5208.5
73	730.58	5071.8
55	409.75	4249.5
68	590.65	4028.4
90	961.42	3337.8
67	577.48	2826.1
74	732.48	2308.7
92	967.23	2243.5
54	394.74	2238.1
79	878.29	1850.8
70	632.94	1779.2
89	958.89	1723.4
75	754.78	1669.6
98	1037.68	1441.6
80	892.22	965.6
72	712.98	638.6
103	1074.84	633.4
59	489.59	501.1
96	1033.33	500.7
65	559.38	488.2
82	911.12	482.3
69	605.06	417.2
76	791.37	397.5
102	1048.36	375.2
66	574.93	370.6
99	1043.76	333.9
61	526.61	309.8
101	1045.33	271.1
60	510.66	231.4
58	465.93	230.2
81	902.44	225.6
87	931.69	223.8
104	1085.32	132.1

52	356.62	15.1
47	302.13	13.4
44	288.7	10.3
37	253.99	4.8
46	294.5	3.7
49	317.2	1.0

77	818.01	128.1
84	925.63	95.5
56	440.58	88.4
57	458.4	85.3
91	963.9	82.4
94	973.81	79.3
86	930.97	40.0
106	1086.74	37.4
64	556.51	35.5
105	1085.82	33.5
85	928.75	29.2
78	822.12	19.1
95	976.3	16.9
93	970.78	14.3
88	937.64	12.9
83	919.22	4.3

Captions for Movies S1 to S7:

Movie S1. Normal vibrational mode 54.
Movie S2. Normal vibrational mode 55.
Movie S3. Normal vibrational mode 66.
Movie S4. Normal vibrational mode 67.
Movie S5. Normal vibrational mode 68.
Movie S6. Normal vibrational mode 70.
Movie S7. Normal vibrational mode 71.

Captions for Data S1:

Caption 1: Cartesian coordinates for the optimized geometry of Dy-5*.
Caption 2: Cartesian coordinates for the displacement geometries used in the evaluation of the spin-phonon couplings in Dy-5*.
Caption 3: Original data for the magnetic property measurements.

References

36. H. Sitzmann, *Z. Naturforsch* **44b**, 1293 (1989).
37. S. M. Cendrowski-Guillaume, G. Le Grand, M. Nierlich, M. Ephritikhine, *Organometallics* **19**, 5654 (2000).
38. W. J. Evans, S. A. Kozimor, J. W. Ziller, N. Kaltsoyannis, *J. Am. Chem. Soc.* **126**, 14533 (2004).
39. O. V. Dolomanov, L. J. Bourhis, R. J. Gildea, J. A. K. Howard, H. Puschmann, *J. Appl. Cryst.* **42**, 339 (2009).
40. G. M. Sheldrick, *Acta Cryst.* **A71**, 3 (2015).
41. G. M. Sheldrick, *Acta Cryst.* **C71**, 3 (2015).
42. G. A. Bain, J. F. Berry, *J. Chem. Educ.* **85**, 532 (2008).
43. D. Gatteschi, R. Sessoli, J. Villain, Molecular Nanomagnets. Oxford University Press (2006).
44. D. Gatteschi, R. Sessoli, *Angew. Chem. Int. Ed.* **42**, 268-297 (2003).
45. F. Aquilante, J. Autschbach, R. K. Carlson, L. F. Chibotaru, M. G. Delcey, L. De Vico, I. Fdez. Galván, N. Ferré, L. M. Frutos, L. Gagliardi, M. Garavelli, A. Giussani, C. E. Hoyer, G. Li Manni, H. Lischka, D. Ma, P. Å. Malmqvist, T. Müller, A. Nenov, M. Olivucci, T. B. Pedersen, D. Peng, F. Plasser, B. Pritchard, M. Reiher, I. Rivalta, I. Schapiro, J. Segarra-Martí, M. Stenrup, D. G. Truhlar, L. Ungur, A. Valentini, S. Vancoillie, V. Veryazov, V. P. Vysotskiy, O. Weingart, F. Zapata, R. Lindh,. *J. Comp. Chem.* 2016, 37, 506–541.
46. P.-O. Widmark, P.-Å. Widmark, B. O. Roos. *Theor. Chim. Acta*, **77**, 1432 (1990).
47. B. O. Roos, R. Lindh, P. Å. Malmqvist, V. Veryazov, P.-O. Widmark. *J. Phys. Chem. A*, **108**, 2851 (2004).
48. W. Kutzelnigg, W. Liu. *J. Chem. Phys.* **123**, 241102 (2005).
49. M. Filatov. *J. Chem. Phys*. **125**, 107101 (2006).
50. Daoling, M. Reiher. *Theor. Chem. Acc.* **131**, 1 (2012).
51. B. O. Roos in *Advances in Chemical Physics*, *Ab Initio Methods in Quantum Chemistry II*, Vol. 69 (Ed.: K. P. Lawley), Wiley, New York, **1987**, pp. 399–455.
52. P. Siegbahn, A. Heiberg, B. Roos, B. Levy. *Phys. Scripta* **21**, 323 (1980).
53. B. O. Roos, P. R. Taylor, P. E. M. Siegbahn. *Chem. Phys.* **48,** 157 (1980).
54. P. E. M. Siegbahn, J. Almlöf, A. Heiberg, B. Roos. *J. Chem. Phys.* **74**, 2384 (1981).
55. B. O. Roos, R. Lindh, P. Å. Malmqvist, V. Veryazov, P.-O. Widmark. *Multiconfigurational Quantum Chemistry.* Wiley, Hoboken, NJ, **2016**.
56. B. O. Roos, P. Linse, P. E. M. Siegbahn, M. R. A. Blomberg. *Chem. Phys.* **66**, 197 (1982).
57. K. Andersson, P. Å Malmqvist, B. O. Roos, A. J. Sadlej, K. Wolinski. *J. Phys. Chem.* **94**, 5483 (1990).
58. K. Andersson, P.-Å. Malmqvist, B. O. Roos. *J. Chem. Phys.* **96**, 1218 (1992).
59. P. Å. Malmqvist, B. O. Roos, B. Schimmelpfenning. *Chem. Phys. Lett.* **357**, 230 (2002).
60. L. F. Chibotaru, L. Ungur. *J. Chem. Phys.* **137**, 064112 (2012).
61. Gaussian 09, Revision D.01, M. J. Frisch, G. W. Trucks, H. B. Schlegel, G. E. Scuseria, M. A. Robb, J. R. Cheeseman, G. Scalmani, V. Barone, G. A. Petersson, H. Nakatsuji, X. Li, M. Caricato, A. Marenich, J. Bloino, B. G. Janesko, R. Gomperts, B. Mennucci, H. P. Hratchian,

J. V. Ortiz, A. F. Izmaylov, J. L. Sonnenberg, D. Williams-Young, F. Ding, F. Lipparini, F. Egidi, J. Goings, B. Peng, A. Petrone, T. Henderson, D. Ranasinghe, V. G. Zakrzewski, J. Gao, N. Rega, G. Zheng, W. Liang, M. Hada, M. Ehara, K. Toyota, R. Fukuda, J. Hasegawa, M. Ishida, T. Nakajima, Y. Honda, O. Kitao, H. Nakai, T. Vreven, K. Throssell, J. A. Montgomery, Jr., J. E. Peralta, F. Ogliaro, M. Bearpark, J. J. Heyd, E. Brothers, K. N. Kudin, V. N. Staroverov, T. Keith, R. Kobayashi, J. Normand, K. Raghavachari, A. Rendell, J. C. Burant, S. S. Iyengar, J. Tomasi, M. Cossi, J. M. Millam, M. Klene, C. Adamo, R. Cammi, J. W. Ochterski, R. L. Martin, K. Morokuma, O. Farkas, J. B. Foresman, and D. J. Fox, Gaussian, Inc., Wallingford CT, **2009**.

62. J. P. Perdew, K. Burke, M. Ernzerhof. *Phys. Rev. Lett.* **77**, 3865 (1996).
63. J. P. Perdew, K. Burke, M. Ernzerhof. *Phys. Rev. Lett.* **78**, 1396 (1996).
64. M. Ernzerhof, G. E. Scuseria. *J. Chem. Phys.* **119**, 5029 (1999).
65. C. Adamo, V. Barone. *J. Chem. Phys.* **110**, 6158 (1999).
66. A Schäfer, C. Huber, R. Ahlrichs. *J. Chem. Phys.* **100**, 5829 (1994).
67. M. Dolg, H. Stoll, A. Savin, H. Preuss. *Theor. Chim. Acta* **75**, 173 (1989).
68. M. Dolg, H. Stoll, H. Preuss. *Theor. Chim. Acta* **85**, 441 (1993).
69. J. Yang, M. Dolg. *Theor. Chem. Acc.* **113**, 212 (2005).
70. A. Weigand, X. Cao, J. Yang, M. Dolg. *Theor. Chem. Acc.* **126**, 117 (2010).
71. S. Grimme, J. Antony, S. Ehrlich, H. Krieg. *J. Chem. Phys*. **132**, 154104 (2010).
72. S. Grimme, S. Ehrlich, L. Goerigk, *J. Comp. Chem*. **32**, 1456 (2011).
73. N. Iwahara, L. F. Chibotaru. *Phys. Rev. B* **91**, 174438 (2015).
74. N. Iwahara, L. Ungur, L. F. Chibotaru. *Phys. Rev. B* **91**, 054436 (2018).
75. K. N. Shrivastava. *Phys. Status Solidi B* **117**, 437 (1983).
76. D. H. Moseley, S. E. Stavretis, K. Thirunavukkuarasu, M. Ozerov, Y. Cheng, L. L. Daemen, J. Ludwig, Z. Lu, D. Smirnov, C. M. Brown, A. Pandey, A. J. Ramirez-Cuesta, A. C. Lamb, M. Atanasov, E. Bill, F. Neese, Z.-L. Xue. *Nat. Commun.* **9**, 2572 (2018).